

Saltwater Modelling of Fire Gas Flow through a Horizontal Ceiling Opening

A thesis submitted in partial fulfilment of the
requirements for the Degree of Master of Engineering in
Fire Engineering at the University of Canterbury by
M. A. Le Quesne

University of Canterbury
Christchurch, New Zealand

2010

Abstract

When fires occur in domestic or commercial buildings it is the smoke from the fire that leads to far more injury and death than the heat produced from the flames.

Understanding the movement of smoke within the fire compartment and through openings in the enclosure is critical for designing buildings to prevent fire fatalities.

Prediction of the movement of smoke is a complex phenomenon and is a continued focus of research throughout the world.

Work has been conducted in the past on the exchange flow rates through vertical openings, but very little has been done on horizontal ceiling openings. Current smoke transport calculations are most often carried out using standard vent flow models that do not accurately take in to account the buoyancy component of the flow. The fire zone model BRANZFire was developed with a ceiling vent flow algorithm based on the work of Cooper who found there was very little data on which to base his predictions. This report aims to provide additional experimental data on exchange flow rates through horizontal ceiling openings through the use of saltwater modelling and compare this to the work previously undertaken by Cooper.

Taking measurements of fire phenomena in hot and smoky environments can be difficult and expensive because the sooty environment and high temperatures involved can damage equipment and make taking accurate readings a challenge. Herein this problem is overcome through the use of a saltwater analogue system to model the conditions in a real fire scenario. The density difference created by a fire between the hot fire gases and the ambient air is replicated by using fresh and saltwater. The orientation of the experiment is inverted compared to the real life scenario as the saltwater which has the higher density is added to the fresh water. The saltwater is injected from a source on the 'floor' of the compartment into a tank of fresh water which generates a buoyant plume that 'rises' to the ceiling forming a distinct upper layer. Fluid in this layer exchanges with the ambient fluid through the ceiling opening.

The saltwater is dyed and Light Attenuation (LA) is used to discern the density of the fluid and hence the amount of mixing that has occurred. This can then be used to determine the amount of exchange flow through the ceiling vent.

An integral model for the descent of the interface between the hot smoky zone and the cool ambient zone has been developed and was found to perform well when compared with the saltwater experiments and another predictive model developed by Turner and Baines. The model was then developed further using mass conservation conventions to calculate the exchange flow through the ceiling opening.

The exchange rate through the ceiling opening was calculated and was found to compare well with Cooper's algorithm when an equivalent fire size of 323 kW was used but differed significantly when a fire twice this size was considered. It was found that Cooper's method did not adequately take into account the difference in fire sizes as the exchange flow predicted was almost identical between fire sizes for a particular ceiling vent. The implications of this are that the exchange, and hence the mixing and the amount of smoke, may be under predicted using larger fires in BRANZFire and this could lead to non-conservative design.

Acknowledgements

Firstly I would like to thank my supervisors, Mike Spearpoint and Associate Professor Mark Davidson for their support and guidance throughout the course of my thesis and for being able to point me in the right direction when needed. Mike's expertise in fire engineering and Mark's in fluid analysis offered two very different but essential view points to the study that really helped me put together a piece of work that incorporates both of these fields.

I would like to thank the New Zealand Fire Service Commission for their financial support of my study and their support of the fire engineering programme at the University.

Thank you to all the technical staff that helped me on this project, particularly Ian Sheppard and Kevin Wines who always found time to help me no matter what else they had going on (and it was usually a lot). Also, thanks to Grant and Bob who I could always rely on to build something or solve a problem at short notice.

I would like to thank Carl Voss, Simon Weaver and the rest of the Connell Wagner (Aurecon) team for their support during my studies.

Furthermore I would like to acknowledge the help of Dr Roger Nokes and Cameron Oliver who helped me with the more specialised Imagestream and Matlab programs employed in this research.

My final and most heartfelt thanks must go to my family and friends, particularly my parents, Geoff and Jan, for their continued support of my chosen path, even when that was sometimes a long and windy one.

Table of Contents

ABSTRACT	III
ACKNOWLEDGEMENTS	V
TABLE OF CONTENTS	VII
LIST OF FIGURES	X
LIST OF FIGURES	X
LIST OF TABLES.....	XIII
LIST OF NOTATIONS	XIV
1. INTRODUCTION	1
1.1. Research Impetus	2
1.2. Saltwater Modelling.....	2
1.3. Background.....	4
1.4. Research Objectives and Scope.....	6
1.5. Software	7
1.6. Outline.....	8
2. LITERATURE REVIEW	9
2.1. Introduction.....	9
2.2. Scale Saltwater Modelling	9
Dimensionless Governing Equations	10
Limitations of Saltwater Modelling	14
Boussinesq Assumption.....	14
Heat Transfer Deficiency.....	15
Initial Plume Momentum	15
Saltwater Source Geometry	16

Plume Mass Flux	16
2.3. Ceiling Vent Exchange Flows.....	17
Lock Exchange	17
Buoyant Plumes	19
Previous Computer Modelling.....	27
3. CONCEPTUAL MODELS.....	28
3.1. Introduction.....	28
3.2. Box Filling Model.....	28
3.3. Mass Conservation Model.....	32
3.4. Box Filling Model with Exchange Flow.....	34
4. EXPERIMENTAL SYSTEMS AND DESIGN	36
4.1. Introduction.....	36
4.2. Flow Visualisation Techniques.....	36
Light Attenuation.....	36
Ambient Tank Configuration.....	39
4.3. Camera.....	43
Camera Setup.....	43
Camera Setup Experiments.....	45
4.4. Calibration Experiments	48
4.5. Method Performance Check	51
4.6. Experimental Configuration	53
Initial Conditions	53
4.7. Equivalent Fire Size	57
4.8. Experimental Method	59
4.9. Data Analysis Methods	62
Layer Height	62
Plume Analysis	64
5. RESULTS AND DISCUSSION	68
5.1. Introduction.....	68
5.2. Experimental Observations.....	68
5.3. Layer Height.....	71

5.4. Plume Analysis	75
Free Plume Assumption.....	75
Horizontal Profiles.....	75
Vertical Profiles	79
5.5. Spread Assumption	82
5.6. Concentration Leaving Vent	88
Concentration Profile across Vent	88
Maximum Concentration Leaving Vent	89
5.7. Box Filling Model (Baines & Turner 1978).....	92
5.8. Layer Concentration.....	94
5.9. Exchange Flow.....	98
5.10. Cooper Comparison.....	100
5.11. Discussion.....	105
6. CONCLUSIONS	109
7. FUTURE WORK.....	112
8. REFERENCES	114
9. APPENDIX A.....	119
9.1. Matlab Algorithm.....	119
10. APPENDIX B.....	129
10.1. Dimensionless Layer Height Equation	129
11. APPENDIX C.....	131
11.1. Light Attenuation Equation Derivation	131
12. APPENDIX D.....	134
12.1. Concentration Profiles Across Vent	134
Three Percent Experiments.....	134

List of Figures

<u>Figure</u>	<u>Page</u>
Figure 1.1 - Compartment set up in the real life (top) and analogue (bottom) scenarios.	5
Figure 2.1 - Variable description used by Brown (left) and Epstein (right).	17
Figure 2.2 - Boundary values for problems of type 1 (left) and type 2 (right).	21
Figure 2.3 - Flooding Froude number (Figure 4 from Cooper 1994a).	22
Figure 2.4 - Flooding pressure (Figure 5 from Cooper 1994a)	23
Figure 2.5 - Flooding discharge coefficient (Figure 6 from Cooper 1994a)	24
Figure 3.1 - Conceptual model schematic	28
Figure 4.1 - Schematic drawing of source configuration	40
Figure 4.2 - Ambient tank photograph.	40
Figure 4.3 - Compartment photograph.	41
Figure 4.4 - Source tank photograph	41
Figure 4.5 - Magnetic flow meter calibration curve	42
Figure 4.6 - Plan view of setup showing parallax	43
Figure 4.7 - Schematic drawing of camera setup.	44
Figure 4.8 - Green gun light intensity at various shutter speeds	46
Figure 4.9 - Calibration profile of red dye response	49
Figure 4.10 - Background red image and dye filled compartment used in performance test.	51
Figure 4.11 - Experimental image showing the upper and lower layer	63
Figure 4.12 - Processed image of the compartment.	63

Figure 4.13 - Plume contour schematic	65
Figure 4.14 - Imagestream view of time averaged plume	65
Figure 5.1 - Plume formation after 2 s (L) and plume reaching ceiling after 6 s (R). . . .	69
Figure 5.2 - Ceiling jet reaching wall after 15 s (L) and deflected off wall after 24 s (R)	69
Figure 5.3 - Layer interface settling and descending after 45 s (L) and 90 s (R)	70
Figure 5.4 - Layer height for the 3 percent density difference	71
Figure 5.5 - Layer height for the 6 percent density difference	72
Figure 5.6 - Comparison of layer height definition for 50sq vs. 100sl	73
Figure 5.7 - Layer height in the compartment compared with that predicted in the model.	73
Figure 5.8 - Horizontal profile of the free plume	76
Figure 5.9 - Horizontal profile with compartment present.	77
Figure 5.10 - Time averaged horizontal profile comparison of the free and confined plumes.	78
Figure 5.11 - Vertical profile of the free plume	79
Figure 5.12 - Vertical profile with compartment present	80
Figure 5.13 - Time averaged vertical profile comparison of the free and confined plumes.	81
Figure 5.14 - Maximum centreline concentration for free and confined plumes	82
Figure 5.15 - Gaussian fit of integrated concentration profile for the free plume	83
Figure 5.16 - Gaussian fit of integrated concentration profile for the confined plume . .	84
Figure 5.17 - Plume spreading rate comparison for the confined and free plumes.	84
Figure 5.18 - Plume spreading rate comparison with Kikkert (2006)	85
Figure 5.19 - Layer height in the compartment with improved integral model.	86
Figure 5.20 - Dimensionless layer height data for three and six percent experiments. . .	87
Figure 5.21 - Vent exit concentration schematic	88
Figure 5.22 - Concentration profile across vent for 50 mm square opening.	89
Figure 5.23 - Maximum integrated concentration at vent exit for	90

the 3 percent density difference.	
Figure 5.24 - Maximum integrated concentration at vent exit for the 6 percent density difference.	90
Figure 5.25 - Dimensionless layer height model comparison	93
Figure 5.26 - Average layer concentration in the compartment	95
Figure 5.27 - Relative layer mass of 3 percent experiments	96
Figure 5.28 - Relative layer mass of 3 percent experiments	97
Figure 5.29 - Exchange flow through the opening	98
Figure 5.30 - Exchange flow constant	99
Figure 5.31 - Exchange flow rates calculated using Cooper's equations.	101
Figure 5.32 - Exchange flow rate comparison with Cooper - 3 percent.	102
Figure 5.33 - Exchange flow rate comparison with Cooper - 6 percent.	102
Figure 5.34 - Exchange flow constant comparison with Cooper – 3 percent.	103
Figure 5.35 - Exchange flow constant comparison with Cooper – 6 percent.	104

List of Tables

<u>Table</u>	<u>Page</u>
Table 4.1 - Camera set up experiments	47
Table 4.2 - Calibration experiment conditions	50
Table 4.3 - Pipe flow initial conditions	55
Table 4.4 - Experiments conducted	61

List of Notations

Latin

Symbol	Unit	Definition
<i>a</i>	-	empirical attenuation rate constant
<i>A</i>	m ²	cross-sectional area
<i>b</i>	-	rate of attenuation in fluid with no dye
<i>B</i>	m ⁴ /s ³	buoyancy
<i>c</i>	kg/m ³	average cross-channel dye concentration
<i>ch_f</i>	kg/m ²	integrated dye concentration
<i>c_p</i>	J/kgK	specific heat at constant pressure
<i>C</i>	m.kg/m ³	concentration
<i>C_D</i>	-	discharge coefficient
<i>d</i>	m	source diameter
<i>d_f</i>	-	optical thickness of fluid
<i>D</i>	m	compartment depth
<i>D_i</i>	m	circular vent diameter
<i>E</i>	-	exchange flow constant
<i>f</i>	-	calibration constant
<i>Fr</i>	-	Froude number
<i>g</i>	m/s ²	acceleration due to gravity
\bar{g}	m/s ²	gravitational acceleration vector
<i>g'</i>	m/s ²	reduced gravity
<i>Gr</i>	-	Grashof number
<i>h</i>	m	height of saltwater compartment
<i>H</i>	m	height of fire compartment
<i>I</i>	-	light intensity
<i>J</i>	m	depth of ceiling vent used by Brown (1962) and Epstein (1988)
<i>k</i>	W/mK	thermal conductivity
<i>k_T</i>	-	plume spread constant
<i>l</i>	m	spatial extent of saltwater source
<i>l_{jp}</i>	m	jet to plume transition length

L	m	length
\dot{m}	kg/s	mass flux of saltwater flow
M	m^4/s^2	momentum
O	m^2/s	mass diffusivity
P	kg/ms^2	pressure
\bar{P}	kg/ms^2	average pressure
Pr	-	Prandtl number
\dot{Q}	kW	heat flux
Q	m^3/s	flow rate
r	m	radius used by Baines & Turner (1978)
R	-	relative concentration or density
Re	-	Reynolds number
S	m	square vent width
Sc	-	Schmidt number
t	s	time
T	K	temperature
\bar{u}	m/s	velocity vector
U	m/s	velocity
V	m^3	volume
w	m/s	vertical velocity
W	m	width
Y	-	salt mass fraction
Z	m	layer height

Greek

Symbol	Unit	Definition
α	-	entrainment constant
Δ	-	dimensionless density difference
ε	-	dimensionless density difference used by Cooper (1994a, 1994b)
η	-	rate of light absorption
κ	m^2/s	thermal diffusivity
μ	kg/ms	dynamic viscosity

Π	-	dimensionless pressure
ξ	-	dimensionless layer height used by Baines & Turner (1978)
ρ	kg/m ³	density
σ	-	constant used by Cooper (1994a, 1994b)
τ	-	dimensionless time used by Baines & Turner (1978)
ν	m ² /s	kinematic viscosity

Subscripts

Symbol	Definition
0	initial or reference
a	ambient incoming fluid
B	bottom
c	contaminated outgoing fluid
D	discharge
E	exchange
f	fluid
$flood$	flooding condition
g	gas
h	high
i	integrated
I	at the interface
L	within the layer
l	low
max	maximum
min	minimum
net	net
s	saltwater
T	top
∞	infinity

1. Introduction

Unwanted fires which occur in domestic and commercial buildings produce heat and toxic gases that can lead to human fatalities. The smoke from such fires is known to lead to even more deaths than the heat itself (Cote 1997). The ability to predict the movement of smoke within an enclosed space is essential information for the design and use of these buildings. Further knowledge of this issue will lead to safer and more cost effective designs.

Like many natural phenomena, the flow of smoke is complex and measurements in smoky environments can be very difficult and expensive due to the build up of soot within the enclosure and on equipment, as well as the high temperatures involved. The practice of modelling smoke flows using saltwater visualisation techniques, such as the light attenuation (LA) method, has been widely adopted and is now an accepted way of modelling full scale experiments because it is relatively inexpensive and does not carry with it the inherent difficulties associated with taking measurements in high temperature, smoky environments.

Saltwater modelling involves the use of a saltwater analogue system to replicate the flow of hot fire gases into cool ambient air. This is done by injecting saltwater into a tank of fresh water to create the equivalent density difference seen in the fire compartment and generate buoyancy.

Enclosure vents can be categorised as being one of two types. The first of these is the vertical vent. These are vents such as doors and windows and are not dealt with explicitly here as there has already been significant work done in this area. Emmons provides a detailed summary of vertical vent flow calculation methods (Emmons 2002).

The second vent category is horizontal vents. These are vents in a ceiling or floor and could comprise of a burnt out skylight, a broken window or a purpose built heat or smoke vent. Research into these vents has not been as comprehensive as their vertical counterparts and can be complicated by an unstable density profile across the vent.

1.1. Research Impetus

Present understanding of buoyancy driven exchange flow through horizontal ceiling vents is limited. Current smoke transport calculations are most often carried out using standard vent flow models that do not accurately take in to account the buoyancy component of the flow. This can lead to poor design decisions if the engineer cannot accurately predict the amount of smoke being exchanged with the outside environment or the conditions within an enclosure.

1.2. Saltwater Modelling

The movement of smoke and hot fire gases through a ceiling opening in an otherwise closed compartment is a complex phenomenon and has not yet been well characterised. Previous attempts at computer modelling of the problem have been made (Mills 2004) but it was found that there was little experimental data available in the literature for the verification of results. The aim of this work is to generate a set of experimental data that can be used for comparison with previous/future computer modelling work. The experimental data will be obtained using saltwater modelling techniques for a range of suitable fire sizes and opening geometries.

The concept of using scaled saltwater models to investigate fire gas and smoke flows was first formally documented by Steckler *et al.* (1986). Since this time the technique has become an accepted way of modelling full scale experiments because it is inexpensive and does not carry with it many of the difficulties associated with taking measurements in high temperature environments. At reduced scales turbulent flows can be achieved more easily using water as the fluid medium as it has a lower kinematic viscosity than that of air (Steckler *et al.* 1986; Tieszen 2001).

The flow of saltwater down to and across the floor of a compartment into fresh water has the same fluid dynamics as hot air spreading across a ceiling into cool ambient air (Baum *et al.* 1995). The buoyant driving force, which is produced by the difference in densities across the fluids, is the same so these processes can be related when the viscous and heat transfer effects are small.

In order to gauge the effects of various parameters on the entrainment of the plume and flow through the opening, a variety of different parameters could be varied, namely:

- compartment size/configuration
- fire size (density difference)
- fire location
- ceiling opening geometry/location

This work will focus on using an approximately 1/10 scale room for the dimensions of the compartment. The size of fire that can be investigated is limited by a maximum density difference between fluids for which the concentration density relationship is valid. For this reason two relatively small fire sizes will be investigated.

The location of the fire will be such that there are no wall or corner effects which could limit the amount of entrainment into the fire plume. The location of the ceiling opening will also be far enough away from the plume that there is sufficient time for a ceiling jet to fully develop. A range of ceiling openings will be investigated which will consist of 1D rectangular slots and 2D square openings.

1.3. Background

Among the first models attempting to predict the behaviour of fire in a compartment were two-zone models. These types of models divide the area within a space containing a fire into two separate areas, the upper layer and the lower layer. Under most circumstances these zones are well defined. The upper layer is that which is against the ceiling and is filled with hot fire gases and smoke from the fire burning below. The upper layer will be hot (less dense) and will contain very little oxygen making the space untenable. The lower layer on the other hand is close to normal temperature and contains fresh air which feeds the fire. The layer height is defined as the interface between these two zones and is measured as the distance from the floor to the interface.

When a vent is present in the ceiling, smoke from the upper layer is able to escape and fresh air from the outside is able to enter the compartment. This is known as the exchange flow whose individual components can be high in or out of the vent, but the net effect of which is zero as the flows in each direction are equal.

When using a saltwater system to model this behaviour, the more dense fluid containing the salt acts in place of the fire source and the less dense fresh water acts as the cool air in the lower layer. For this reason it is necessary to conduct these experiments upside down to how they appear in real life scenarios. Both the fire and its saltwater analogue produce plumes which are a result of the less dense fluid rising (or falling in the saltwater system) and entraining ambient fluid as eddy currents develop due to the density difference. A schematic of the two-zone scenario is shown below in Figure 1.1. Throughout this report the conventions of the real life scenario will apply, i.e. the lower layer is that which contains the source, the upper layer is opposite this where the less dense fluid collects and the ceiling is the surface containing the vent.

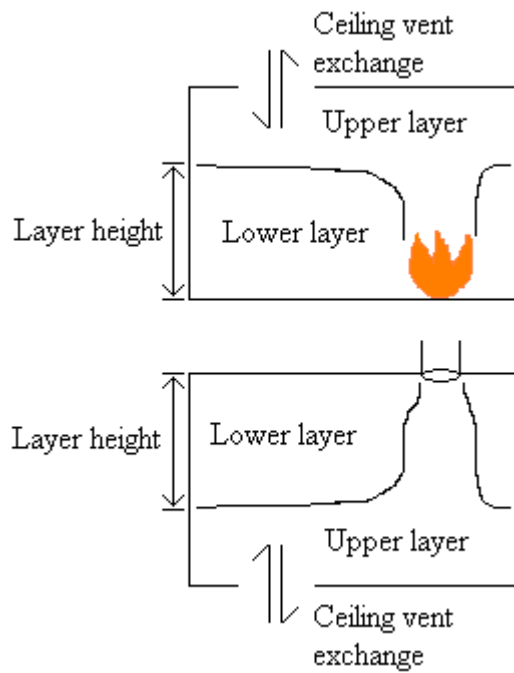


Figure 1.1 – Compartment set up in the real life (top) and analogue (bottom) scenarios

A number of ceiling vents are used in this study and these are of two types. There are slots which use the entire width of the compartment, and square vents. Slots are named with the form '50slot', for example, for a slot going across the width of the compartment that is 50 mm wide. A square vent that is 50 mm on each side has the form '50square'.

1.4. Research Objectives and Scope

This study will focus on the experimental modelling of buoyancy driven flow through horizontal ceiling vents arising from compartment fires. Experimentally, saltwater modelling and non-intrusive quantitative flow visualisation techniques will be applied.

The major research objective proposed for this study is:

To quantify the effect of different compartment opening geometries on the bulk flow characteristics and internal flow structure arising from fire gas exchange flow through horizontal ceiling openings.

Results of these investigations will be represented in a dimensionless manner. This is so that results can be compared easily with other research and also to help simplify which variables have the greatest effect on the flow outcome. Key variables of interest are:

- layer depth in the compartment
- flow rate in/out opening

1.5. Software

Throughout this project a number of software packages have been used to record and analyse the data. Adobe Premier 6.0 was used to record the data and store it as .avi video files. Premier was used to export these .avi files as single frame .tiff files so that they could be better analysed by Imagestream (Nokes 2006a, 2006b).

Imagestream is an image processing package and has an enormous amount of power for data reduction. Images were time averaged as required using this package and also filters were able to be applied so that the green signal from the digital camera could be isolated in order to track the attenuation of the dyed saltwater solution, which was red. Further to this the Imagestream package allows edge detection which detects when a particular light intensity is reached as well as the ability to average pixel intensity across the image. Imagestream can export data as .csv (comma separated variable) files allowing them to be read in Microsoft Excel where it can be further reduced to an appropriate form.

Matlab is employed as a computational tool to do some of the more demanding calculations required. In this case it is used to track the saltwater plumes and calculate the spread, maximum centreline concentration and to fit Gaussian profiles across the plumes. This is detailed further in section 4.9.

Throughout this project reference will be made to two specialist fire engineering software packages BRANZFire and the Fire Dynamics Simulator (FDS). BRANZFire was developed by Wade (2003) and is a zone model employing algorithms to track the effects of a fire in a compartment. FDS (McGrattan 2004a, 2004b, 2005) is a Computational Fluid Dynamics (CFD) package that uses the conservation equations for mass momentum and energy to simulate fire driven flows.

1.6. Outline

In Chapter 2 a literature review is presented discussing the saltwater modelling technique, its applicability to the problem and its limitations. Previous research is then discussed in terms of previous attempts at determining ceiling vent exchange flow as well as work to write an algorithm to model the problem and the difficulties arising from this.

In Chapter 3 a conceptual integral model is systematically developed which considers the descent of the layer within the compartment and uses this to predict exchange flow through the ceiling opening.

Chapter 4 details the light attenuation modelling technique and describes how the equipment was set up in order to achieve repeatability and reliability of results. Calibration experiments are also conducted and the experimental technique is described in detail. Analysis techniques that were employed in order to obtain the data required are also described. This primarily involves discussion of using Imagestream as an image manipulation package.

In Chapter 5 the experimental observations and results are detailed and the original experimental assumptions are investigated. Comparisons are made between the experimental results, the conceptual integral model previously developed and prior works. The major results are presented as well as discussion regarding the issues that came up throughout the course of the research.

Chapter 6 draws the major conclusions from the research and the possible direction of further work is considered in Chapter 7.

2. Literature Review

2.1. Introduction

In recent times, saltwater modelling has become a common way of modelling various phenomena, not just in the field of fire dynamics, but in a range of applications. Herein is presented a discussion of saltwater modelling techniques and how, through dimensional analysis, the saltwater analogue system can be used to provide insight into a real fire scenario.

The range of saltwater modelling work is vast and so this section also summarises the important relevant work done in this area to date and how it applies to the problem at hand. An outline of work done to attempt to write an algorithm and associated FORTRAN code for the exchange flow through a ceiling opening is presented as well as a comparison between the way BRANZFire and FDS deal with the problem.

2.2. Scale Saltwater Modelling

Since the initial work of Steckler *et al* (1986), saltwater modelling has become commonplace in the arsenal of methods available to researchers wishing to investigate density driven flows that occur in fire and in the environment. Saltwater modelling is relatively cheap and safe compared to other alternatives and has been used extensively by the likes of Epstein, Heskestadt and Linden (Epstein 1988, 1989; Heskestadt 1991; Linden 1999) among others for a vast range of applications.

Saltwater experiments are typically done at reduced scales and built from commonly available building materials such as polycarbonate sheet. This, along with the fact that the life of a compartment is significantly reduced when conducting full scale fire experiments leads to a far cheaper experimental alternative. Saltwater modelling also has an advantage in that the environment is very clean and flow visualisation is much easier. In high temperature environments taking accurate measurements is difficult as equipment can be damaged or clog up with soot.

Dimensionless Governing Equations

Various forms of the equations of motion which govern the buoyant flows seen in both thermally driven gas and density driven saltwater flows have been previously documented by Steckler *et al* (1986), Rehm and Baum (1978), Rehm *et al* (1997) and Clement (2000) among others. The fluid dynamics that are seen in real fire scenarios as hot air spreads across a ceiling are the same as those seen when as saltwater flows across the floor of a fresh water environment (Baum 1995). When the viscous and heat transfer effects are small these two processes can be related because the driving force, a buoyancy force driven by density differences, is the same in each case (Baum *et al.* 1995, Steckler *et al.* 1986). Scaled saltwater models can therefore be used to investigate full-scale fire scenarios. The similarity of these flows can be investigated through consideration of the dimensionless governing equations. At reduced scales, turbulent flows can be achieved more easily using water as the fluid medium as it has a lower kinematic viscosity than that of air (Linden 1999).

It is assumed in this analysis that changes in the density can be ignored everywhere except in the body force term. This is called the Boussinesq approximation and is valid as long as the density difference between fluids is small (less than approximately 10% (Shin *et al.* 2004)).

In order to correlate between a real fire scenario and what happens in a saltwater modelling experiment, each scenario must have the same set of governing equations. The equations used are the conservation equations for mass, momentum and energy. In the fire scenario energy means the thermal energy of the fire, in the saltwater example this is the concentration of the salt.

The equations for incompressible, inert buoyancy driven flow in a compartment are presented in equations 2-1 to 2-4 from Fleischmann (1994) and Weng and Fan (2002).

For temperature and density driven flow

$$\frac{\delta \rho}{\delta t} + \nabla(\rho \bar{u}) = 0 \quad \text{mass} \quad (2-1)$$

$$\rho \left[\frac{\delta \bar{u}}{\delta t} + (\nabla \bar{u}) \bar{u} \right] + \nabla P - \rho \bar{g} = \rho \nu \nabla^2 \bar{u} \quad \text{momentum} \quad (2-2)$$

For temperature driven flow

$$\frac{\delta T}{\delta t} + (\bar{u} \nabla) T = \kappa \nabla^2 T \quad \text{stratifying species - temperature} \quad (2-3)$$

For density driven flow

$$\frac{\delta Y}{\delta t} + (\bar{u} \nabla) Y = \kappa \nabla^2 Y \quad \text{stratifying species - density} \quad (2-4)$$

where Y salt mass fraction

$$\kappa = \frac{k}{\rho c_p} \quad \text{thermal diffusivity}$$

Making the Boussinesq assumption and rearranging gives equations 2-5 and 2-6 for mass and momentum respectively

For temperature and density driven flow

$$\nabla \bar{u} = 0 \quad \text{mass} \quad (2-5)$$

$$\frac{\delta \bar{u}}{\delta t} + (\nabla \bar{u}) \bar{u} + \frac{1}{\rho} \nabla P - \bar{g}' = \nu \nabla^2 \bar{u} \quad \text{momentum} \quad (2-6)$$

where \bar{g}' reduced gravity

Non-dimensional variables can be defined by selecting an appropriate scale relevant to the flow. Relevant scales include length scale H (enclosure height), the velocity scale U and the density scale $\Delta\rho$. Using these scales the following dimensionless variables are created:

$$\nabla^* = H \nabla \quad \text{dimensionless del operator} \quad (2-7)$$

$$t^* = \frac{t}{t_0} \quad \text{dimensionless time} \quad (2-8)$$

$$\text{where } t_0 = \left[\frac{d}{\Delta_0} \right]^{1/2}$$

$$\bar{u}^* = \frac{\bar{u}}{U} \quad \text{dimensionless velocity} \quad (2-9)$$

$$\rho^* = \frac{\rho}{\Delta\rho} \quad \text{dimensionless density} \quad (2-10)$$

$$P^* = \frac{P}{\Delta\rho U^2} \quad \text{dimensionless pressure} \quad (2-11)$$

$$T^* = \frac{T}{T_0} \quad \text{dimensionless temperature} \quad (2-12)$$

Using the dimensionless forms of the variables above, the non-dimensional forms of the governing equations of mass and momentum are presented.

For temperature and density driven flow

$$\nabla^* \bar{u}^* = 0 \quad \text{mass} \quad (2-13)$$

$$\frac{\delta \bar{u}^*}{\delta t^*} + (\nabla^* \bar{u}^*) \bar{u}^* + \frac{1}{\rho^*} \nabla^* P - 1 = \frac{Fr}{Re} \nabla^{*2} \bar{u}^* \quad \text{momentum} \quad (2-14)$$

The dimensionless equations for the conservation of species are given below in equations 2-15 and 2-16. The molecular transport terms are scaled by the Prandtl number for the diffusion of heat and the Schmidt number for the diffusion of salt.

For temperature driven flow

$$\frac{\delta T^*}{\delta t^*} + (\bar{u}^* \nabla^*) T^* = \frac{Fr}{Pr Re} \nabla^{*2} T^* \quad \text{stratifying species - temperature} \quad (2-15)$$

For density driven flow

$$\frac{\delta Y}{\delta t^*} + (\bar{u}^* \nabla^*) Y = \frac{Fr}{Sc Re} \nabla^{*2} Y \quad \text{stratifying species - density} \quad (2-16)$$

The dimensionless variables arising from the development of these dimensionless governing equations are presented in the following equations:

$$Fr = \frac{U_0}{(\Delta_0 d)^{1/2}} \quad \text{Froude number} \quad (2-17)$$

$$\text{Re} = \frac{U_0 d}{\nu} \quad \text{Reynolds number} \quad (2-18)$$

$$\text{Sc} = \frac{\nu}{O} \quad \text{Schmidt number} \quad (2-19)$$

$$\text{Pr} = \frac{\nu}{\kappa} \quad \text{Prandtl number} \quad (2-20)$$

Limitations of Saltwater Modelling

As with any scientific technique, saltwater modelling of real fire scenarios is only relevant within specific bounds and conditions. This section explores the limitations and assumptions required for saltwater modelling, and discusses ways to limit their effect on the experiments.

Boussinesq Assumption

In the derivation of the non-dimensional governing equations in the previous section a number of important assumptions have been made. These are:

- The length, time and temperature scales associated with the volumetric heat source are such that the addition of heat is slow. The implication of this is that the pressure over a large region of space is approximately uniform but not necessarily constant during heating. This does not imply restrictions on the magnitude of density or temperature variations during heating.
- It is the buoyancy effects which induce the flow velocities in the system. This relates the magnitude of the density variation and the velocities induced by the heat source.
- The vertical length scale of interest is much smaller than that associated with the static density variation. This implies that the variation of the static density from its mean is small.
- The density variations produced by the heat source are small.

Heat Transfer Deficiency

In any real fire in an enclosure there is a certain amount of heat transfer to the boundaries of the compartment. The result of this is a thermal boundary layer which is cooler than the general ceiling layer immediately adjacent to the compartment boundaries. This phenomenon cannot be directly simulated by saltwater modelling as this would necessitate mass transfer of salt into the surfaces of the model. This limitation means that this technique is not suitable for high temperature gas flows where heat transfer effects are important. It can be used for Boussinesq flows however, as the temperatures involved are low enough that heat transfer effects to the boundaries become negligible (Klote *et al.* 2004)

Initial Plume Momentum

In a real fire scenario the buoyant plume created by the fire has no initial momentum as the flow is driven solely by the density difference between the fire gases and the ambient air. In the case of saltwater modelling however, the rate of heat release of the fire is modelled using the mass flux of salt leaving the source. In order for a mass flux to exist the saltwater solution is required to be injected with a certain initial momentum. For the saltwater model to best represent the real fire scenario it is important to reduce this initial momentum as far as possible. There is a problem with this though in that the saltwater plume produced must be in a turbulent state as it would be in a real fire. For this to occur, the Reynolds number at the source, as given in equation 2-18, must be greater than approximately 3000 (Linden 1999).

$$\text{Re} = \frac{U_0 d}{\nu} \quad (2-18)$$

In practice the initial velocity of the source is a compromise between these two issues.

In a real scenario a turbulent fire plume has a Reynolds number on the order of 10^5 (Karlsson and Quintiere 2000). In the case of saltwater modelling the reduced length scale and the issues of initial momentum previously discussed mean that this cannot

be achieved. Turbulent plumes can exist as long as the Reynolds number is above approximately 3000. At Reynolds numbers above this figure the molecular transport terms in the governing equations become negligible compared with advective transport terms and the difference between the Prandtl number for air and the Schmidt number for water become negligible (Steckler *et al.* 1986).

Saltwater Source Geometry

In the derivation of the non-dimensional governing equations by Baum and Rehm (1978), the combustion zone is replaced by a volumetric heat source that has a specific heat release rate. While fire can be considered to be a volumetric heat source, the extent of its volume is constantly changing and is also very difficult to define. In the case of saltwater modelling it is not possible to release saline solution in a precisely scaled volume corresponding to the volumetric extent of a real fire. Therefore, the saltwater source geometry is assumed to be the diameter of the planar source.

Plume Mass Flux

In a real fire scenario the mass flux at the source of the fire is zero as there is no mass introduced into the system. When conducting a saltwater modelling experiment however, mass is introduced in the form of the more dense saltwater solution. In order for this point of difference to only have a negligible effect on the experiment care must be taken to ensure that the mass flux entraining into the plume some distance from the source is large compared with that at the source.

2.3. Ceiling Vent Exchange Flows

Upon conducting a review in the literature it was found that there was very little work previously done involving plume flows through a horizontal ceiling opening. However, there have been a number of experiments carried out using saltwater modelling techniques to investigate the flow through a horizontal vent that arises from two compartments filled with fluids of different densities which then have their separations removed. This technique is called lock exchange flow and whilst this is slightly different from the problem at hand, the work is relevant and is able to provide some valuable insights into what might be expected. An overview of buoyant plume work is also presented along with its applicability to the current study.

Lock Exchange

The following diagram in Figure 2.1 is used to indicate the vent arrangements used by Brown and Epstein in their experiments.

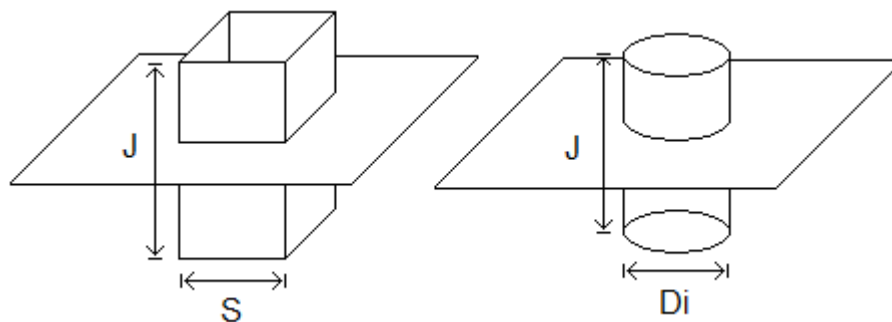


Figure 2.1 – Vent arrangements used by Brown (left) and Epstein (right)

Brown 1962

In his experiments, Brown used air as the fluid medium and imposed a temperature difference between two compartments to induce buoyancy driven exchange (countercurrent) flow through square openings. Brown presented results for a series of square openings which had opening depth to vent width ratios, J/S , in the range of 0.0825 to 0.66. This differs from the experimental setup used in this study which uses a flat opening that is approximately 10 mm in thickness and does not protrude from

the level of the ceiling. This equates to an equivalent J/S ratio of 0.25 for the 50 mm square opening and a ratio of 0.1 for the 100 mm square opening. Note that Brown used square openings only whereas rectangular openings are also considered in this work.

While Brown expressed his results as a Nusselt number versus Grashof number correlation, these can be re-expressed in terms of a functional relationship between the exchange flow rate, the density difference, J/S, and S. A major result from this work is that the exchange flow rate increases with increasing J/S.

Epstein 1988

Using simplistic saltwater modelling techniques, Epstein investigated the exchange flow between two compartments of different density fluids with circular horizontal ceiling vents. The fluids used in this case were brine as the more dense fluid and fresh water as the less dense. In these experiments a series of vent length to diameter ratios were investigated in the range of $0.01 < J/D_i < 10$.

This series of experiments was designed to investigate pure buoyancy driven flow through the vents and no artificial pressure differences were imposed. This allowed a bi-directional flow to develop between the two spaces. Four different flow regimes were found as J/D_i was increased through the range.

Epstein found that the exchange flow rate was, for practical purposes, to be independent of viscosity. This enabled him to develop a universal correlation between the Froude number (dimensionless exchange flow rate) and J/D_i.

Epstein and Kenton 1989

Epstein's work was then expanded to include investigations into the flow rate required to overcome bi-directional flow for a series of vent geometries. Similar saltwater modelling techniques using brine and fresh water were again used to simulate compartment density differences. The experimental apparatus was slightly modified to include the ability for water to be removed or added from the bottom compartment

at a specific rate. This allowed an adjustable pressure difference to be added across the vent.

By adjusting the drainage or supply rate until the buoyant flow was arrested, an empirical formula was obtained to calculate the flow rate that is required to prevent countercurrent flow within a horizontal ceiling opening. This relates directly to the work of Cooper describe below who used a flooding Froude number to determine the point at which the flow between compartments failed to be bi-directional and became uni-directional. As this investigation concerns bi-directional exchange flow it is essential that the experiments are not in the region where bi-directional flow may be arrested.

Heskestad and Spalding 1991

Further work investigating the flow rate required to prevent smoke transport across vents was carried out by Heskestad and Spalding. The authors used air as the fluid medium in this case conducting mainly small scale experiments with some full scale experiments carried out for validation of results.

Buoyant Plumes

Linden *et al.* (Hacker *et al.* 1996; Hunt *et al.* 2001; Lin *et al.* 2002, 2005; Linden 1999; Rooney *et al.* 1997)

In a series of papers over a number of years Linden *et al.* have used saltwater modelling to simulate thermal forces in buildings for the purposes of building ventilation system design and control as well as considering fire design applications. His work deals with both mixing ventilation (exchange flow) and displacement ventilation which has an outlet as well as an inlet to a compartment. The key difference between this work and the work of those mentioned previously is that instead of using the lock exchange technique, turbulent buoyant plumes were used to create the density difference. This makes it directly relevant to the work at hand and has direct correlation to fire induced flows.

The work of Linden *et al.* is now seen to be invaluable to our understanding of how air is distributed and moves around a building. Furthermore we now have available through this research very good understanding of issues such as box filling, plume similarity and thermal stratification.

Thermal stratification occurs when, to consider a real life fire example in say an atrium, the fire gases rise from the source entraining air into the plume which cools the smoke and causes it to lose momentum. This then leads to the simple two-zone model of a fire compartment breaking down as the layer will form before it reaches the ceiling which can endanger occupants on a lower level than previously considered and needs to be taken into account in design. In this set of experiments the similar situation is if the concentrated source solution were to be sufficiently diluted before reaching the ceiling so that there was no longer a density difference between the plume and the ambient fluid and stratification would occur.

Kelly 2001

Kelly used a combination of both saltwater modelling and CFD modelling to investigate the movement of fire gases throughout a two storey compartment separated by a ceiling vent. A large compartment was modelled in the Fire Dynamics Simulator for these experiments that was 2.67 m x 6.23 m x 7.12 m high. A 1/10th scale model was used for the saltwater modelling again using turbulent buoyant plumes to introduce the saltwater.

These two modelling techniques were compared by analysing the arrival of the smoke or salt front at six different points throughout the structure. The results showed that there is one dimensionless time for the front to arrive at a particular point regardless of the strength of the source, and that this time is approximately the same in both systems. This further supports and somewhat validates the use of CFD modelling for continued investigation of fluid exchange through horizontal ceiling openings and it is recommended as a target of further study.

Cooper 1994a, 1994b

In 1994 Cooper published an algorithm to calculate the flow through shallow horizontal ceiling openings and used this to develop FORTRAN code for the problem. Cooper divides the problem into two distinct configurations depending on the boundary conditions portrayed in Figure 2.2 below.

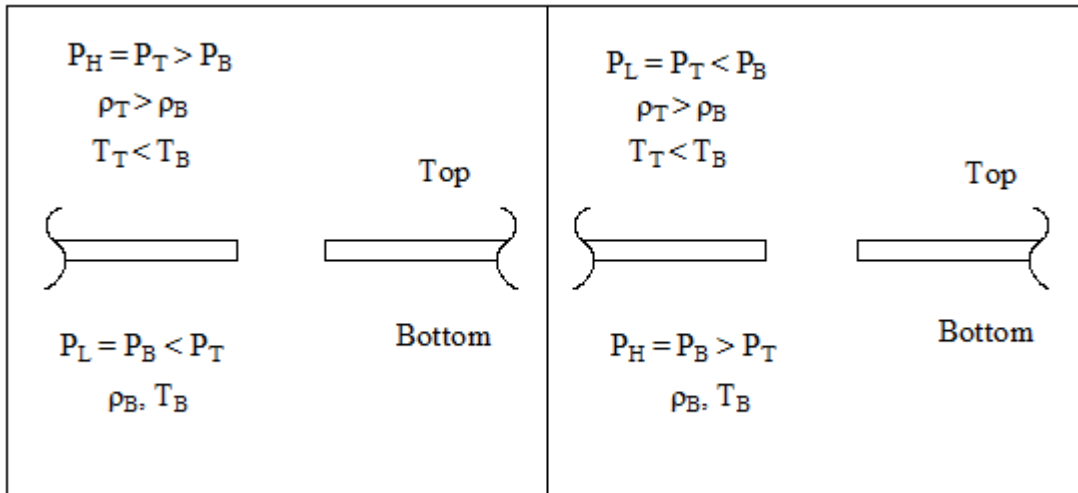


Figure 2.2 – Boundary values for problems of type 1 (left) and type 2 (right)

An unstable configuration with net flow from the top of the vent to the bottom is designated type 1 and vice versa for type 2. All experiments conducted herein are of the type 2 configuration as less dense fluid is rising due the buoyancy force and travelling upwards and out the vent.

Coopers work was based on some of the research previously discussed, namely Brown (1962), Epstein (1988, 1989) and Heskestadt (1991). An empirical correlation was found for $Fr_{h, flood}$ which is the Froude number for the flow rate associated with the point at which the flow overcomes the normal exchange flow nature of the vent and results in unidirectional flow. Cooper then plotted this against the relative density, $\epsilon = \Delta\rho / \rho$, to develop the following analytical equation using a least squares fit. This graph is reproduced here as Figure 2.3.

$$Fr_{h, flood} = 0.1754 \exp(0.5536\epsilon) \quad (2-21)$$

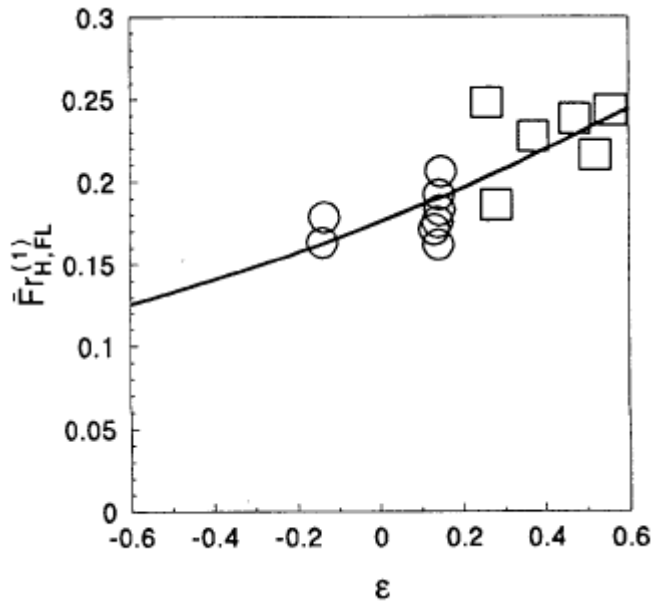


Figure 2.3 – Flooding Froude number (Figure 4 from Cooper 1994a)

Equations for the dimensionless pressure when flooding commenced was also developed and these are presented in equations 2-21 and 2-22.

$$\Pi_{flood} = \frac{\Delta P_{flood}}{4g\Delta\rho Di} \quad (2-22)$$

$$\Pi_{flood}(\epsilon) = 0.2427 \left(1 + \frac{\epsilon}{2} \right) \exp(1.1072\epsilon) \quad (2-23)$$

Figure 2.4 shows the flooding pressure graph reproduced from Cooper (1994a)

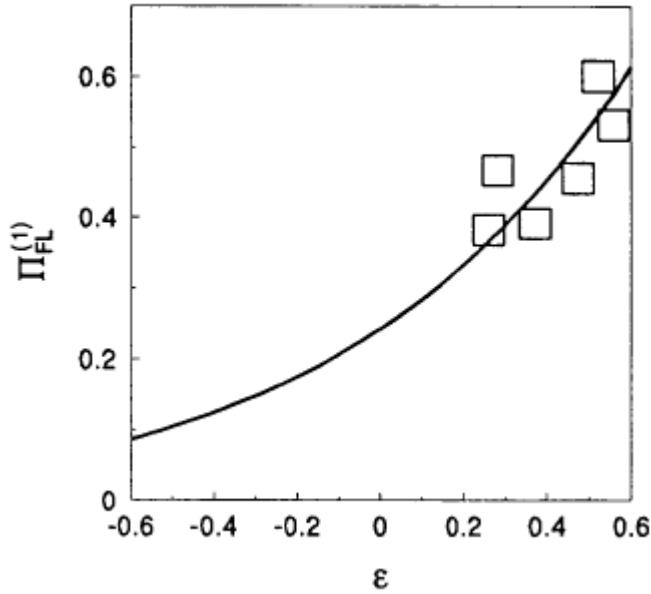


Figure 2.4 – Flooding pressure (Figure 5 from Cooper 1994a)

Using equations 2-21 and 2-23 the magnitude of the unidirectional flow can be found as well as the pressure difference it occurs at. Above the flooding pressure difference the standard flow model can be used. This requires a discharge coefficient, C_D , to be calculated and it was found that this was not constant and varied as the pressure difference approached ΔP_{flood} . Cooper analysed the data from a number of researchers and found the relationship shown in equation 2-24.

$$\frac{C_D}{C_{D,\infty}} = \frac{Fr_h / Fr_{h,flood}}{\left[\left(Fr_h / Fr_{h,flood} - 1 + \sigma_2^2 \right)^2 + \sigma_1^2 - \sigma_2^4 \right]^{1/2}} \quad (2-24)$$

where σ_1 and σ_2 were by least squares fit to available $\frac{C_D(\Pi, \epsilon)}{C_{D,\infty}}$ data. The values of

the constants were found and they were: $\sigma_1 = 3.370$ and $\sigma_2 = 1.045$. Cooper concedes that there may be a trend in the value of σ_2 if more data were available and whilst possibly not strictly correct it provides a figure to work with where there are no better estimates.

Figure 2.5 shows the flooding discharge coefficient reproduced from Cooper 1994a.

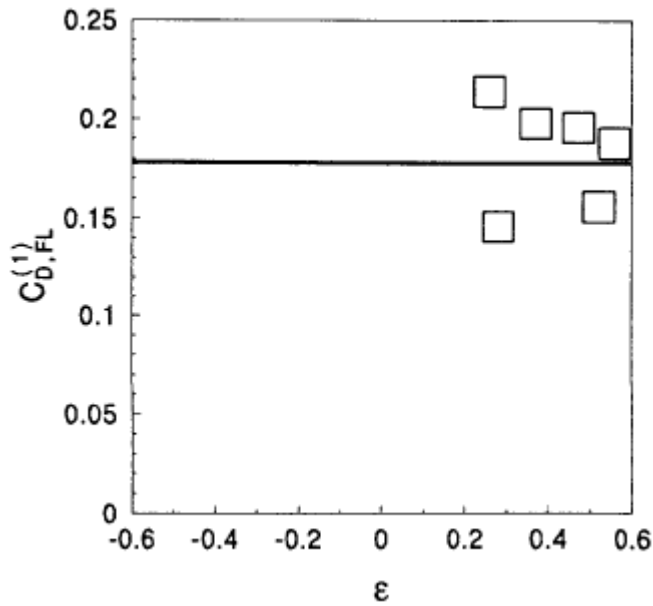


Figure 2.5 – Flooding discharge coefficient (Figure 6 from Cooper 1994a)

Equations for both flow schemes, the mixed flow and the unidirectional, were developed and these were combined into a model to estimate the flow through shallow horizontal ceiling vents. The VENTCF2 algorithm can be performed by following these steps:

Step 1

Ensure that there is an unstable density profile present ($\rho_T > \rho_B$) (the configuration is unstable) and calculate $\Delta\rho$. Find the average temperature and evaluate the viscosity, μ , and the average density, ρ , at this temperature.

The kinematic viscosity in m^2/s , $\nu = \mu / \rho$ can be determined from Hilsenrath (1955), where T is in Kelvin.

$$\nu(T) = \frac{0.04128(T)^{5/2}(10^{-7})}{T + 110.4} \quad (2-25)$$

Step 2

Determine the high and low pressures (P_h, P_l), the pressure difference (ΔP) and the average pressure (\bar{P}). Designate the problem as either type 1 or type 2.

Type 1 problems are of the form:

$$P_h = P_T > P_B,$$

$$\rho_T > \rho_B$$

$$T_T < T_B$$

Type 2 has the opposite pressure profile, i.e. $P_1 = P_T < P_B$. If problem is of type 2 replace ε in the following equations with $-\varepsilon < 0$.

Step 3

Evaluate the Grashof number according to equation 2-26.

$$Gr = \frac{2gDi^3|\varepsilon|}{(\mu T / \rho)^2} \quad (2-26)$$

Verify that the result satisfies the large Grashof number criterion of $Gr \geq 2 \times 10^7$.

Step 4

Calculate the following:

$$Fr_{h,flood} = 0.1754 \exp(0.5536\varepsilon) \quad (2-21)$$

$$Q_{h,flood} = 0.1754 \sqrt{2gDi|\varepsilon|} A_E \exp(0.5536\varepsilon) \quad (2-27)$$

$$\Delta P_{flood} = 0.2427 \left(1 + \frac{\varepsilon}{2}\right) \exp(1.1072\varepsilon) (4g\Delta\rho Di) \quad (2-28)$$

Step 5

If $\frac{\Delta P}{\Delta P_{flood}} \geq 1$ the flow regime will be unidirectional

$$Q_l = 0$$

$$Q_h = \frac{1 - \sigma_2^2 + [\sigma_2^4 + \sigma_1^2 (\Delta P / \Delta P_{flood} - 1)]^{1/2}}{Q_{h,flood}} \quad (2-29)$$

Step 6

If $\frac{\Delta P}{\Delta P_{flood}} < 1$ the flow regime will be mixed

$$Q_{net} = \frac{M - [1 + (M^2 - 1)(1 - \Delta P / \Delta P_{flood})]^{1/2}}{M - 1} Q_{h,flood} \quad (2-30)$$

$$Q_{E,max} = 0.055 \left(\frac{4}{\pi} \right) A_E \sqrt{gDi|\varepsilon|} \quad (2-31)$$

$$Q_l = \frac{[(1 + m_3/2)(1 - \Delta P / \Delta P_{flood})^2 - (2 + m_3/2)(1 - \Delta P / \Delta P_{flood})]^2}{Q_{E,max}} \quad (2-32)$$

$$Q_h = Q_{net} + Q_l \quad (2-33)$$

where $M = 2m_1 - 1 = \left(\frac{\sigma_1}{\sigma_2} \right)^2 = 9.400$

$$m_2 = \frac{d(Q_l / Q_{h,flood})}{d(\Delta P / \Delta P_{flood})} \Big|_{\frac{\Delta P}{\Delta P_{flood}}=0}$$

$$m_1 = m_2(\varepsilon) \frac{Q_{E,max}}{Q_{h,flood}}$$

Cooper used this algorithm to write an equivalent Fortran 77 subroutine (Cooper 1994b) which was converted by Wade (Wade 2003) to Visual Basic code for use in the BRANZFire zone model.

Previous Computer Modelling

Mills 2004

As stated above, when Cooper was writing his shallow horizontal ceiling vent algorithm in 1994 he found that there was very little data in the literature from which to develop a robust computer model of the problem. When Wade used this algorithm in the BRANZFire zone model it was with some uncertainty but this was all the data that was available at the time. A decade after Coopers effort, Mills revisited this problem in an attempt to expand on Coopers work with further available data. Unfortunately he found that there was little more available work on the subject than that which Cooper had used.

Mills then went on to compare the flow results obtained from using BRANZFire with those generated from the Computational Fluid Dynamics (CFD) package the Fire Dynamics Simulator (FDS). It is important to note that a comparison between computer packages is not a validation. Although each model is constructed independent of the other it is still possible that, for example, there is a common flaw in the equations that make up the models. CFD models such as FDS can overcome this issue to a certain extent as they have been shown to reproduce experiments with a high level of accuracy. This means in some circumstances CFD models can be used in place of experiments but they are by no means perfect and experimental validation is still required for results to be used with confidence.

Mills found that in BRANZFire, ceiling vented fire predictions contained errors that compound as the simulation progresses. A lack of quality entrainment modelling for the incoming air meant that while early predictions of layer height and upper zone temperature were reasonable, these became worse as the simulation progressed. Mills' study therefore already indicates that there are issues with the BRANZFire modelling of ceiling vent flows (and hence with the equations on which they are based) and this study will aim to highlight where some of these issues lie and provide guidance as to how to improve the model.

3. Conceptual Models

3.1. Introduction

In order to help explain the observations that are occurring in the experiments a relatively simple integral model is proposed. This model will use volume and buoyancy conservation conventions as a basis for predicting the experimental behaviour by considering firstly the descent of the layer in the compartment and then provide a way of determining the mass flow through the ceiling vent.

3.2. Box Filling Model

The model is based on the salt water analogue of a room fire scenario and is described schematically in Figure 3.1.

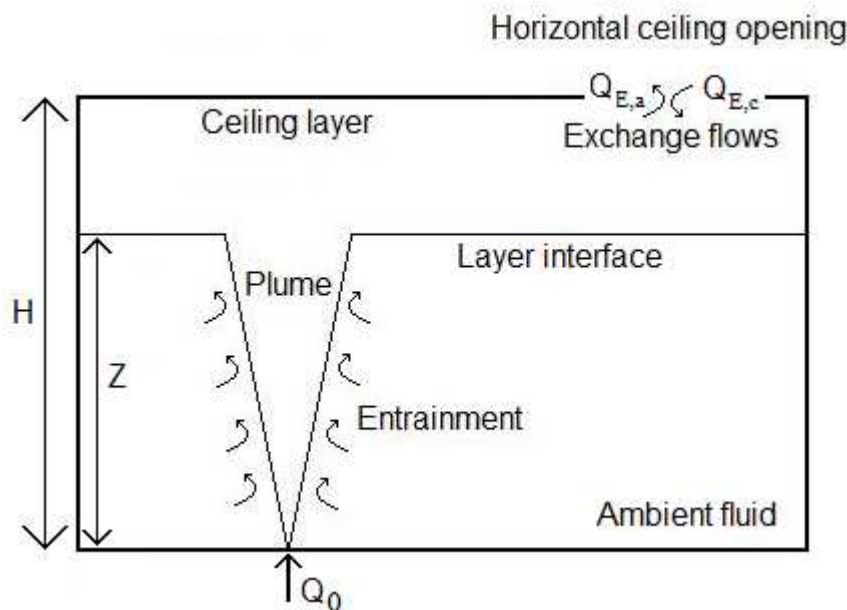


Figure 3.1 – Conceptual model schematic

In the model a room of height, H , width, W and depth, D contains an inlet source on the floor of the room with a buoyancy, B_0 . In the case of the salt water analogue the buoyancy force is created by the inlet source flow, Q_0 , with a dimensionless density difference as given in equation 3-1.

$$\Delta_0 = g \left(\frac{\rho_a - \rho_0}{\rho_a} \right) \quad (3-1)$$

The plume rises from the inlet source on the floor of the compartment, entraining air as it does so. The mixed fluid then accumulates at the top of the compartment forming the ceiling layer. The interface between the mixed and ambient fluid is at height z_I and upon reaching this point the plume discharge is Q_I . When simulating an equivalent real fire scenario it is important that Q_I is much greater than Q_0 , the source flow rate. This is because a real fire does not introduce additional fluid into the system and hence the amount of entrained fluid must be much more than the introduced fluid so that it can be considered to be negligible.

The ceiling vent has an area A_E and takes the form of either a rectangular slot across the width of the compartment, or a square opening. This is done to simulate a skylight, which is a common form ceiling openings in real buildings take. There is a buoyancy driven flow through the ceiling opening of ambient fluid flowing into the compartment and contaminated fluid from the ceiling layer exiting the compartment. These flow rates will be exchange flows and are designated Q_{Ea} , for the ambient incoming fluid and Q_{Ec} , for the contaminated outgoing fluid. The net flow rate for the opening will be Q_0 , i.e. equal to the amount of fluid introduced at the source.

In order to help understand the processes which are occurring in the compartment a simple box filling model was developed. The model has no exchange flow and is similar to that developed by Baines and Turner (1969) but has been adapted for this specific scenario. Initially volume conservation conventions are applied to the ceiling layer accumulating at the top of the compartment.

$$\frac{dV}{dt} = Q_I \quad (3-2)$$

Equation 3-2 defines Q_I which is the flow rate of fluid at the interface, i.e. that which is accumulating in the top layer and is equal to the flow from the inlet source coupled

with the additional fluid which is entrained into the plume as it rises. It is assumed that $Q_I \gg Q_0$ as discussed above. Using the compartment dimensions we obtain:

$$WD \frac{d(H - z_I)}{dt} = Q_I \quad (3-3)$$

Therefore:

$$\frac{dz_I}{dt} = \frac{-Q_I}{WD}$$

Substituting this expression into equation 3-4 below defining the flow rate of the plume and then integrating allows us to arrive at an expression for the height of the layer over time.

$$Q_I = \left[3 \frac{\pi^2}{4} B_0 k_T^4 \right]^{1/3} z^{5/3} \quad (3-4)$$

where $B_0 = Q_0 \Delta_0$

$$z_I = \left[\frac{1}{\frac{1}{H^{2/3}} + \frac{3}{2} \frac{1}{WD} \left[3 \frac{\pi^2}{4} B_0 k_T^4 \right]^{1/3} t} \right]^{3/2} \quad (3-5)$$

N.B. At $t=0$ the interface is at height H .

This layer height model can now be used as a guide to how the plume in the experiments is behaving. The model described above predicts that the size of a ceiling opening and indeed if one is present at all, should not affect the layer height under this scheme. This is because the opening is exchanging with only fluid that is in the layer and this is a bidirectional exchange flow whose net flux through the opening is zero in the real fire scenario and should be negligible in the saltwater analogue. It is

important to note some of the assumptions that are inherent in this model. The model assumes turbulent flow immediately from the exit at the source, which is seen in a real fire scenario but is unable to be replicated in the saltwater analogue as there is an initial zone in which the turbulent plume forms.

For the model it is assumed that the plume behaves the same within the compartment as it would if it were simply a free plume with no boundaries. This is important as if the entrainment into the plume was restricted and this was not reflected in the model, then this would lead to a discrepancy. The spread of the plume is assumed to be constant and have a spread constant, k_T , for the model of 0.15 (Kikkert *et al.* 2007).

This model does not take into account any mixing along the interface between the two layers.

In order to advance the model further it is now easiest to consider it in dimensionless form, the derivation of which can be found in detail in Appendix B but the resulting equation is given here as equation 3-6.

$$\frac{z_I}{H} = \frac{1}{\left[1 + \left[\frac{3^4}{2^3} \pi \frac{H}{D} \frac{H}{W} \left(\frac{\beta}{\gamma} \right)^2 Fr_0 k_T^4 \right]^{1/3} t^* \right]^{3/2}} \quad (3-6)$$

where

$$t^* = \frac{t}{t_0}, \quad t_0 = \left[\frac{d}{\Delta_0} \right]^{1/2}, \quad \beta = \frac{\pi}{4} d^2, \quad \gamma = DW$$

It should be noted that:

$$\frac{B_0}{\Delta_0^{3/2} H^{5/2}} = \frac{\pi}{4} \left(\frac{d}{H} \right)^{3/2} Fr_0 \quad (3-7)$$

Where F_0 is the densimetric Froude number, $U_0/(\Delta_0 d)^{1/2}$, which is a typical way of characterising plumes; U_0 and d are the velocity and diameter of the inlet source respectively.

3.3. Mass Conservation Model

The box filling model can now be expanded with the aim of using it to predict the amount of contaminant present in the ceiling layer. It is important to note that the effects of the ceiling opening are still not being taken into account at this time as this will affect the concentration of contaminant in the ceiling layer. Mass conservation dictates that the flux of contaminant entering the ceiling layer is equal to the contaminant flux at the inlet source.

$$Q_1 C_1 = Q_0 C_0 \quad (3-8)$$

where C_1 is the average contaminant concentration entering the ceiling layer and C_0 is the initial contaminant concentration. Therefore the total mass of contaminant in the ceiling layer can be defined by:

$$C_L V_L = \int_0^t C_0 Q_0 dt \quad (3-9)$$

where C_L is the average contaminant concentration in the layer and V_L is the volume of the layer. Again it has been assumed that $Q_1 \gg Q_0$. Equation 3-9 can now be integrated with the compartment dimensions substituted in to express the layer concentration in the following form:

$$C_L = \frac{Q_0 \Delta_0 t}{WD(H - z_1)} \quad (3-10)$$

N.B. the constant of integration is zero in this case. In non-dimensional form this can be expressed as follows:

$$\frac{C_L}{C_0} = \frac{H^2}{WD} \frac{B_0}{\Delta_0^{3/2} H^{5/2}} \frac{t^*}{1 - \frac{z_L}{H}} \quad (3-11)$$

This study uses a light attenuation technique to examine these flows experimentally and this system measures spatially integrated concentration fields. It is advantageous at this time to consider the model in terms of this width integrated information so that the model and the experiments can be compared more readily. The maximum integrated contaminant concentration at the source (designated C_{0i}) is C_0d and the average integrated contaminant concentration in the ceiling layer (designated C_{Li}) is $C_L D$. Therefore equation 3-11 can be rewritten utilising integrated terms as follows:

$$\frac{C_{Li}}{C_{0i}} = \frac{C_L D}{C_0 d} = \frac{H^2}{dW} \frac{B_0}{\Delta_0^{3/2} H^{5/2}} \frac{t^*}{1 - \frac{z_L}{H}} \quad (3-12)$$

3.4. Box Filling Model with Exchange Flow

As noted previously the position of the layer interface should be independent of the exchange flow and therefore equation 3-6 still remains valid at his time. However the contaminant concentration within the layer will change once the ceiling opening is taken into account as the layer exchanges fluid with the ambient environment outside the compartment. For this reason, equations 3-11 and 3-12 apply for closed compartments only.

Conserving mass in the ceiling layer gives the following equation:

$$\frac{d}{dt}(\Delta_L V_L) - Q_0 \Delta_0 + \Delta_L Q_{Ec} = 0 \quad (3-13)$$

Using the data which is available to us experimentally, i.e. C_{Li}/C_{0i} , the above equation can be solved for the exchange flow which is expressed in dimensionless form by dividing by the inlet flow.

$$\frac{Q_E}{Q_0} = \frac{C_{0i}}{C_{Li}} \frac{D}{d} \left[1 - \frac{d}{D Q_0} \frac{d}{dt} \left(\frac{C_{Li}}{C_{0i}} V_L \right) \right] \quad (3-14)$$

It has been assumed in the above equation that the buoyancy of the ceiling layer is representative of the buoyancy at the ceiling opening.

Dimensional arguments will provide some guidance as to the expected form of the exchange flow. Noting that the compartment is not pressurised and therefore the exchange flow is only dependant on the buoyancy of the fluid and the area of the ceiling opening (A_E) we can write:

$$U_E \propto \Delta_L, A_E$$

This dependency can be represented by the following relationship:

$$U_E \propto [\Delta_L \sqrt{A_E}]^{1/2}$$

Multiplying both sides by the area of the opening,

$$Q_E \propto [\Delta_L \sqrt{A_E}]^{1/2} A_E$$

$$Q_E \propto \Delta_L^{1/2} A_E^{5/4}$$

Hence

$$\frac{Q_E}{\Delta_L^{1/2} A_E^{5/4}} = \text{const.} = E \quad (3-15)$$

where E is a constant for a given type of ceiling opening and is known herein as the exchange flow constant.

4. Experimental Systems and Design

4.1. Introduction

This chapter describes the light attenuation method and the theory behind it as well as the general set up of the ambient tank and the source feed system. Also explained are how the camera is set up and the experiments conducted in order to ensure there was repeatability in the system.

Calibration experiments are presented which are required to confirm the linear relationship between light attenuation and the dye concentration, as well as providing an upper bound above which this relationship does not apply. Finally a check of the light attenuation method is made to confirm the technique is performing to a satisfactory level.

This chapter then describes the saltwater experiments undertaken in detail. The configuration as well as the method of the experiments is explained as are the source conditions. The derivation of the fire size which corresponds to a particular saltwater density is also made.

4.2. Flow Visualisation Techniques

Light Attenuation

The basis of the LA system lies in the relationship between the amount of dye which the light has to pass through and the associated decrease in the intensity of that light. It was found that the attenuation of light that passes through a dyed fluid can be used to measure the concentration of dye in that fluid (Hacker *et al.* 1996). Densities caused by dissolved salts can be determined as they are linearly proportional to dye concentration for low concentrations. The data from a light attenuation experiment is integrated over the width through which the light passes. As a result LA is able to provide high quality information for the flow as a whole because the signal does not

diminish as quickly with increasing distance from the source as it can with other visualisation techniques.

During an LA experiment, a uniform source of white light is directed through a dyed fluid and all other possible sources of light are removed. As the light travels through obstructions and interfaces its intensity is attenuated as it is absorbed (due to travel through air, water, glass etc.), reflected (for example from an air – water interface) or dispersed over distance. The difference between the light intensity as it passes through a fluid that is dyed and one that is not is due to the attenuation of the dye. If the relationship between the light intensity and the dye attenuation is known, then this can be used to determine the concentration of the dye and therefore the density of the fluid.

One of the first uses of light attenuation theory was in the investigation of 2-D lock exchange gravity currents (Hacker *et al.* 1996). For these experiments it was assumed that the light attenuation was linearly dependent on dye concentration, c , according to the following equation.

$$c = c_0 f \left(\frac{I_0}{I} \right) \quad (4-1)$$

Where I is the intensity of light received and f is the calibration constant calculated from the relationship between light intensity and dye concentration.

Further to this a more advanced relationship was developed by Cenedese and Dalziel (1998) who were able to show that the intensity of light which passes through a dyed fluid will decay exponentially with integrated dye concentration. The derivation of this equation is included in Appendix C.

$$ch_f = a \ln \left(\frac{I_0}{I} \right) = ad_f \quad (4-2)$$

$$d_f = \ln \left(\frac{I_0}{I} \right) \quad (4-3)$$

It is important to note that while this relationship is valid for low concentrations, it does not hold for higher dye concentrations (Cenedese and Dalziel 1998). The point at which this equation no longer applies can be determined by incrementally adding small amounts of dye to the solution and determining at which point the integrated dye concentration and optical thickness relationship ceases to be linear.

If the maximum dye concentration is known (set), and the optical thickness is measured, then any dye concentration can be determined as a fraction of the maximum. The relative mixing, R , can be determined and is equal to the relative density for low salt concentrations. It is effectively a measure of the extent of mixing which has occurred as an R value of 1 corresponds to unmixed solution and a value of 0 corresponds to ambient fluid. R is shown in the equation below. A constant width of integration is assumed.

$$R = \frac{c}{c_{\max}} = \frac{\ln\left(\frac{I_0}{I}\right)}{\ln\left(\frac{I_0}{I_{\max}}\right)} = \frac{d}{d_{\max}} \quad (4-4)$$

Cenedese and Dalziel (1998) found that the level of light attenuation was a function of wavelength as well as a function of dye concentration. They found that red dye has a region of constant response at approximately 510 nm. This wavelength corresponds to green light. Green light can be selected either through placing a green filter on the camera lens, or by selecting only the green gun (and disregarding the blue and red guns) on the digital camera or the related software.

The optical thickness was found by Kikkert (2006) to also be dependent on the intensity of the background lighting as well as the temperature. The background lights were left to heat up for a period of time prior to an experiment to ensure that the air surrounding them also has a chance to heat up. Spatial variations in background lighting can be overcome by time averaging data and subtracting the reference image from a recording so that such variations are eliminated. Fluid temperatures were also

allowed to reach a steady state prior to an experiment being carried out so that variations in this regard are minimised.

Ambient Tank Configuration

During the light attenuation experiments, the control of the amount and direction of light in the room is very important and so all experiments are carried out in a darkroom. The ambient tank used for these experiments has internal dimensions of (length x width x height) 1068 mm x 1072 mm x 624 mm. The tank had windows on the bottom and all sides and these were constructed out of glass for the sides and polycarbonate sheet for the bottom.

The source solution was fed from a source tank 3.6 m above the bottom of the main tank. This tank used a small pump to push the mixture up to a constant head tank whose overflow ran back into the source tank and also acted to circulate the fluid as a way of providing additional mixing of the solution. From the constant head tank the source solution ran down through a magnetic flow meter and out of the source pipe. Covering the tank when it was not being used acted to minimise evaporation and therefore changes to the concentration of the source solution. Figure 4.1 below shows the source tank configuration.

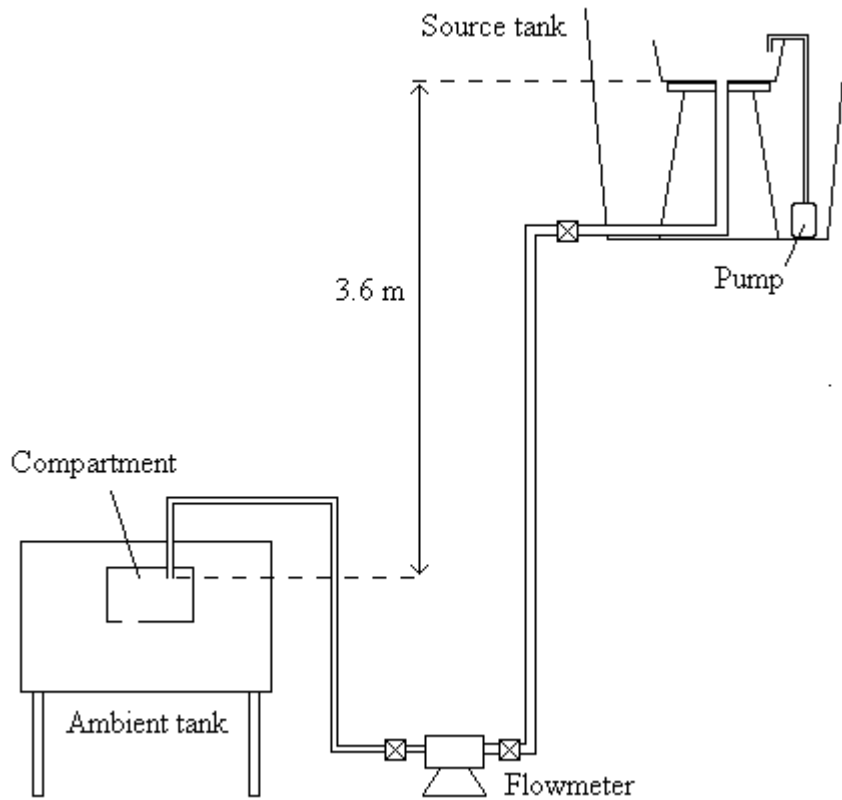


Figure 4.1 - Schematic drawing of source configuration

Photographs of the experimental set up are shown below depicting the ambient tank in Figure 4.2, the compartment suspended inside the tank in Figure 4.3 and the source tank in Figure 4.4.



Figure 4.2 – Ambient tank photograph



Figure 4.3 – Compartment photograph



Figure 4.4 - Source tank photograph

The magnetic flow meter was calibrated with fresh water to ensure the flow rate given on the display was representative of the actual flow rate. All ball valves were opened and the precision valve was then turned up until a steady flow was seen exiting out the source, at which point it was turned down to the desired flow rate and measurements taken. The water was captured in a bucket for approximately one minute before being weighed and the mass (± 0.004 g) and time (± 0.1 s) recorded. The flow rates investigated ranged from 1 L/min to approximately 3.2 L/min. Figure 4.5 shows the calibration curve for the magnetic flow meter.

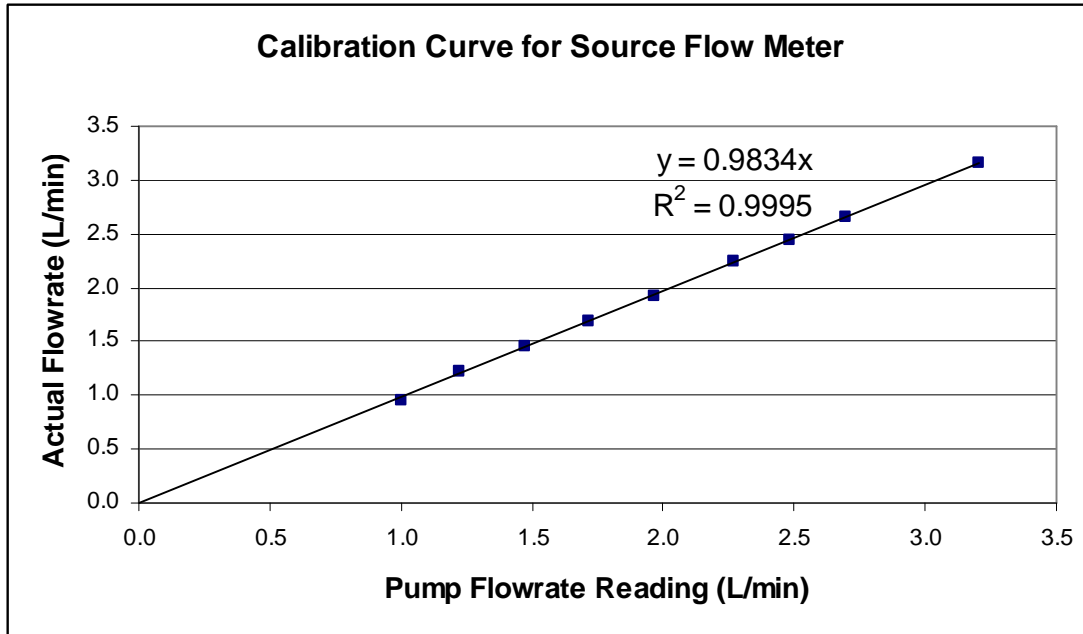


Figure 4.5 – Magnetic flow meter calibration curve

The light source for the attenuation experiments was a bank consisting of eight 100 Hz fluorescent tubes. The light bank was held in place by a steel frame and located directly behind the back window of the tank. A translucent plastic diffusion sheet of approximately 2 mm in thickness was placed between the light bank and the tank in order to create a more uniform light source. On the sides of the light bank where it protruded beyond the width of the tank, black cloth drop sheets were used to prevent any light entering the tank from any direction other than through the rear window.

4.3. Camera

The position and set up of the camera is crucial to the conduction of these experiments as it is upon the camera and the light that it receives that all results are based. The camera in question, while it is of high quality, is of a style used for home videoing. As a result of this it adjusts many of its parameters automatically which can lead to unexpected changes in the intensity of light received. This section describes how the camera was positioned and set up in order to achieve consistent, repeatable results for the experiments.

Camera Setup

Facing the tank, a digital video camera was positioned approximately 5 m from the front of the tank. While this may seem to be quite a large distance it is important to avoid issues of parallax. Parallax occurs due to the difference in the distance travelled between a ray of light which passes from the centre of the light bank through the tank to the camera and one that travels from the corners of the bank through the tank to the camera. This is highlighted below in Figure 4.6.

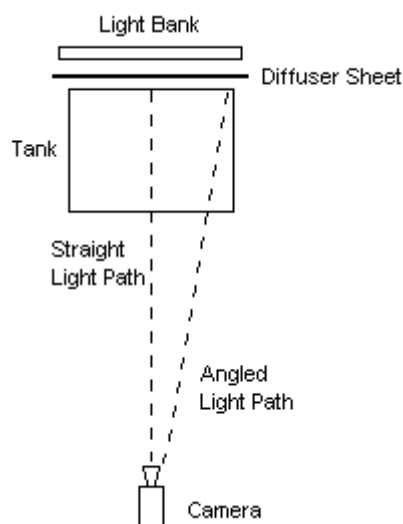


Figure 4.6 – Plan view of setup showing parallax

As light from the corners has to travel further to the camera than light that travels straight, it will be attenuated slightly more by having to travel through more of each

medium on the way. By using the approximation that the camera is infinitely distant from the tank and the distance paths are the same an error is being introduced into the calculations. The magnitude of this error can be found by considering the maximum length that the light could travel compared to the straight line distance. The maximum horizontal and vertical distance from the image centre is approximately 500 mm in each case. Therefore the distance to the corner is approximately 700 mm. This means the maximum distance from the corner to the camera is 5040 mm. Compared to the straight line distance of 5000 mm this corresponds to an error of 1 % which is deemed to be negligible.

The camera that was used was the Canon Digital Video Camcorder XM2 and was positioned on a tripod such that the camera was in the centre of, and perpendicular to, the front window of the tank. The camera has a resolution of 576 x 720 pixels. A computer was used for the data acquisition and this was connected to the camera via a data cable and an IEEE Firewire cable. A depiction of the camera and ambient tank set up is presented in Figure 4.7.

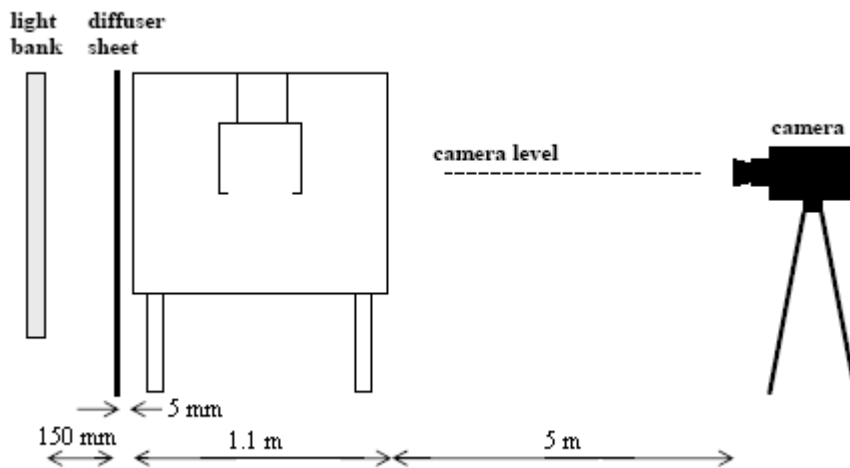


Figure 4.7 – Schematic drawing of camera setup

Camera Setup Experiments

As previously mentioned the position and setup of the camera was very important in these experiments in order to get repeatable runs that can be compared and allow us to infer information about the structure of the flow being studied. The Canon Digital Video Camcorder XM2 is a handycam and is designed for the home user. For this reason it adjusts many of its parameters automatically so that the inexperienced user is easily able to obtain reasonable quality images. In this application however this affects the experiments in a negative way. This issue can be resolved however by manually adjusting the parameters of the camera and ensuring it does not make any unexpected automatic changes.

During an experiment it is vital that the only change in light intensity is due to the increase in dye concentration in the tank. The white balance was set manually by zooming the camera in until the shot consisted of only white background, i.e. none of the structure of the tank could be seen, only the lights shining through from behind, and the 'set white' button pressed. By doing this the camera adjusts the relative magnitudes of the green, red and blue guns at each pixel and sets them so that they are the same. This is preferable to the camera setting the white balance because when red dye is added to the solution the camera would then adjust the gain of the other two guns itself.

A series of tests were conducted in which the shutter speed, exposure and gain were adjusted. The main priorities in setting these parameters were to ensure that the maximum intensity signal was set as close as possible to, but not over 255, and that the experiments were repeatable. If the intensity at any point was greater than 255 then the image would be over exposed and the colour saturated. This is undesirable because there is no way of telling how saturated the colour is and hence how large a change in intensity actually is. It is important however that the maximum intensity be as close as possible to 255 (typically 230 – 240) because this allows as big a dynamic range as possible, thus making the measurements more accurate. The camera focus was also set manually.

The fluorescent lights that were used work by alternately heating the neon in the tubes up until they glow every 0.01 seconds and then switching off. It has been suggested (Kikkert 2006) that if the shutter speed is faster or of similar frequency to that of the bulb then these fluctuations may show up as intensity variations with time. In order to investigate this issue the light intensity of a particular pixel was monitored over time with shutter speeds of 1/100, 1/210. These speeds represent 100 and 210 percent of the frequency of the bulb. The profiles at each shutter speed are represented in Figure 4.8.

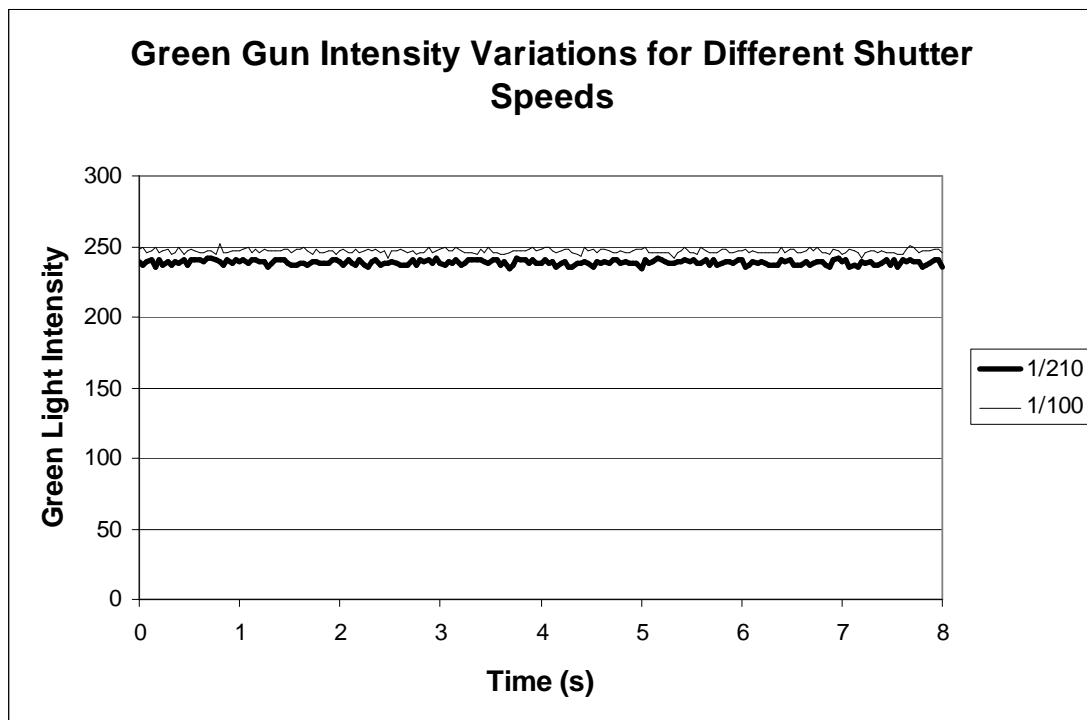


Figure 4.8 – Green gun light intensity at various shutter speeds

The above figure shows that even if the shutter speed is more than twice as fast as the frequency of the bulb there is no significant increase in the fluctuation of the green light intensity.

The following table outlines the combinations of the camera set up that were investigated according to the requirements discussed above. The set up that was used was number 11 in the table with the shutter speed set to 1/100, the exposure to 8 and the gain to 0.

Camera set up	Shutter Speed	Exposure	Gain	Recorded
1	1/60	5.7	6	~ 100 frames
2	1/60	6.2	0	~ 100 frames
3	1/60	6.7	0	~ 100 frames
4	1/60	8	0	~ 100 frames
5	1/75	6.7	0	~ 100 frames
6	1/75	7.3	0	~ 100 frames
7	1/75	7.3	0	~ 100 frames
8	1/75	7.3	0	~ 100 frames
9	1/75	8	0	~ 100 frames
10	1/75	8	0	~ 100 frames
11	1/100	8	0	~ 100 frames

Table 4.1 – Camera set up experiments

4.4. Calibration Experiments

In order to determine the relationship between the increase in dye concentration and loss in light intensity due to attenuation, a series of calibration experiments were carried out. These experiments were designed to work out the maximum dye concentration for which the linear relationship with light attenuation applies and to explore possible limitations in the technique.

The setup used is shown in Figure 4.7. Instead of the fire compartment however, a calibration cell of approximately 9 L capacity was placed inside the tank in the position where the outlet of the compartment would otherwise be. The calibration cell was square in shape and measured 119 mm in depth in the direction of the light path.

A reference image of the tank filled with water but not containing the calibration cell was recorded using Adobe Premier 6.0. The cell was filled with 7.75 L of water and a video of approximately 100 frames was taken using Premier. A dye solution of 0.0335 g was mixed thoroughly into 250 ml of water. The solution was added 25 ml at a time with a pipette, mixed well and a video of approximately 100 frames was taken.

Once the video footage was converted to .tiff files, an image sequence was created in Imagestream 6.0 (Nokes 2005) in order to analyse the data. The data was first time averaged using Imagestream in order to smooth out any fluctuations in the signal. Then, using the white reference image initially taken, the calibration cell images were filtered so that only the intensity of the green gun was shown. A small region of the image inside the calibration cell was used to create an intensity field in Imagestream and this data was exported as a .csv (comma separated variable) file for reading in Microsoft Excel. The green light intensity was averaged over the small region inside the cell and this value was plotted against the integrated dye concentration in the cell to produce Figure 4.9.

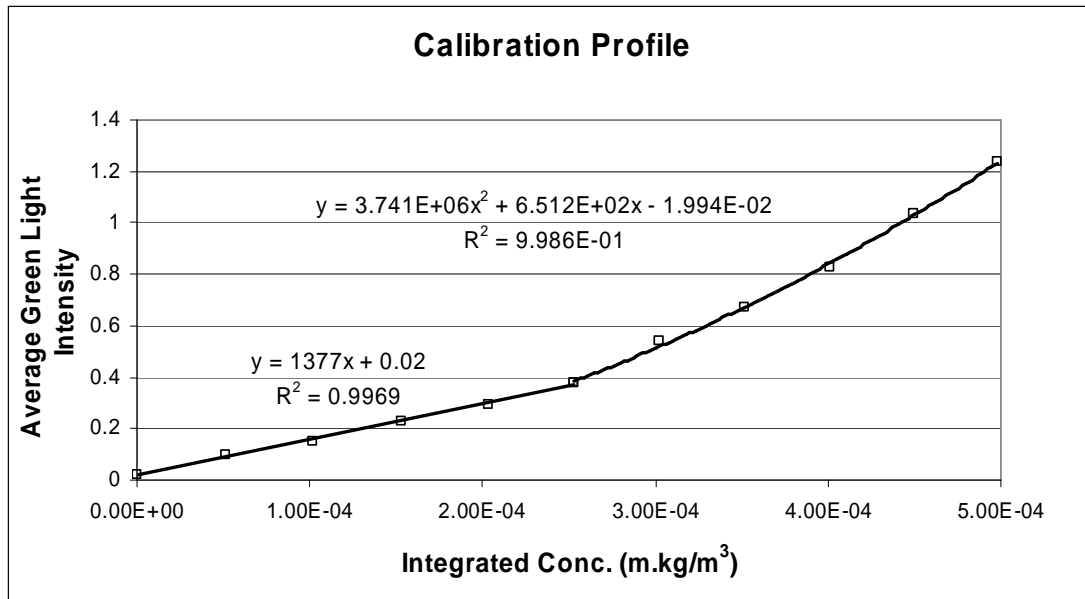


Figure 4.9 – Calibration profile of red dye response

The above figure shows a distinct linear region at low dye concentrations before the relationship becomes exponential at higher concentrations. The maximum integrated concentration for which the linear relationship applies is seen to be approximately $2.5 \times 10^{-4} \text{ m.kg/m}^3$. Above this point a quadratic expression is used to represent the data. By rearranging the equations in the above figure green light intensity data can easily be converted to integrated concentration data.

The following table describes the incremental dye additions used in the calibration experiments and the intensity of green light that was recorded.

Increment	Dye added (g)	Water volume (L)	Concentration (m.kg/m ³)	Green Light Intensity
0	0	7.750	0.00	0.02
1	0.00335	7.775	5.127E-05	0.1
2	0.00670	7.800	1.022E-04	0.15
3	0.01005	7.825	1.528E-04	0.23
4	0.01340	7.850	2.031E-04	0.295
5	0.01675	7.875	2.531E-04	0.375
6	0.02010	7.900	3.028E-04	0.54
7	0.02345	7.925	3.521E-04	0.67
8	0.02680	7.950	4.012E-04	0.83
9	0.03015	7.975	4.499E-04	1.035
10	0.03350	8.000	4.983E-04	1.235

Table 4.2 – Calibration experiment conditions

4.5. Method Performance Check

In order to check that the green light attenuation to integrated dye concentration relationship is working well a simple test was devised to provide confidence that design of the experimental system was progressing according to plan. This section outlines this test and explains why it was used.

The ambient tank was filled with water and a white background video was taken. Then 0.1244 g of dye was added to the tank as a liquid and mixed thoroughly. This gave an integrated dye concentration in the tank of $2.11 \times 10^{-4} \text{ m.kg/m}^3$, which is at the limit of the linear region. A background red video of the tank was recorded. Once these images were recorded the compartment was placed in position inside the tank so that it filled up with the dye solution and then checked to ensure it was fully water tight. The ambient tank was then emptied and refilled with fresh water leaving the compartment filled with dye solution immersed in fresh water. The background red image and the dye filled compartment are shown in Figure 4.10.

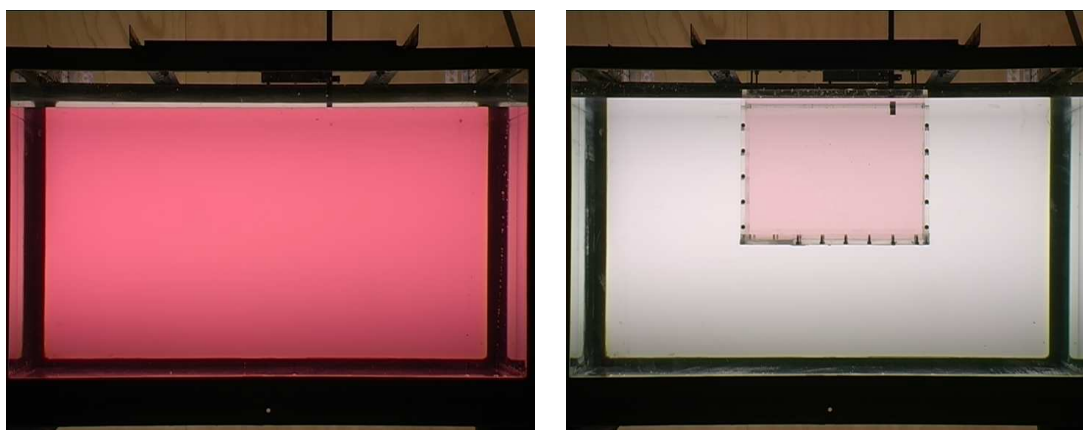


Figure 4.10 – Background red image and dye filled compartment used in performance test

If the relationship between the integrated dye concentration and the amount of green light attenuated is valid, then the integrated concentrations recorded should be approximately equal to the ratio of the depth of the compartment to the depth of the ambient tank as the amount of other light attenuated should be consistent in each case. The depth of the ambient tank is 1068 mm and that of the compartment is 250 mm

giving a ratio of 4.3. Imagestream was used to filter the images and take the average concentration from a small area inside the position of the compartment and it was found that the ratio of the concentrations from the two images was 4.5. While this is slightly different from the actual ratio of the depths concerned, one must remember that the light path has been slightly altered through the inclusion of the plastic compartment walls. Furthermore the amount of light attenuated by dye within the compartment will be slightly different than that attenuated by dye in front or behind the compartment, as is found in the background dye solution. This test is not a robust analysis of the technique due the differences in the light path described above but gave confidence that the equipment was working well and that there were no major issues.

4.6. Experimental Configuration

Prior to the conduction of any quantitative experimental work in this project, it was important to investigate the source conditions required to generate an appropriate fire analogue with the saltwater system. There are a huge number of variations of initial conditions which could be employed including different source diameters, inlet velocities, source positions and room sizes/configurations. The scope of this project, however, could not possibly encompass all of the potential fire scenarios so it is necessary to investigate a relatively small number of the most relevant, beneficial situations.

Initial Conditions

The compartment used for this investigation was a 1:9.6 scale model of a (length x depth x height) 3.6 m x 2.4 m x 2.4 m room, which is are standard ISO room dimensions. This gives the compartment dimensions of 0.375 m x 0.25 m x 0.25 m. The size of the room was chosen to be as large as possible while still fitting inside the ambient tank with enough room such that the walls of the enclosure did not affect the flow of fluid from the opening in the compartment.

Keeping in mind the scope of this project, which is to investigate the fluid flows from the compartment opening, only one fire position was investigated. The source was situated towards one end of the room, with the opening at the other end. It was important that the source was far enough away from the walls of the compartment so as to minimise the effect of the walls and ensure the plume behaved as close as possible to a free plume. This allowed entrainment from all sides of the plume, which was the most conservative scenario as it resulted in the most mixing and hence the most smoke.

The source was located away from the opening to ensure there is sufficient time for a ceiling jet to fully develop in the room. If this was not the case and the momentum from the fire itself were able to impinge on the opening then we would be leaving the

bounds of what zone models are able to predict and thus steering away from the scope of the project.

The size of fire that can be investigated is limited by a maximum density difference between fluids for which the concentration density relationship is valid which is approximately 10 % (Shin *et al.* 2004). For this reason two relatively small fire sizes were investigated. The size of fire corresponding to a particular saltwater density difference is derived in the next section.

Once the location of the source and the arrangement of the compartment had been determined the source conditions – namely the source diameter and the inlet flow rate – needed to be determined. This is a very important step in ensuring comparable conditions between the real fire scenario and the saltwater analogue.

For this analysis it was fair to assume that the fire does not contribute any mass to the system, instead the buoyancy forces are caused through the heating of fluid and hence generation of a density difference. When saltwater is used the buoyancy forces are again due to a density difference between the fluids, however this time it is as a result of an introduced fluid. This was important when it came time to analyse the flows through the opening as this extra fluid needs to be taken into account.

At the source of a fire there is no inherent momentum in the fluid. This is not the case in saltwater modelling and it is an important point of difference. The flows into the compartment must be kept as low as possible so that this difference is minimised. However, in order to generate a turbulent plume a reasonable velocity is needed to ensure a large enough Reynolds number for that to happen. In reality the flow rate will be based on a compromise between these two issues.

Important in the analysis of these internal flows is the entrainment of the introduced fluid. As a result of those issues presented above and the required compromise between the Reynolds number required and the need to minimise initial velocity, there will be a jet region (which is not present in the real fire scenario and therefore is designed to be as small as possible) and a plume region. The entrainment into the plume is much greater than that into the jet region. For this reason it is very important

to be able to calculate where the transition between these two flow regimes is. The distance from the source to the point where the plume is established is known as the jet to plume transition length, l_{jp} . In the jet region it is the momentum flux which dominates the buoyancy flux and vice versa in the plume region. When these forces are approximately equal is where we find the jet to plume transition.

The next issue is to determine the source conditions that are required to get the flow pattern that is desired. An investigation of a range of source conditions and their effect on the Reynolds and Froude numbers is presented below in Table 4.3.

Pipe diameter	d	m	0.005	0.005	0.01	0.01	0.01	0.002
Flow rate in pipe	Q_0	L/min	1	0.5	0.78	1.5	1.5	1
Initial velocity	U_0	m/s	0.85	0.42	0.17	0.32	0.32	5.31
Initial fluid density	ρ_0	kg/m ³	1030	1030	1030	1030	1100	1030
Initial density difference	Δ_0	m/s ²	0.294	0.294	0.294	0.294	0.98	0.294
			(3%)	(3%)	(3%)	(3%)	(10%)	(3%)
Initial buoyancy	B_0	m ⁴ /s ³	4.9E-06	2.5E-06	3.8E-06	7.4E-06	2.5E-05	4.9E-06
Initial momentum	M_0	m ⁴ /s ²	1.4E-05	3.5E-06	2.2E-06	8.0E-06	8.0E-06	8.8E-05
Jet to plume transition	l_{jp}	m	0.104	0.052	0.029	0.055	0.03	0.412
Reynolds number	Re	-	4227	2114	1649	3170	3170	10568
Froude number	Fr	-	22.14	11.07	3.05	5.87	3.22	218.78

Table 4.3 - Pipe flow initial conditions

The initial density difference is as described using equation 3-1.

$$\Delta_0 = \left[\frac{\rho_s - \rho_a}{\rho_s} \right] g \quad (3-1)$$

The initial buoyancy flux and momentum flux are calculated using equations 4-5 and 4-6 respectively.

$$B_0 = U \cdot \Delta_0 \cdot A \quad (4-5)$$

$$M_0 = \frac{\pi}{4} U_0^2 d^2 \quad (4-6)$$

Recall the Froude number as given in equation 2-16, and the Reynolds number given in equation 2-17.

$$Fr_0 = \frac{U_0}{\sqrt{\Delta_0 d}} \quad (2-17)$$

$$Re = \frac{U_0 d}{\nu} \quad (2-18)$$

The above table shows that if a 5 mm source diameter were to be used then the jet to plume transition length is very large and far from ideal when considering the physical dimensions of the compartment. If the flow rate is reduced to 0.5 m³/s the transition point does fall to a more acceptable level but the Reynolds number is no longer high enough to ensure a turbulent flow regime. If a 10 mm source is used and the initial velocity increased the transition length is halved and a high Reynolds number can be obtained while still preserving a low Froude number. If however a 20 mm opening is used high Reynolds numbers can be obtained easily with low flow rates but the jet to plume transition length is extremely large and outside the bounds of the compartment.

As shown in this table the best compromise between the opposing ideals of higher Reynolds number and low jet to plume transition length is found with a 10 mm source at approximately 1.5 L/min inlet flow. In practice a 10.3 mm source diameter was used at approximately 1.7 L/min to ensure turbulence is reached. We also see that when the fluid density is increased to 1100 kg/m³ with the 10 mm opening the parameters obtained are still within a suitable range.

4.7. Equivalent Fire Size

While the conduction of these experiments will provide insight into the nature of the plume and of the compartment filling problem, without the ability to relate the work to an actual fire size in the room, its applicability is very limited. When conducting a fire engineering design the engineer will come up with a design fire which is the realistic worst case scenario for a building or room. The engineer can then use their design fire input to be able to predict flows within the compartment and through a ceiling opening. This section describes the way the fire size is calculated from the density difference used in the saltwater modelling.

In order to relate the density difference in the saltwater analogue system to a fire size in a real scenario, the buoyancy fluxes at the source of each scenario are matched. This is done through adaptation of the method used by Poreh *et al.* (1998) in their spill plume analysis. Recall that the initial flux of buoyant fluid can be described by equation 4-5.

$$B_0 = U \cdot \Delta_0 \cdot A \quad (4-5)$$

Consider the convective heat flux of the fire given in equation 4-7.

$$\dot{Q} = c_p \int \overline{\rho \cdot w \cdot \Delta T} \cdot dA \quad (4-7)$$

An alternative description of the buoyancy flux in equation 4-5 is given in equation 4-8.

$$B = \left(\frac{g}{\rho_a} \right) \int \overline{w \cdot \Delta \rho} \cdot dA \quad (4-8)$$

Using the pressure of water at sea level and an average ambient tank temperature of 14 °C, $\rho \Delta T = (999.22 \times 287)$ and $\Delta T/T = 287000 \Delta \rho/\rho_a$. Using this information and

combining equations 4-7 and 4-8 above, an expression can be obtained for the buoyancy flux in terms of the convective heat flux.

$$B = \left[\frac{g}{287000c_p} \right] \dot{Q} = \frac{\dot{Q}}{122338} \quad (4-9)$$

Expressions 4-5 and 4-9 can now simply be equated to determine the equivalent unscaled heat release rate from a saltwater density. In order to scale the result to the real scenario one simply employs the equivalent scaling law relating convective heat release rate to length (Harrison 2000) which is given in equation 4-10 below.

$$\dot{Q} \propto L^{5/2} \quad (4-10)$$

Since in this case a 1:9.6 scale is used, the multiplying factor for convective heat flux is 316. Using the above method we determine that the real fire size using a three percent density difference is 323 kW, and for a six percent density difference is a 646 kW fire.

4.8. Experimental Method

Here, as in all scientific research, repeatability and quality assurance are paramount. Therefore a strict and complete method of operations needs to be devised in order to minimise the effects of any human or systematic error. The conduction of each experiment needs to be identical with only the parameter of interest being varied so that any subsequent change in output can be considered causative. In this section the method for the saltwater modelling experiments is presented and experiential issues discussed.

Firstly the source solution is made up in the source tank. The tank is filled with water up to 60 L. The appropriate amount of salt is then added to the water depending on the density required. The scales for weighing the salt are accurate to 0.0005 g.

The amount of dye required to achieve an integrated concentration of $1.4 \times 10^{-4} \text{ m.kg/m}^3$ (scaled by the source diameter) was weighed on precise scales (accurate to 0.00005 g). In 60 L the amount of dye required was 0.8155 g. As the amount of dye is small, one lump of powder that does not dissolve could significantly affect the concentration in the solution. For this reason a portion of the dye was first added in a small amount of water until completely dissolved before being added to the solution. This was repeated until all the dye was dissolved into the solution. This ensured that there were no lumps of undissolved dye remaining at the bottom of the tank and that the appropriate concentration was achieved.

Once the solution was made up and stirred thoroughly the pump was left circulating the solution up to the constant head tank and back into the source tank to ensure there was thorough mixing of all components. The solution was then sampled and analysed in the density meter to determine that it had the correct density for the problem at hand.

Before commencing a series of experiments the tank and the compartment were both levelled and then cleaned using specialised glass or plastic cleaning solutions respectively. The valves were opened to allow the solution to exit the jet and the fine

control valve adjusted to the desired flow rate before the ball valve was shut off. Doing this allows the desired flow rate to be obtained almost immediately upon the commencement of an experiment through the operation of the ball valve.

The ambient tank was filled with fresh water and left overnight for the temperature to equilibrate and for the water to de-aerate. At this time all bubbles are removed from all the surfaces on the ambient tank as well as on the compartment. The fluorescent light bank was switched on at least an hour before the experiment so that the air surrounding it has reached an equilibrium temperature that did not vary. Before the tank was finally filled right to the jet opening, the jet was turned on for a few seconds and collected in a bucket. This was done so that any air bubbles which may have collected in the jet line were removed before the experiment began. The tank was then filled to the level of the source opening (the ‘floor’ of the compartment) and the fluid left to settle for a few minutes before commencing an experimental run. The room must be in complete darkness except for the light bank, and light entering the tank other than through the rear window was minimised or eliminated.

Prior to a series of experiments the ambient tank was filled with water (the compartment being present) and then dye added to the concentration at the maximum of the linear range for which the light attenuation to integrated concentration relationship is valid, i.e. $2.5 \times 10^{-4} \text{ m.kg/m}^3$. The depth of the tank was 1.068 m so the amount of dye required for the 578 L tank was 0.1353 g. A small video clip was recorded and this reference image was used as the upper bound when applying a polynomial field calibration to the image during processing. This is the filter which applies the linear attenuation relationship to determine the concentration at a pixel between zero (recorded before an experiment of the ambient tank filled with water only – no dye) and the maximum red background.

The camera was set up and recording initiated. An initial set of approximately 100 images was recorded before the flow was started. This was done to obtain a reference blank image that was relevant to a particular experiment and used as such when the images were processed. Recording was then started and the ball valve opened to allow the solution to escape out the jet and then shut off once the experiment has been run for approximately 5000 frames (3 minutes 20 seconds).

The following table outlines each of the experimental series conducted including the source conditions and the opening used in each case (except for the free plume comparison experiments which obviously do not include the compartment).

Source conditions		Opening	Flow rate (L/min)	Recorded
Solution volume	60 L	50 square	1.750	> 5000 frames
Salt density	3%	75 square	1.773	> 5000 frames
Dye concentration	0.01067 g/L	100 square	1.727	> 5000 frames
		50 slot	1.730	> 5000 frames
		100 slot	1.732	> 5000 frames

Source conditions		Opening	Flow rate (L/min)	Recorded
Solution volume	60 L	Free plume	1.751	> 5000 frames
Salt density	3%			
Dye concentration	0.01066 g/L			

Source conditions		Opening	Flow rate (L/min)	Recorded
Solution volume	45 L	50 square	1.751	> 5000 frames
Salt density	3%	75 square	1.715	> 5000 frames
Dye concentration	0.002134 g/L	100 square	1.721	> 5000 frames
		50 slot	1.641	> 5000 frames

Source conditions		Opening	Flow rate (L/min)	Recorded
Solution volume	60 L	50 square	1.750	> 5000 frames
Salt density	6%	75 square	1.741	> 5000 frames
Dye concentration	0.00449 g/L	100 square	1.745	> 5000 frames
		50 slot	1.750	> 5000 frames

Table 4.4 – Experiments conducted

4.9. Data Analysis Methods

Raw video of the experiments needed to be converted into a viable format for further analysis and this was done by first exporting the video .avi files into a series of single frame .tiff files. At this point Imagestream was employed to reduce the data to a usable format depending on its purpose as described below. In each case however this involved first filtering the data to use the intensity recorded from the green gun only. Then the polynomial field calibration is used to apply the relationship between light attenuation and dye concentration. The polynomial field calibration tells the image processor that the relationship between light intensity and dye concentration is linear from zero up to the maximum determined in a series of calibration experiments and non-linear thereafter. The intensities at zero and maximum concentration are determined prior to an experiment by recording a series of frames with no dye present and with the linearly maximum concentration present respectively and using these to bound the polynomial field calibration.

Layer Height

The layer height for each opening was determined by using Imagestream to detect the interface between the two zones inside the compartment. This was done for a particular frame by setting the criterion for the boundary of the layer and using the edge detection package within Imagestream to track up the image and read off the height at which this criterion is reached. For the experiments $t = 0$ was determined consistently as being the time at which the ceiling jet that travels across the ceiling from above the plume reached the far end of the room. This is why there is already a layer height present when the experiments starts, but was a way or ensuring uniformity in the recording of the experiments.

An example of a raw frame for the experimental recording is shown in Figure 4.11. The same frame showing the compartment when the image has been processed is shown in Figure 4.12. In each case the layer interface height can be seen to be quite clearly defined and is highlighted by the arrows. These images are from the six percent experiments using the 50 mm square opening.

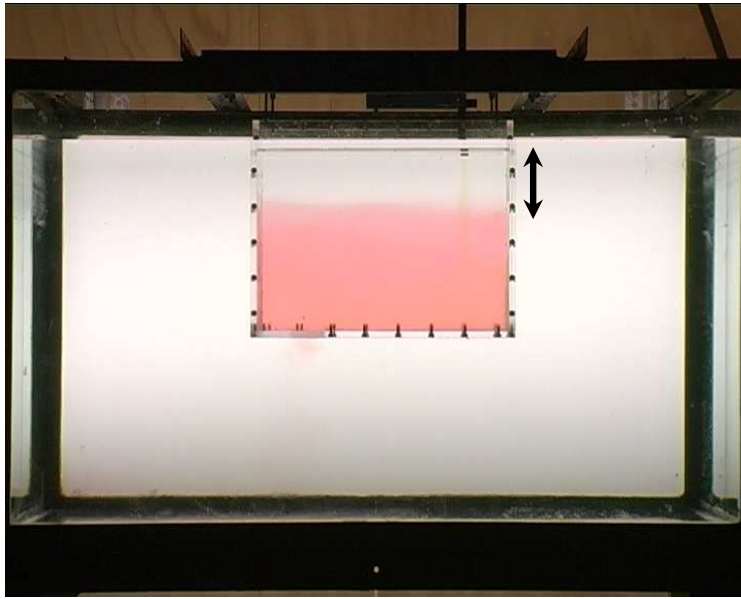


Figure 4.11 – Experimental image showing the upper and lower layer

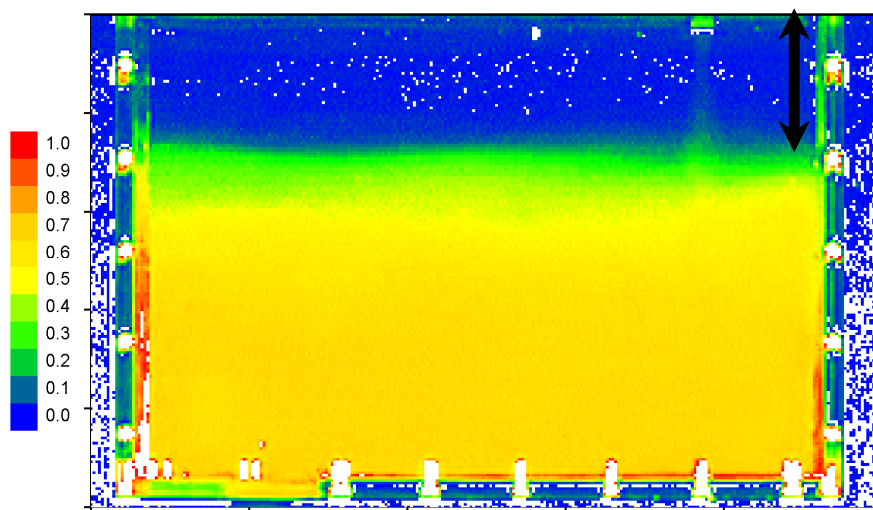


Figure 4.12 – Processed image of the compartment

The edge criterion was set to approximately half the maximum in the layer in each case and this was averaged across the width of the compartment to obtain a single layer height for each opening at each time step. As can be seen from the above image that used the 50 mm square opening, the spatial variation of the layer across the compartment is very small so the approximation of averaging the data across the compartment is accurate. However as the opening size is increased the variation

across the compartment becomes greater. This phenomenon is discussed in more detail in the following chapter.

The layer height data recorded is best presented in dimensionless form according to equation 3-6 below:

$$\frac{z_l}{H} = \frac{1}{\left[1 + \left[\frac{3^4}{2^3} \pi \frac{H}{D} \frac{H}{L} \left(\frac{\beta}{\gamma} \right)^2 Fr_0 k_T^4 \right]^{1/3} t^* \right]^{3/2}} \quad (3-6)$$

In a practical sense this means plotting z_l/H on the y axis vs the terms multiplying t^* on the x axis, all other terms being constants. Therefore:

$$x^* = \left[\frac{H}{D} \frac{H}{L} \left(\frac{A_o}{A_B} \right)^2 Fr_0 \right]^{1/3} t^*$$

$$y^* = \frac{z_l}{H} = \frac{1}{\left[1 + \left(\frac{3^4}{2^3} \pi k_T^4 \right)^{1/3} x^* \right]^{3/2}}$$

Plume Analysis

Detailed analysis of the experimental plumes was done by considering concentration profiles of a single pixel in width taken along the centreline of the plume and across its width. Plumes were time averaged where appropriate as detailed in subsequent sections. A schematic of the profiles taken is shown in Figure 4.13.

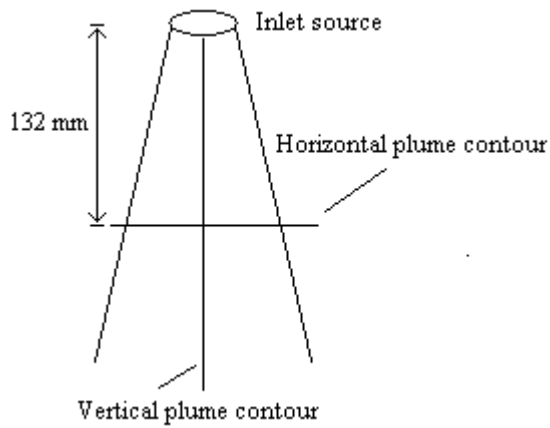


Figure 4.13 – Plume contour schematic

This was expanded further by using a specific Matlab algorithm to study the plume. A region from the top of the compartment to the bottom and encompassing the width of the plume was considered for the analysis. An example is shown in Figure 4.14 below.

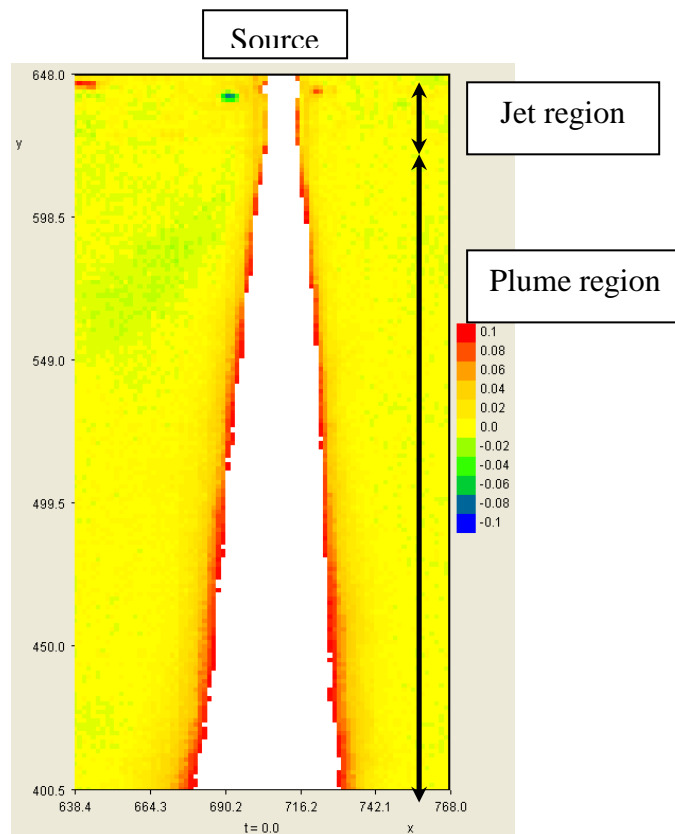


Figure 4.14 – Imagestream view of a time averaged plume

The image is then analysed in Matlab according to the code shown in Appendix A which is used to track the trajectory of the plume as well as the spread and maximum

centreline concentration The algorithm was provided by Cameron Oliver, University of Canterbury, 2007. The function works by employing the following steps:

Step 1

Determining the ridge of maximum values via direct interpolation

When the 'scalartaverse' function is called a large number of variables are incorporated including the source position and the source angle. The algorithm uses the Matlab function 'fminbnd' to find the angle at which the input array (concentration) at a distance of '*stepLength*' away from the source position is at a maximum. The condition is that the angle must be between the bounds of ± 10 degrees. So the algorithm 'looks' a small distance away from the source and finds the centreline (or maximum or ridge) of the concentration and limits the result to within 10 degrees of the starting point.

The algorithm then repeats the process tracking down the array at distances of *stepLength* and calculating the angle at ± 10 degrees from the step previously determined. Through this process a rough trajectory of the plume is able to be determined.

Step 2

Taking Gaussian fits and using them to refine ridge definition

The algorithm steps through each point in the trajectory previously determined and takes cross sections perpendicular to the angle of the trajectory at that point. This means it takes the value of the array at a set number of points across the cross section of the line. Everything below a certain percentage of the absolute maximum value of the cross section is discarded as not useful for the Gaussian fit.

The natural log of the remaining cross section values is fed to the Matlab function polyfit which fits a second order polynomial to the data. The form of the polynomial is: $\ln(C) = ar^2 + br + c$, where C is the concentration value from the array and r is the radius (distance) from the trajectory point in question. The values of a, b and c are used to back-calculate the correct values for C_m , r_0 and b for the best-fit Gaussian

relationship: $C/C_m = \exp(-(r-r_0)/b^2)$. The trajectory centrepoint is then refined by using the r_0 value just calculated.

Step 3

Making 'n' further Gaussian-fitting iterations

Using the above process the trajectory is refined through 'n' further Gaussian fitting operations. As the trajectory is refined the angles at which each cross section is taken are refined and when the cross section is at a more accurate angle, more accurate trajectory positions are obtained.

Step 4

Extracting final set of data to return to user

Data is interpolated at a higher density (and/or greater width) than was used by the program for finding the Gaussian fits.

5. Results and Discussion

5.1. Introduction

This section describes the experimental observations and results obtained for each of the density differences (fire sizes) used and how the integral model compared to the experimental data. It also discusses how the integral model was employed to obtain exchange flow rates through the ceiling opening and the major issues encountered throughout the course of this study.

5.2. Experimental Observations

The source flow was initiated and recording begun as described in the previous chapter. The flow starts with an initial burst of fluid when the valve is opened and quickly travels towards the ceiling as a result of the buoyancy flux generated from the density difference but also due to the inherent momentum that is present at the source as discussed previously. The general structure of the plume is soon established with a small jet to plume transition length observed. The plume reaches the ceiling and immediately begins to spread outwards radially and also a short distance back down towards the floor as the introduced fluid is deflected from the ceiling. Figure 5.1 shows two video stills from the three percent density difference experiments using the 50 mm square opening highlighting this behavior with the plume formation 2 seconds after experiment start on the left and the plume striking the ceiling 6 seconds after experiment start on the right.

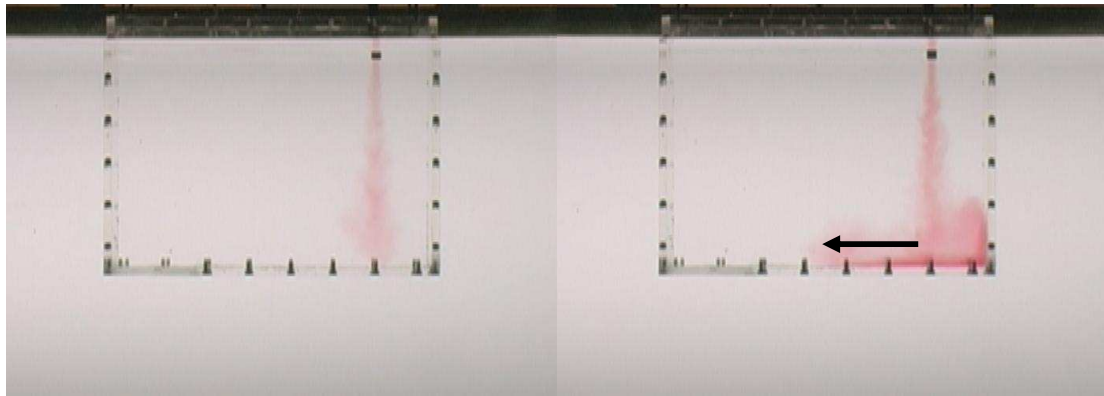


Figure 5.1 – Plume formation after 2 s (L) and plume reaching ceiling after 6 s (R)

The plume then travels further out from above the source in a radial pattern spreading across the ceiling in what is known as a ceiling jet (the direction of flow of the ceiling jet is shown in the above figure). The plume soon reaches the vent where it slowly begins to exchange with the ambient fluid outside the compartment. The initial exchange appears to be very low as the ceiling layer is only beginning to form and is still very dilute, i.e. the density difference is small. The ceiling jet then reaches the far end of the compartment where it is again deflected down towards the floor and back towards the plume because of the momentum as it reaches the wall, as shown by the arrow in the figure below. This flow continues back across the compartment and means the interface between the two zones is not well defined. Figure 5.2 shows the plume reaching the ceiling opening and the far wall of the compartment 15 seconds after experiment start and also the flow back below the ceiling layer 24 seconds after starting.

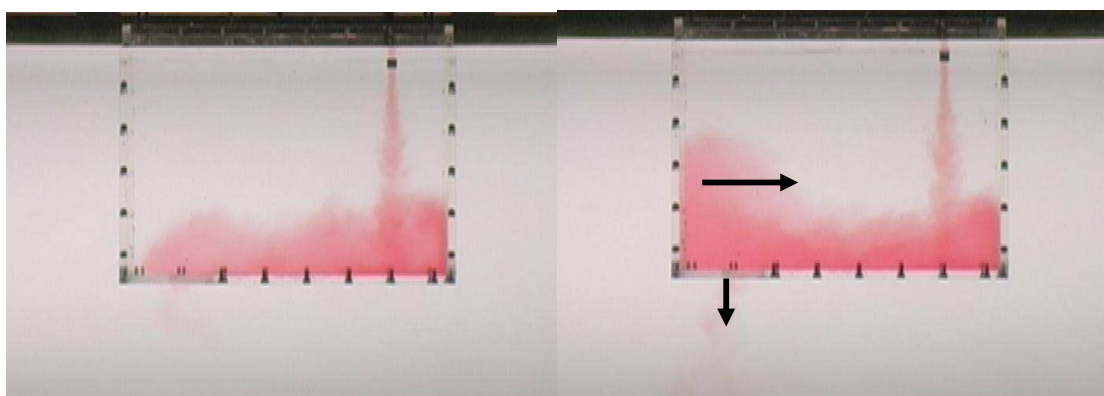


Figure 5.2 – Ceiling jet reaching wall after 15 s (L) and deflected off wall after 24 s (R)

As the experiment continues the interface between the upper and lower layer becomes more settled and the upper layer becomes more and more concentrated as the dense fluid builds up at the ceiling level. As the layer fills up and descends less and less ambient fluid is able to be entrained into the plume leading to a more dense layer also.

It was observed during the experiments that the way in which the exchange flow occurs is by the dense fluid leaving the compartment through the centre of the opening while the ambient fluid from the outside enters the compartment via the edges and the corner of the vent. This is interesting behaviour as it may indicate difficulties when comparing the work of those who have used circular vents with those that have used square vents in their experiments as the corners of the square vents in particular appear to play a big role in the flow structure. Figure 5.3 shows the layer interface becoming more settled and descending towards the floor of the compartment after 45 and 90 seconds.

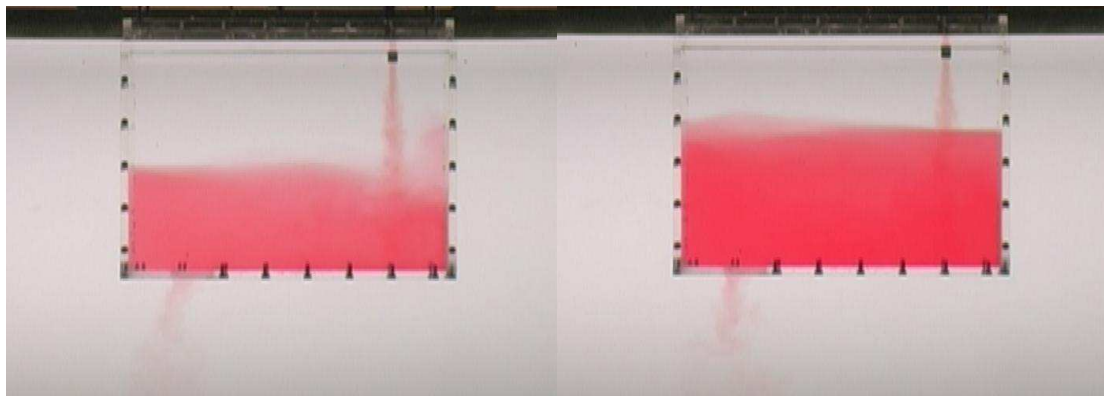


Figure 5.3 – Layer interface settling and descending after 45 s (L) and 90 s (R)

5.3. Layer Height

Layer height is presented as distance from the floor of the compartment. The layer height for the three percent density difference is presented in Figure 5.4 and for the six percent density difference in Figure 5.5.

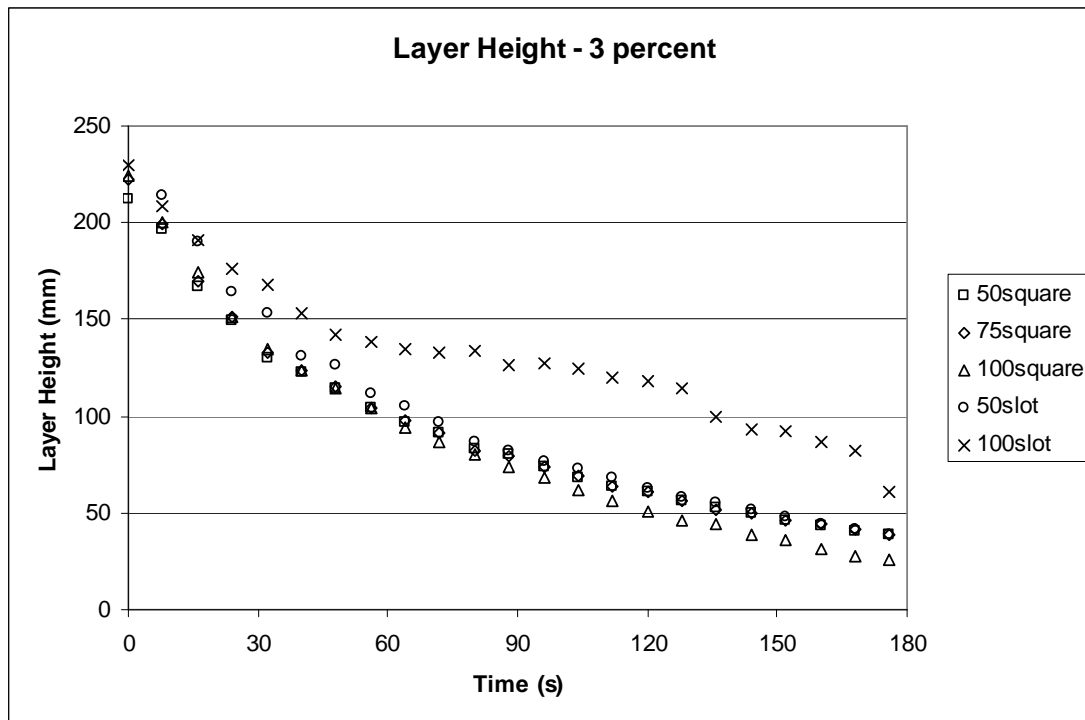


Figure 5.4 – Layer height for the 3 percent density difference

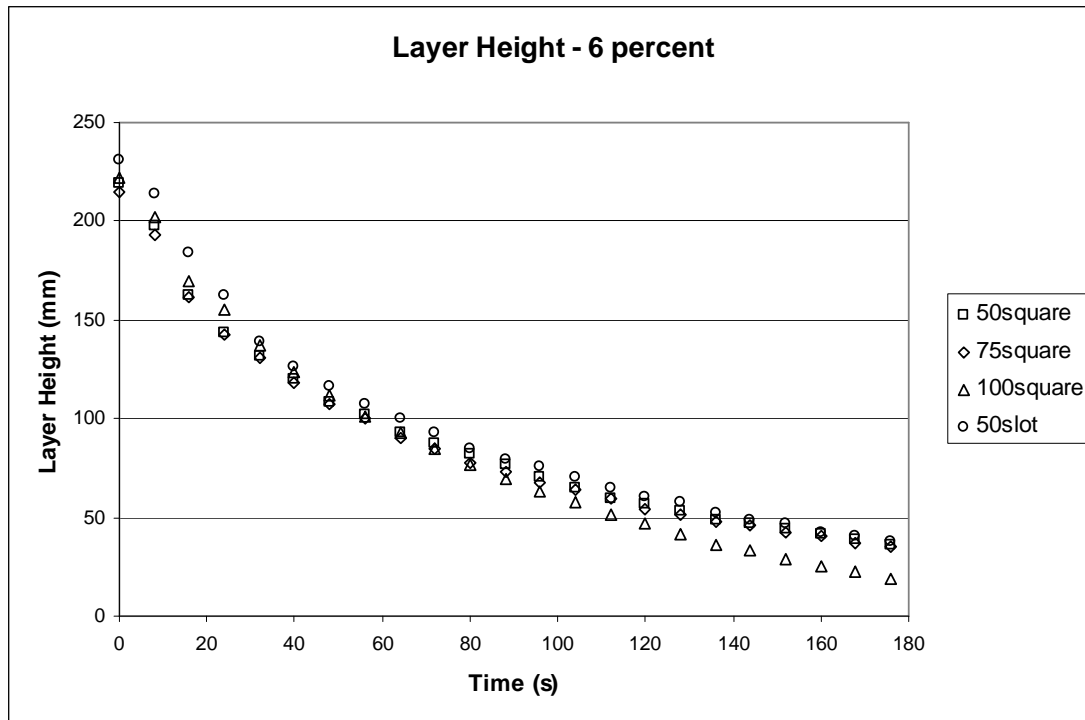


Figure 5.5 – Layer height for the 6 percent density difference

The layer height for each opening size and density difference follows the general trend toward the floor of the compartment as is expected. The size of the opening should not affect the rate of descent of the layer as the ambient air is exchanging only with the fluid that is in the upper layer. Since this is an exchange flow with a net mass loss of close to zero, for each density difference all curves should match. In Figure 5.4 however there is a notable difference. With the 100 mm slot opening we find the layer descends erratically and far faster than with any other opening.

During the experiments it was observed that when the 50 mm square opening was used the interface between layers was very well defined and it steadily descended towards the floor of the compartment in a consistent manner. As the opening size was increased the interface was found to be more disturbed and not as well behaved. In the case of the 100 mm slot the interface was so disturbed that the layer actually entrained additional fluid as it descended and this is what leads to its peculiar behaviour. A comparison is shown in Figure 5.6 with the well behaved layer of the 50 square opening on the left, vs. the turbulent nature of the 100 slot opening on the right. Both images were taken at the same relative time (53 seconds from experiment start). While this is an interesting result in itself, the behaviour when this opening was used

is erratic and makes it difficult to discern further meaningful data. For this reason the use of the 100 mm slot opening was discontinued at this point.

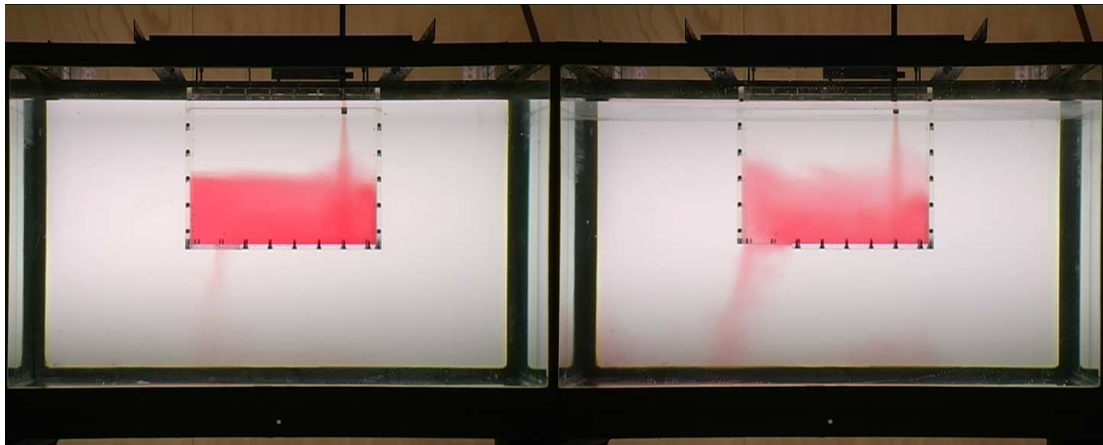


Figure 5.6 – Comparison of layer height definition for 50sq vs. 100sl

The layer height determined experimentally can now be compared with the integral model calculated earlier. This is shown below in Figure 5.7 using the data from the three percent density difference experiments.

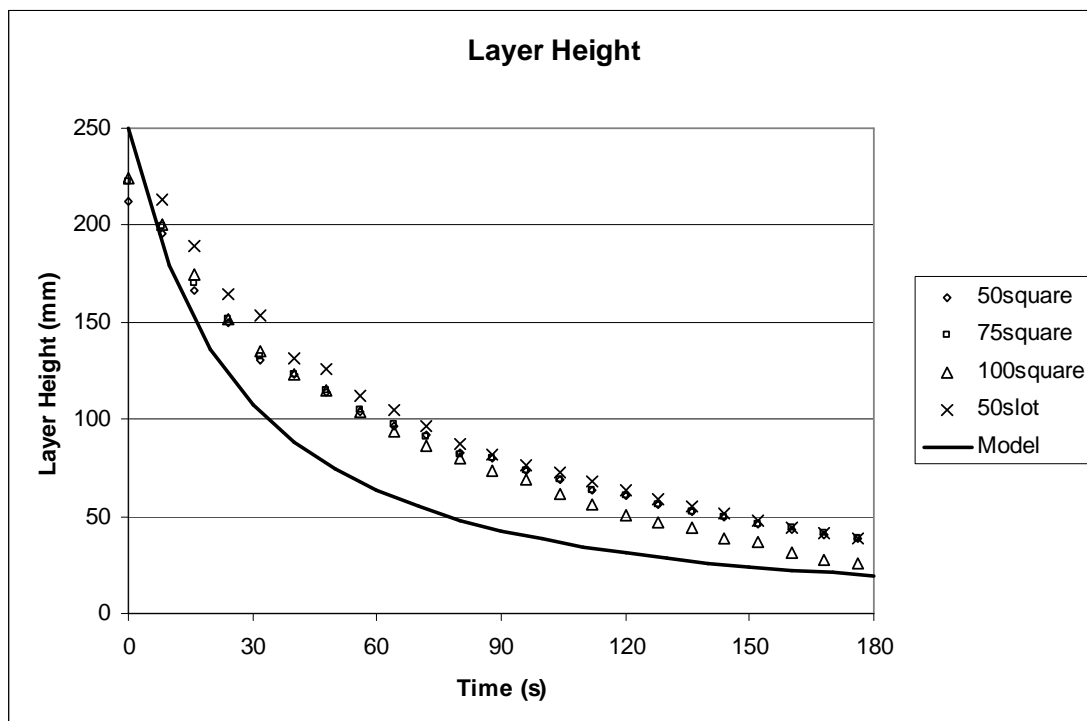


Figure 5.7 – Layer height in the compartment compared with that predicted in the integral model

As can be seen from the above figure, there is a significant discrepancy between the model and what is seen experimentally. This could be due to any of the inherent assumptions in the model discussed above and needs to be investigated further to improve on the model and give us a better understanding of what is really occurring in the compartment. The following sections analyse the structure of the plume in detail in order to highlight where the discrepancies between the predicted results and the experimental results lie.

5.4. Plume Analysis

There are a number of ways which can be used to describe the internal flow structure of the plume in the compartment and the flow through the ceiling vent opening. This section gives general details and trends regarding the concentration and structure of the flow leaving the vent and considers why the predicted and experimental results differ.

Free Plume Assumption

One of the preliminary assumptions made at the beginning of this investigation was that the plume was far enough away from the boundaries of the compartment that it had free entrainment from all sides and could be treated as if the compartment were not there. This is an essential assumption for the integral model.

In order to investigate this phenomenon comparisons are made between the plume structure within the compartment and a free plume that has no physical obstructions of any kind. This is done by considering vertical and horizontal contours of a free plume and a confined plume to find out if there were any inconsistencies between the two. The 50 mm square ceiling vent with a three percent density difference was used because this was experimentally the most consistent and well behaved scenario.

Horizontal Profiles

A profile of the free plume was taken horizontally across the plume 132 mm (13 port diameters) down from the inlet source. This is approximately halfway down where the compartment would be and is at the same level as the other horizontal profiles taken. The profiles were sampled at 5 second intervals and these are shown in Figure 5.8.

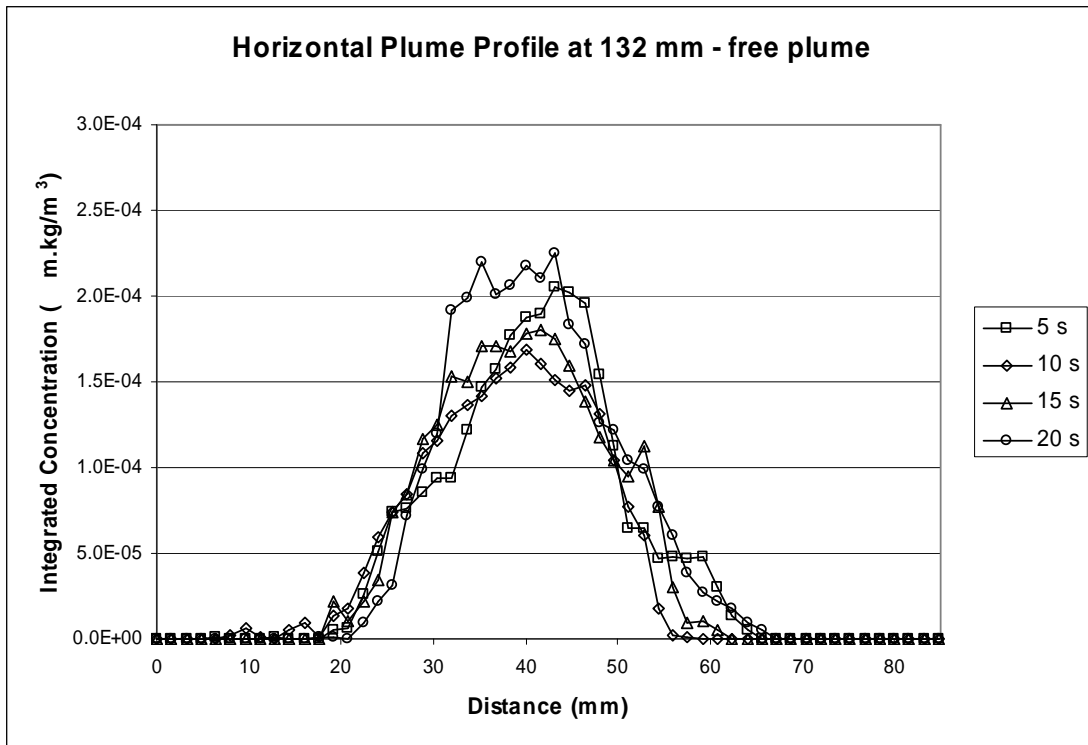


Figure 5.8 – Horizontal profile of the free plume

As can be seen from the above figure the plume profile has the expected shape, most concentrated at the centre and trailing off to zero at the edges, and is quite constant over time. The concentration at the centre of the profile is approximately 1.7 to 2.3×10^{-4} (m.kg/m³).

The horizontal plume profile with the compartment present is presented below in Figure 5.9.

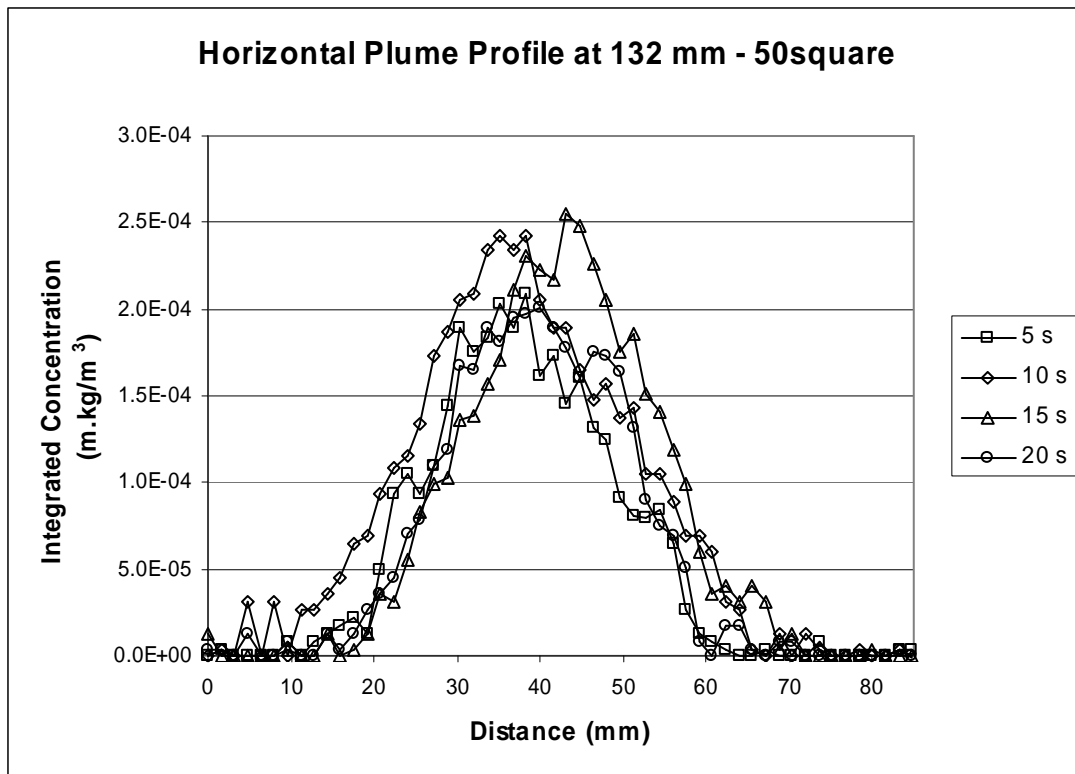


Figure 5.9 - Horizontal profile with compartment present

This profile again has the expected shape and is again quite constant over time but there is an important difference. The centreline concentration seen in this case is approximately 1.9 to 2.5×10^{-4} (m.kg/m³), which is higher than that seen in the previous free plume scenario. The above figures show that while there are some fluctuations, over time the structure of the plume is relatively steady. The comparison between the free and confined plumes can be more easily seen with time averaged data plotted on the same axes, as in Figure 5.10.

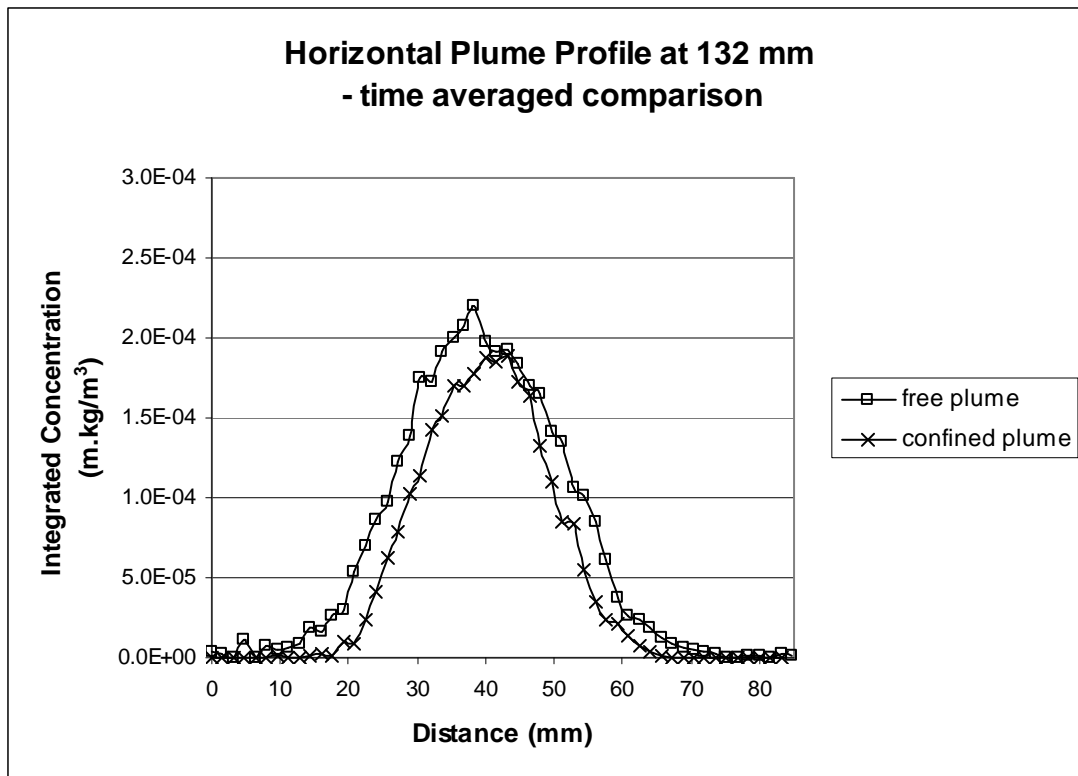


Figure 5.10 – Time averaged horizontal profile comparison of the free and confined plumes

The above direct comparison shows that at a given point in the plume, the confined plume is more concentrated than the free plume. This is a very important result as it indicates that in the free plume example, more fresh water is able to enter the plume and thus it is more dilute. This is a key finding and provides some guidance as to possible areas that might be important when it comes to model this scenario. This is also important from a fire engineering standpoint as it means that there will be less smoke in the room which is more concentrated. This has implications in terms of tenability and visibility within the room as well as the requirements needed to extract this smoke.

Vertical Profiles

In order to investigate and confirm this apparent reduction in entrainment, the vertical profiles of the plume will be considered. Again Imagestream is used to generate the data and does so by plotting the integrated concentration of a one pixel strip taken vertically down through the plume from the source location at each time step. The plume height is considered to a height of 150 mm only as in the case of the confined plume the layer begins to descend which would lead to an artificial increase in integrated concentration for the purposes of this assessment. Figure 5.11 shows the vertical plume profile for the free plume scenario.

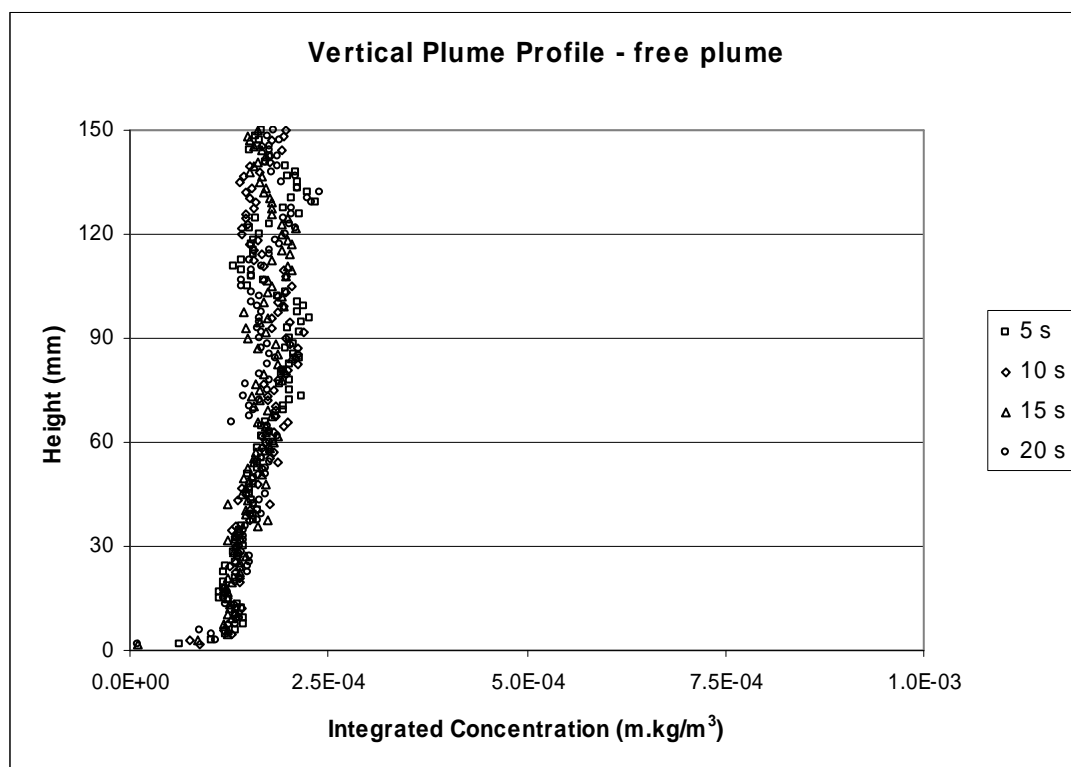


Figure 5.11 - Vertical profile of the free plume

The above figure shows the centreline concentration of the plume to have little variance ranging from around 1.4×10^{-4} to 2.1×10^{-4} m.kg/m³ as well as remaining fairly constant over time.

The vertical plume profile with the compartment present is presented below in Figure 5.12.

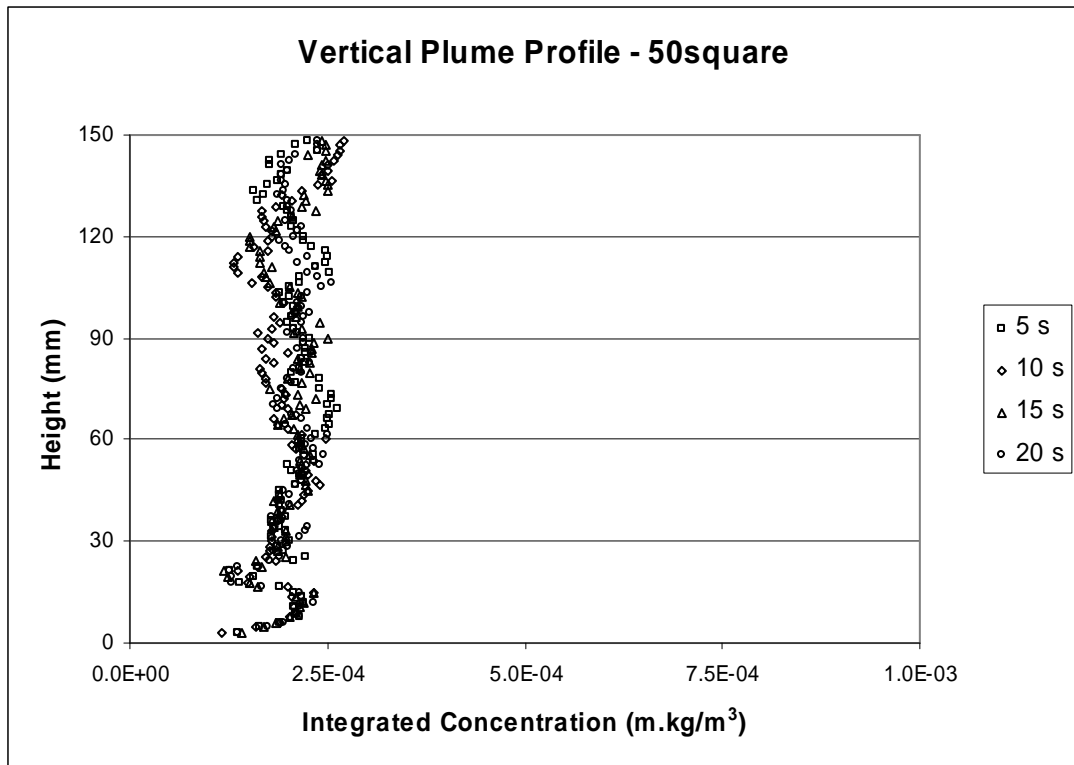


Figure 5.12 - Vertical profile with compartment present

The above diagram shows that the integrated concentration down the centre of the plume is relatively steady and constant over time but in this case it has a higher concentration of 1.5×10^{-4} to 2.5×10^{-4} m.kg/m³, compared with that from the free plume of 1.4×10^{-4} to 2.1×10^{-4} m.kg/m³.

As with the horizontal profile plots, we can average the above data over time and present them on the same set of axes for direct comparison. This is shown below in Figure 5.13.

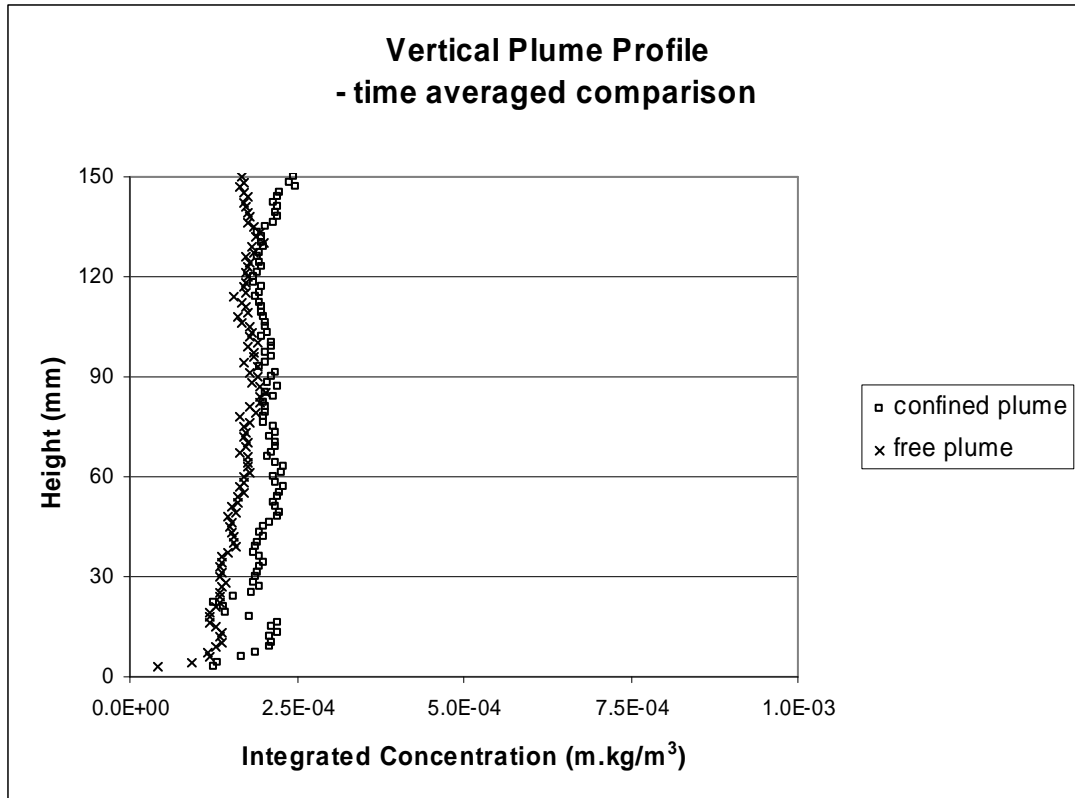


Figure 5.13 – Time averaged horizontal profile comparison of the free and confined plumes

This vertical profile of the plume provides us with further evidence that the plume is more concentrated when confined by the compartment because it is entraining less ambient fluid due to the constrictions of the room.

5.5. Spread Assumption

One of the assumptions made when proposing the initial layer height model was that the spread constant, k_T , was 0.15 (Kikkert *et al.* 2007). The current model does not appear to accurately predict the descent of the layer height so the suitability of this parameter was investigated using images in Imagestream and appropriate Matlab algorithms. This was done by taking a time average of 4 seconds long (100 frames) from the time the plume hits the ceiling of the compartment, which was 2 seconds from the beginning of the experiment. When considering the free plume the averaging was done at the equivalent time since the experiment began, i.e. from 2 seconds till 6 seconds after the beginning of the experiment. Time averaging was shown to be appropriate in this case when considering contour plots of the plumes shown in the previous section which did not change significantly over time.

The integrated maximum centreline concentration was tracked using the Matlab algorithm described in Section 4.9. The three percent experiments compared with the free plume are presented below in Figure 5.14.

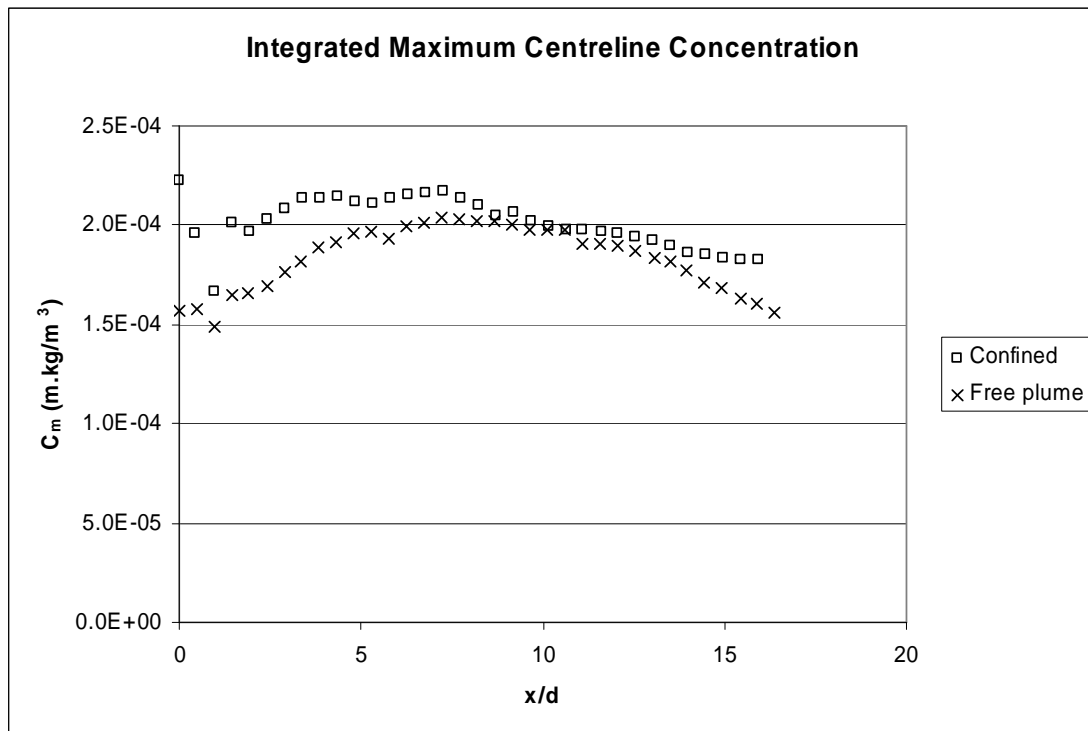


Figure 5.14 – Integrated Maximum centreline concentration for free and confined plumes.

These results determined using the Matlab algorithm can be seen to be consistent with integrated concentrations seen in the previous section when the horizontal and vertical plume profiles were considered. The above graph also supports the trend that the confined plume in the compartment results in a more concentrated plume than is seen in the unobstructed case.

As previously mentioned, a k_T value of 0.15 has in it the inherent assumption of a top hat concentration distribution across the plume. The algorithm is able to fit a Gaussian profile to the integrated concentration cross section and use this to obtain a more accurate figure for k_T . A Gaussian profile is matched to an equivalent top hat profile by conserving the mass and momentum fluxes at a given cross-section.

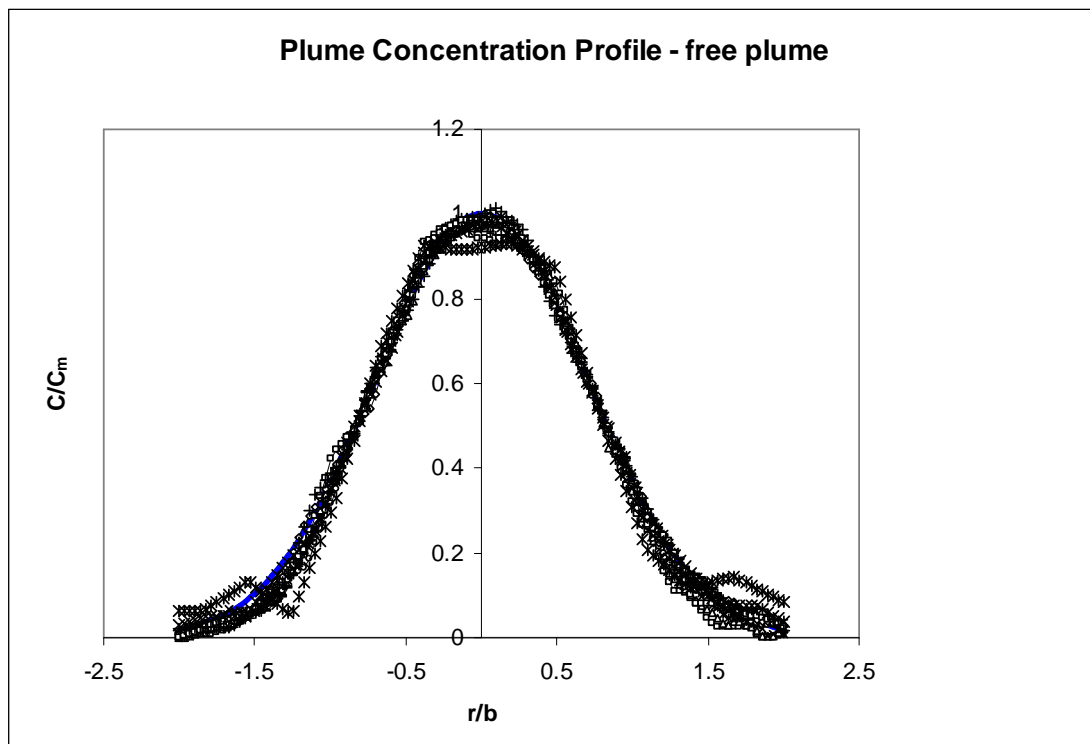


Figure 5.15 – Gaussian fit of integrated concentration profile for the free plume

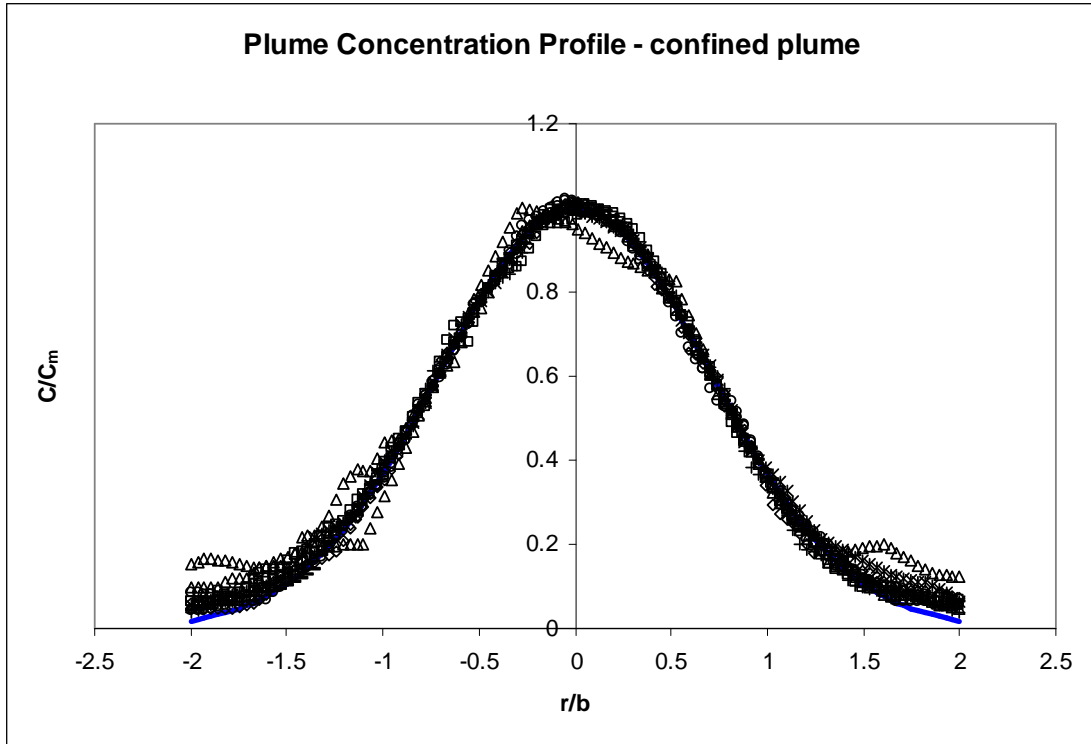


Figure 5.16 – Gaussian fit of integrated concentration profile for the confined plume

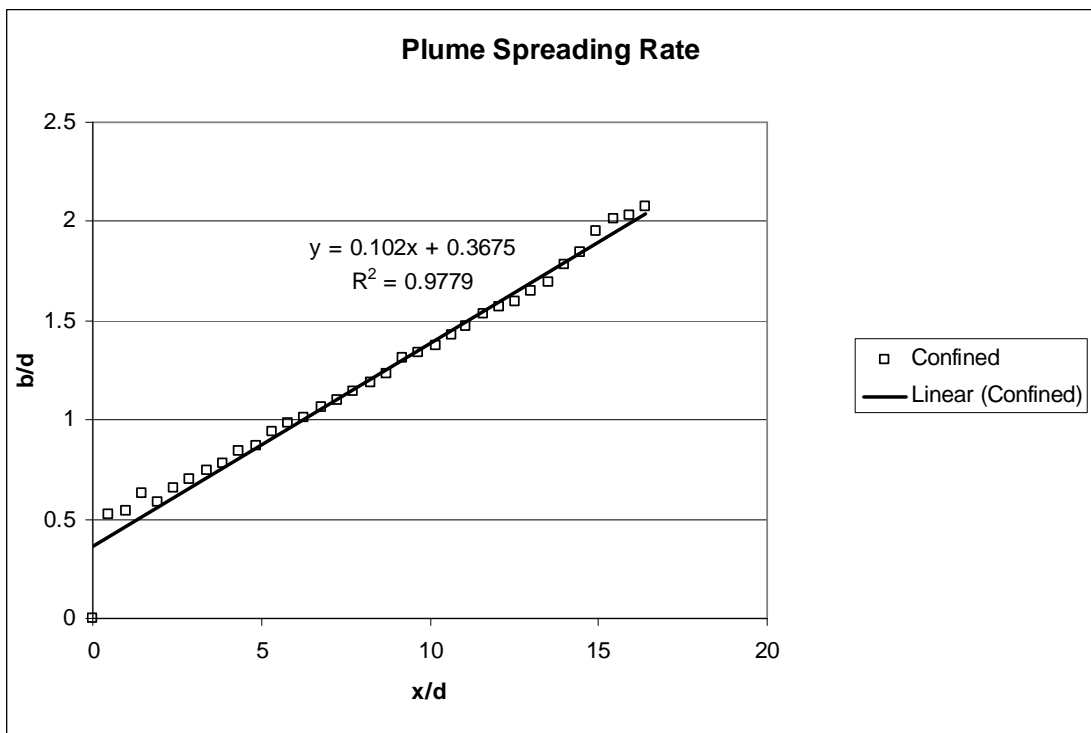


Figure 5.17 – Plume spreading rate comparison for the confined and free plumes

Considering the slope of the spreading rate above, we see that it is significantly different from the initial assumption of 0.15. This provides valuable insight into what

is happening in the experiments, compared to what is predicted to occur in the model. If a larger than appropriate value of k_T is used the plume is spreading faster in the model than it is in reality and this means that the model plume is entraining too much ambient fluid. Thus the model underestimates the layer height and plume concentrations.

If the spreading rate constant is too for the predicted model the ambient fluid is entraining into the plume faster leading to more mixing and greater shear forces. This means larger eddys are forming at the edges of the plume and it therefore spreads at a greater rate.

We can compare this spreading rate result with previous work done in this area. Kikkert (2006) carried out extensive work on characterising two and three dimensional buoyant jets and plotted the spreading rate against position, both non-dimensionalised by the port diameter, as above but over a far greater range of data. This work is plotted in Figure 5.18 along with the data from the current study.

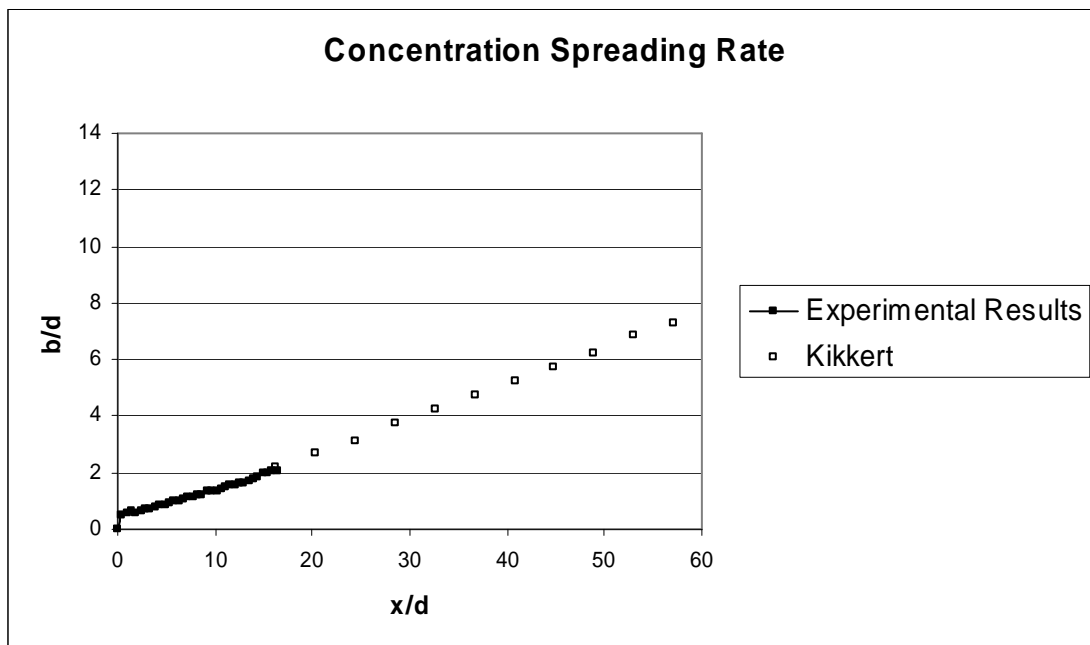


Figure 5.18 – Plume spreading rate comparison with Kikkert (2006)

The above comparison shows that while the data from this study is not many port diameters from the source compared with that of Kikkert (2006), it fits the trend well and gives assurance to the accuracy of the spreading rate data that has been obtained.

The layer height model is reconsidered with the adjusted value for k_T of 0.102 and is presented in Figure 5.19 below.

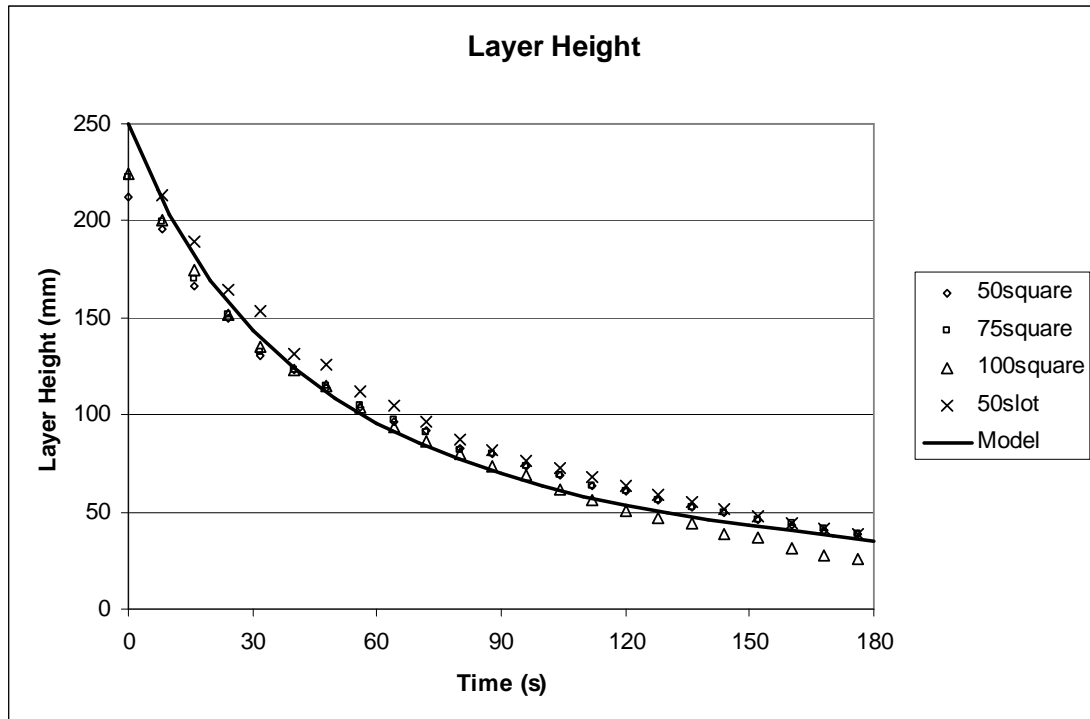


Figure 5.19 – Layer height in the compartment with improved integral model

The above figure shows how well the improved model is now able to predict the layer height within the compartment for the four ceiling openings. This result gives confidence in the integral model and allows us to progress to developing the model further to help calculate the mass flow through the opening.

The six percent density difference experiments which equate to a full scale fire of 650 kW are combined with the data from the three percent experiments and plotted on a single graph. The layer height data from these experiments is shown in a dimensionless manner as per equations 3-6. The results are presented below in Figure 5.20.

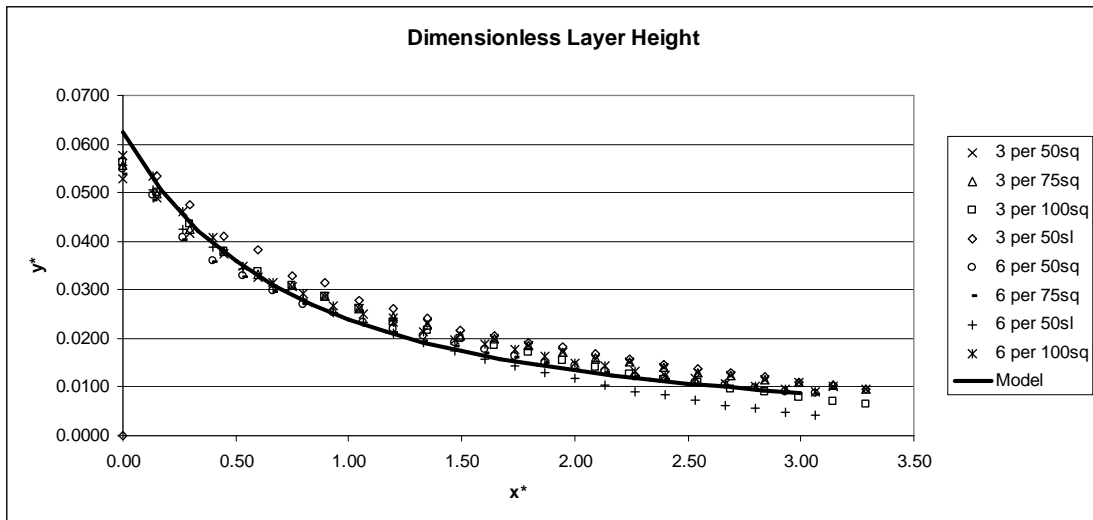


Figure 5.20 – Dimensionless layer height data for three and six percent experiments

As can be seen from the above figure, the data from both experiments collapse well onto an approximately single curve and is in good agreement with the new model predictions.

5.6. Concentration Leaving Vent

The integrated concentration exiting the ceiling vent will now be considered in terms of its shape and the maximum concentration. Imagestream is used to time average 50 frame (two second) blocks of images every 16 seconds in order to remove any fluctuations found in individual frames. Integrated concentration data was extracted across the vent exit. A schematic drawing of the flows which are present is shown in Figure 5.21.

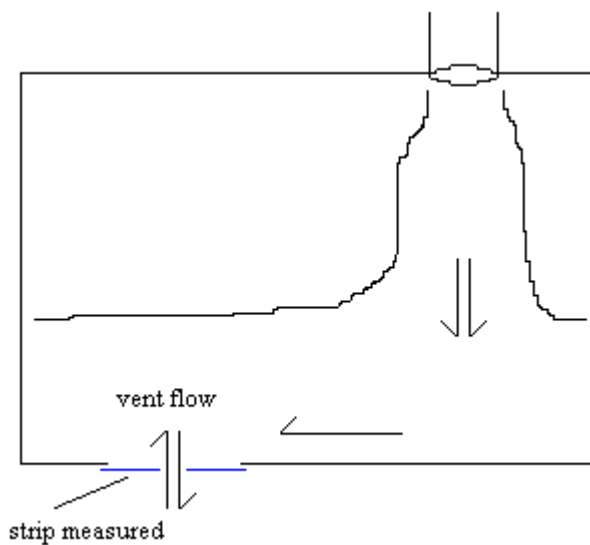


Figure 5.21 – Vent exit concentration schematic

Concentration Profile across Vent

The shape of the concentration profile as it leaves the vent will now be considered. Only the 50 mm square opening is presented here as it is indicative of all the openings which exhibited the same general behaviour. Concentration profiles for other openings can be found in Appendix D. In this case a one pixel wide strip was taken at the immediate exit to the vent and the concentration profile across the vent was extracted. A series of time averaged images was used to avoid excessive fluctuations. The concentration profile across the extent of the vent over time is presented in Figure 5.22 for the 50 mm square ceiling opening.

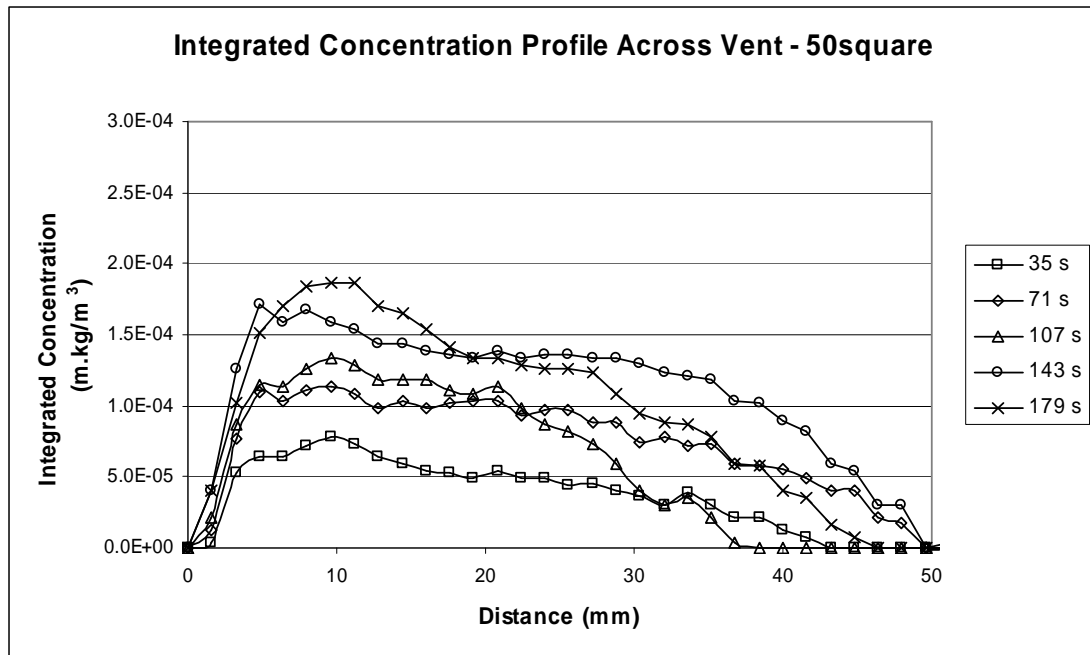


Figure 5.22 – Integrated concentration profile across vent for 50 mm square opening

Over time the profile is seen to become more and more concentrated while still holding its general shape. The profile is seen to be lopsided, tending to one side away from the inlet source. This is as to be expected because as fluid flows towards the vent from above the inlet, its momentum carries it to the opposite side of the vent which was observed in the experiments. Across the vent there is only a gradual increase in concentration which indicates that there is strong mixing occurring before the fluid exits the vent. If the mixing in the compartment was not as significant there would be a sharp increase in concentration along the vent width because the leading edge would still be significantly more concentrated than the rest of the layer.

Maximum Concentration Leaving Vent

The maximum concentration is then determined and the results are plotted for all opening configurations over time for the three percent density difference in Figure 5.23 and the six percent density difference in Figure 5.24.

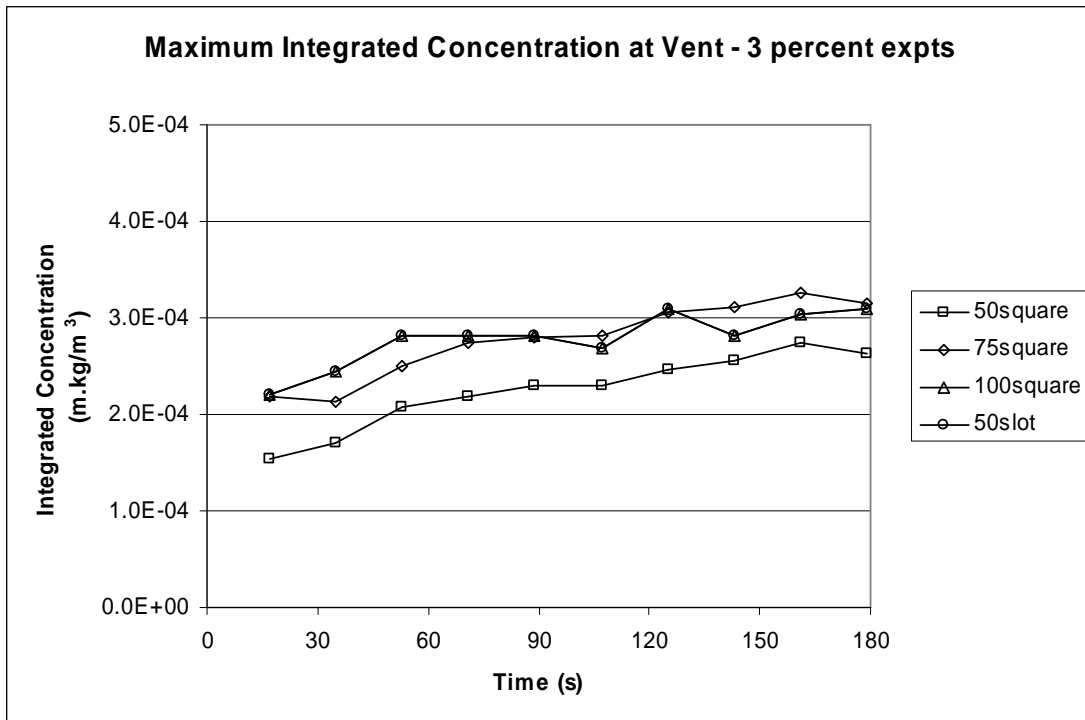


Figure 5.23 – Maximum integrated concentration at vent exit for the 3 percent density difference

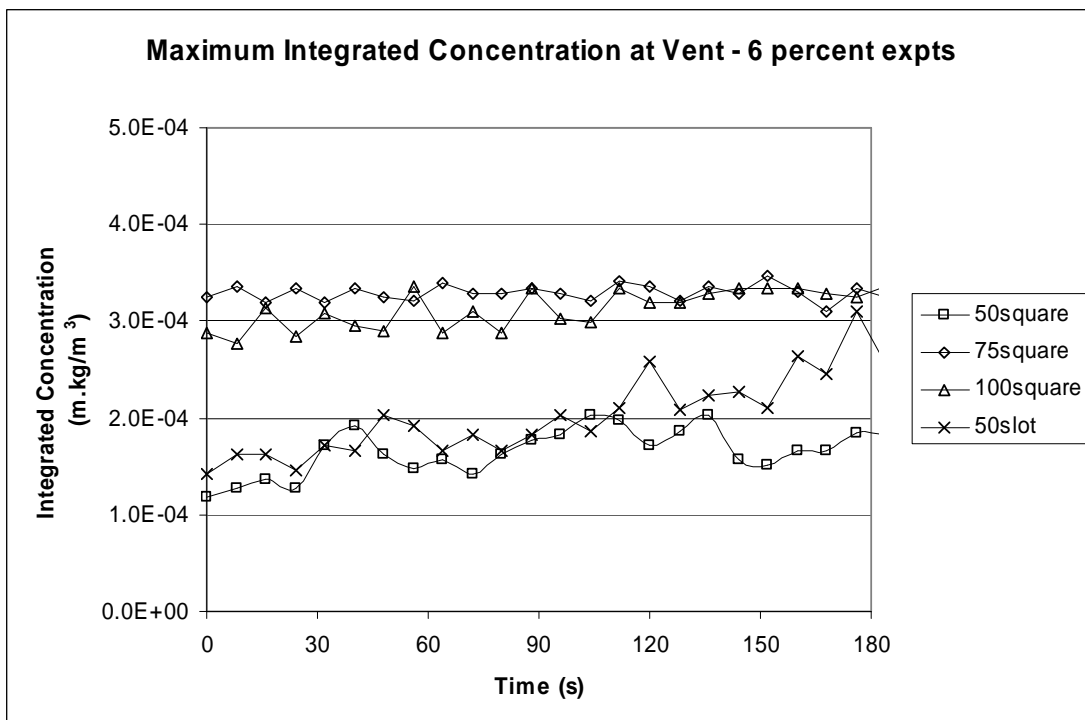


Figure 5.24 – Maximum integrated concentration at vent exit for the 6 percent density difference

The above figures show a steady or slow increase in the maximum concentration at the vent exit.

5.7. Box Filling Model (Baines & Turner 1978)

Previously a model was been developed for the layer height in the compartment. It fits with the experimental data and agrees well when it is made dimensionless. In order to add credibility to the model, however, it must be verified from an independent source. Such a source exists in the box filling model of Baines and Turner (1969). This model was developed from a theoretical point of view by assuming that the rate of entrainment into the turbulent region is proportional to the mean local upward velocity and that the buoyant element spreads along the top of the compartment and becomes part of the non-turbulent environment at that level. That is to say that a layer is formed at the top of the compartment whose descent can be predicted.

The work of Baines and Turner was a forerunner to the work of Zukoski (1978) who applied it to fire specific purposes, and also of Cooper (1994a) whose contribution has already been discussed. The model works by predicting the time at which a particular layer height is reached according to the following equation.

$$t = \frac{5}{4\alpha} \left(\frac{5\pi}{18\alpha} \right)^{1/3} r^2 H^{-2/3} F_0^{-1/3} \left[\left(\frac{H}{Z} \right)^{2/3} - 1 \right] \quad (5-1)$$

This equation uses an entrainment constant, α , of 0.1. The variable, r , in the above equation is the radius of a circular tank assumed in order to develop the model. The authors use an equivalent area for the top plate area of the compartment to determine their value of r for use in the equations.

There are differences in the way Baines and Turner make their equations dimensionless when compared to the integral model developed in Chapter 3. The layer height is divided by the compartment height as in equation 5-2 but the time scale is calculated using equation 5-3.

$$\xi = \frac{Z}{H} \quad (5-2)$$

$$\tau = \frac{4}{\pi^{1/3}} \alpha^{4/3} \left(\frac{H}{r} \right)^2 \frac{B_0^{1/3}}{H^{4/3}} t \quad (5-3)$$

When plotting the experimental data the height of the layer and the time at which this occurs are both known. These are made dimensionless using the equations above and can be plotted along with the Turner and Baines box filling model and the present integral model for comparison. This is shown in Figure 5.25.

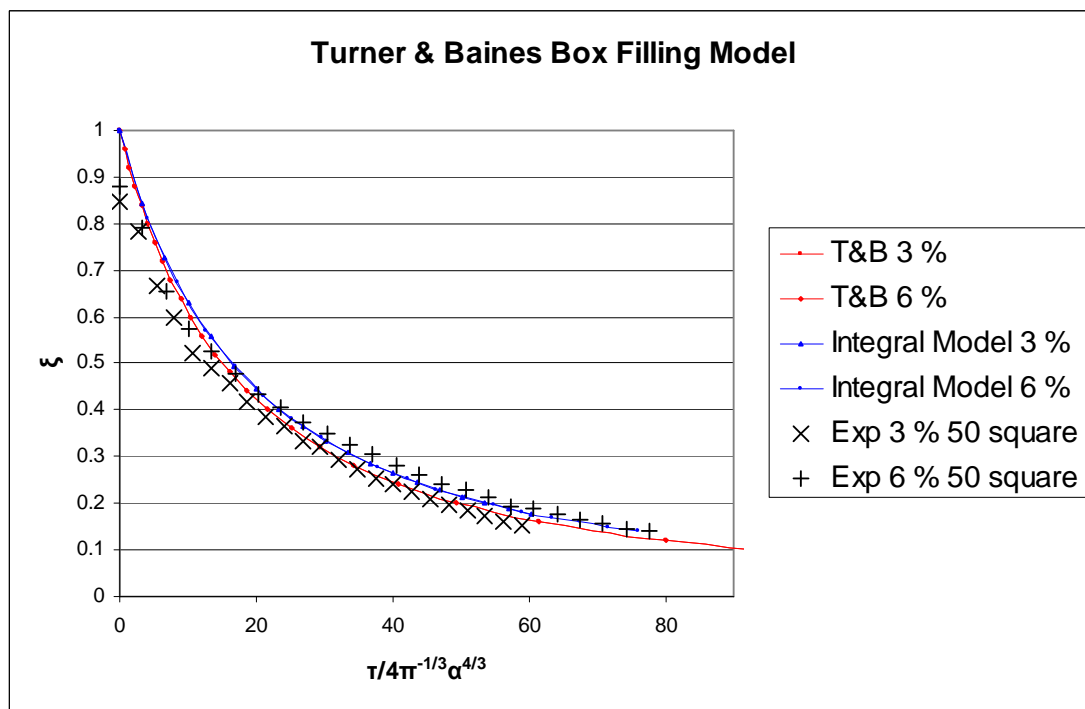


Figure 5.25 – Dimensionless layer height model comparison

The above figure clearly shows the agreement between the box filling model, the integral model and the experimental data. Model predictions for each of the density differences (fire sizes) investigated lie on top of each other, which indicates that they have been non-dimensionalised correctly. The experimental data is seen to match very closely with both of the models. This result provides an independent check of the present integral model and its ability to predict the descent of the layer height.

5.8. Layer Concentration

Using Imagestream, the average concentration in the layer was able to be tracked over time for each of the ceiling openings and for both fire sizes. The layer height at each time step (every eight seconds from formation of the layer) was previously obtained when deriving the layer height model. This was used to determine the concentration in the layer by averaging the data at each pixel across the width of the compartment and between the layer interface and the ceiling of the compartment at each time step.

The concentration in the layer for each density difference is normalised by the initial concentration leaving the source in order to obtain a basis for comparison. This was obtained by closely examining Imagestream images of the plume exiting the source jet and determining the maximum exit concentration for the dye. This was done for each of the density differences and provides a reference point for the plume concentrations. The maximum source concentration for the three percent experiments was found to be $8.21\text{E-}5 \text{ m.kg/m}^3$ and for the six percent experiments was $2.46\text{E-}4 \text{ m.kg/m}^3$.

As discussed in the 'Experimental Observations' section previously, there was significant mixing in the compartment as the layer was established as a result of the plume and then the ceiling jet impacting with the compartment. The source was situated as far as possible from the ceiling vent so that when the upper layer came to exchange with the ambient fluid outside the compartment it was as well mixed as possible. The assumption that the upper layer is sufficiently mixed is an important consideration and while this was checked through analysis of the Imagestream outputs some spatial variation was seen which was not considered when the integral model was established.

Data recorded in the experiments and reduced using Imagestream is integrated data over the entire depth of the compartment. Furthermore the concentration of fluid leaving the source is integrated through the depth of the source. Therefore the non-dimensional layer concentration was multiplied by the ratio of the source depth over the compartment width so that true concentration values are obtained and data from

using this experimental technique can be compared with those that use non-integrated data such as Cooper's equations.

The time was non-dimensionalised by t_0 which has the following relationship:

$$t_0 = \sqrt{\frac{H}{\Delta_0}} \quad (5-4)$$

where Δ_0 is the dimensionless density difference defined previously.

Thus the average concentration in the layer was tracked for each of the ceiling openings and this is presented in Figure 5.26.

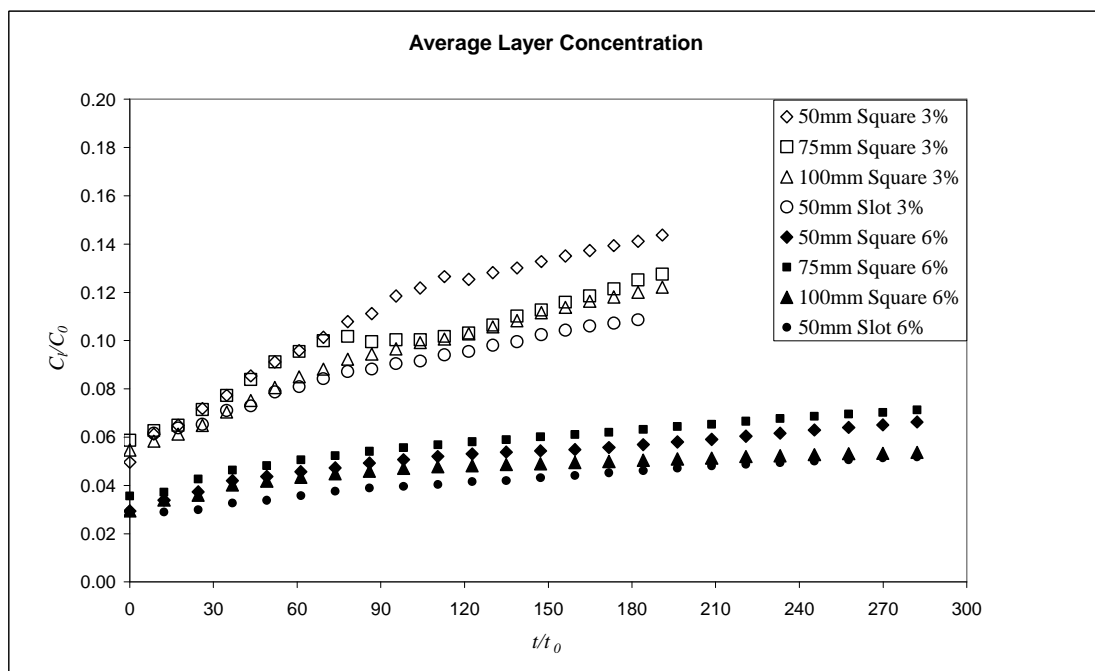


Figure 5.26 – Average layer concentration in the compartment

The above figure shows the average concentration in the layer increasing steadily over time even as the volume in the layer increases as the interface descends. This is because as the layer descends towards the floor, the dye entering the layer is more concentrated as it has not had the chance to entrain as much ambient fluid. For all openings the three percent experiments have a higher concentration than that of the

six percent experiments. This behaviour is as expected because the six percent experiments will create higher buoyancy forces due to the higher density differences and this will lead to more mixing as the plume rises because of the increased shear and turbulence.

In preparation for calculating the exchange flow, the relative layer mass must be calculated as its derivative is required for the exchange flow calculation. The derivative was found by fitting a 6th order polynomial to the experimental results and differentiating the resultant equation.

$$m_L^* = \frac{C_L}{C_0} \frac{V_L}{Q_0 t_0} \quad (5-5)$$

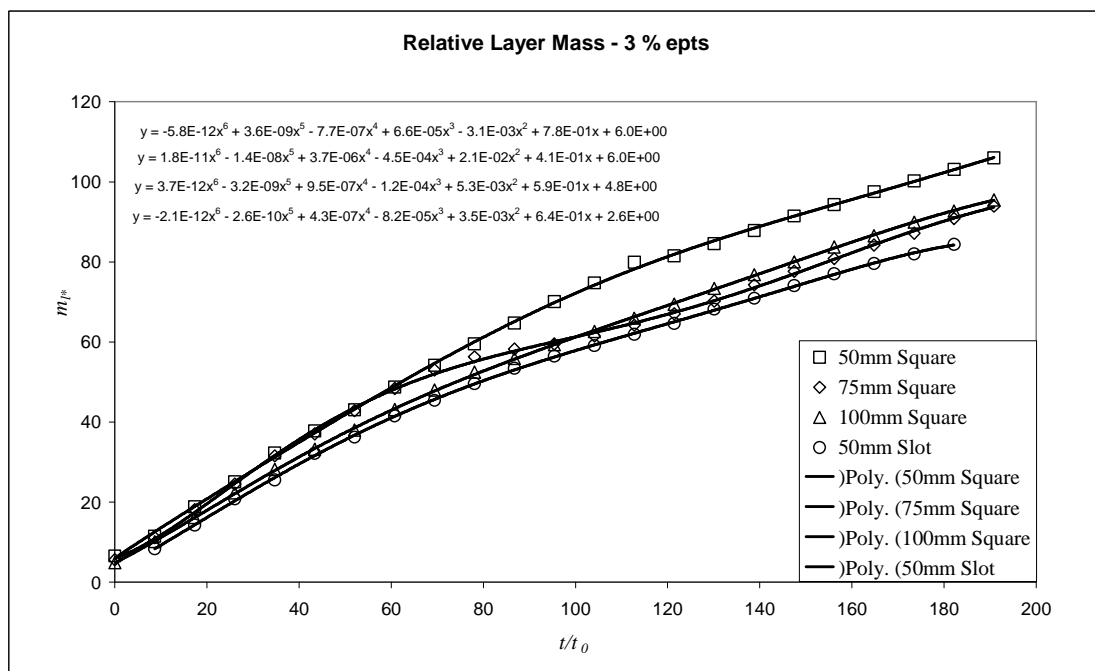


Figure 5.27 – Relative layer mass of 3 percent experiments

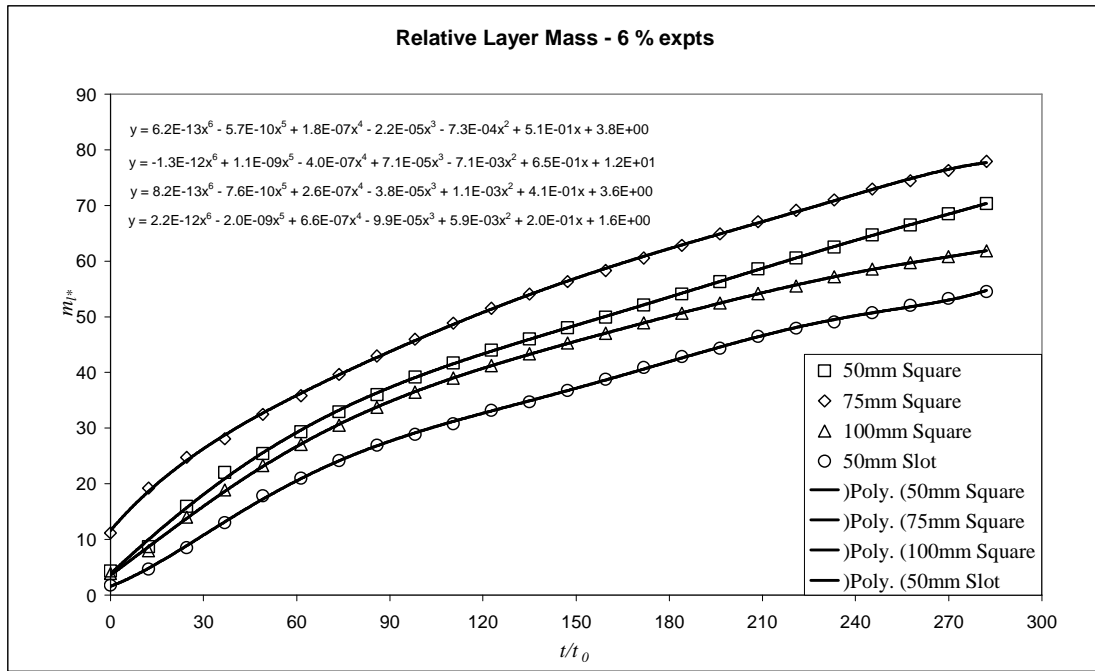


Figure 5.28 – Relative layer mass of 6 percent experiments

5.9. Exchange Flow

Making use of the initial flow rate from the jet, the exchange flow, Q_E , can be calculated according to equation 3-14 and this is shown in Figure 5.29.

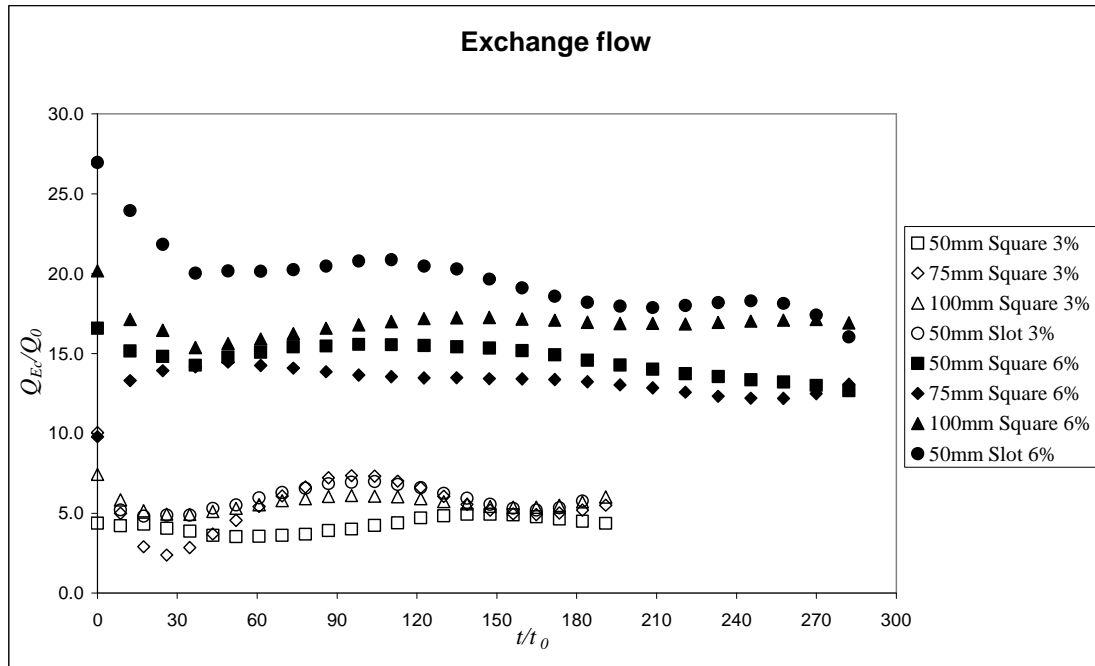


Figure 5.29 – Exchange flow through the opening

Figure 5.29 shows the exchange flow for each of the ceiling openings investigated. In the case of the three percent experiments, the exchange flow is quite steady and fluctuates around 5 times the initial flow rate. The six percent experiments show more variation but reach a steady flow rate as the experiment progresses. The exchange flow rate in this case steadies to between 10 and 17 times the initial flow rate for each of the ceiling openings considered. As expected the exchange flow is greater when a larger ceiling opening is used.

Recall the equation defining the exchange flow constant:

$$\frac{Q_{Ec}}{\Delta_L^{1/2} A_E^{5/4}} = const. = E \quad (3-15)$$

The above relationship provides the basis for scaling the exchange flows calculated from the experimental data. The graph of this relationship over time is shown in Figure 5.30.

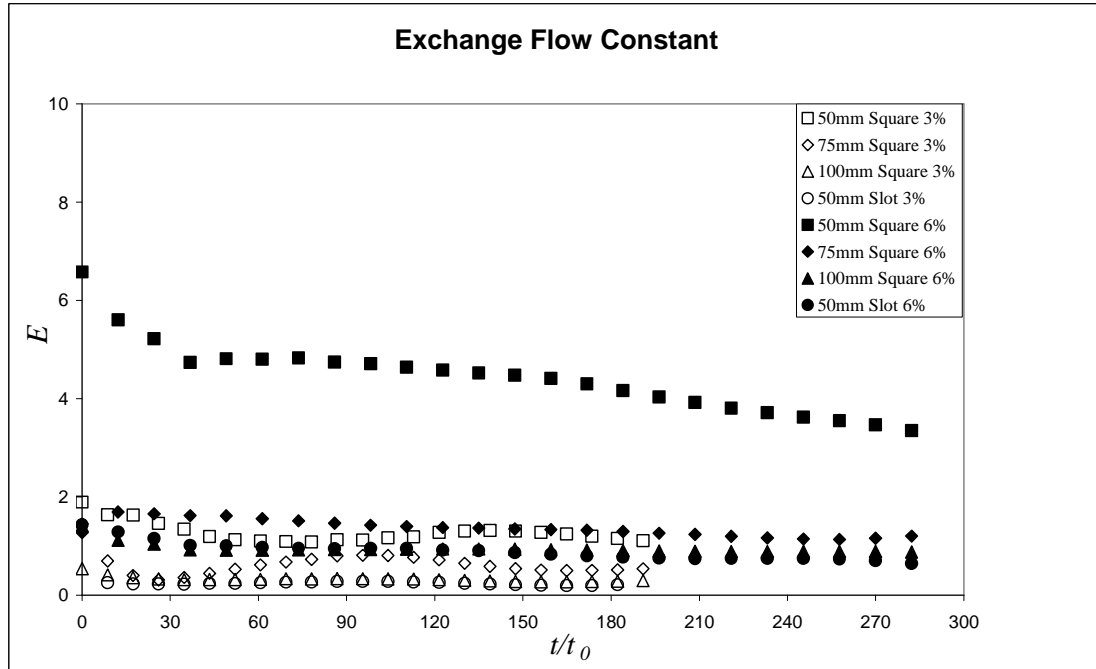


Figure 5.30– Exchange flow constant

Figure 5.30 shows reasonably consistent behaviour for all of the ceiling openings, except for the 50 square opening in the 6 percent experiment which is very large.

5.10. Cooper Comparison

Now that the exchange flow for the experiments has been determined we can compare these results with those obtained from employing Cooper's step-by-step approach outlined in Chapter 2 (Cooper 1994a, 1994b). In view of the approach used by Cooper there are a number of things to consider which will make the exchange flow easier to calculate. First of all we know from the small size of the fires and from experimental observation that we are dealing with a bidirectional exchange flow. Therefore anything regarding calculations of flooding conditions need not be considered.

Furthermore it has already been shown previously that the effect of adding extra fluid into the system is minimal as the exchange flow rates measured are above that of the initial flow rate provided by the source. This means that the pressure difference that is being induced by the source is minimal.

The dimensionless density in the layer can be calculated using the non-dimensional, non-integrated average layer concentration data and multiplying this by the dimensionless density difference of the introduced fluid which is 0.294 for the 3 percent experiments and 0.5886 for the 6 percent experiments. The input data is essentially a ratio of the layer concentration to the concentration of the source fluid. This gives the dimensionless density difference, ε , which is used in Cooper's calculations. Following the steps used by Cooper the maximum exchange flow rate is calculated using equation 2-27.

$$\dot{V}_{ex,max} = 0.055 \left(\frac{4}{\pi} \right) A_E \sqrt{gDi|\varepsilon|} \quad (2-27)$$

The results as calculated using Cooper's equations are presented below showing comparison between each set of experiments.

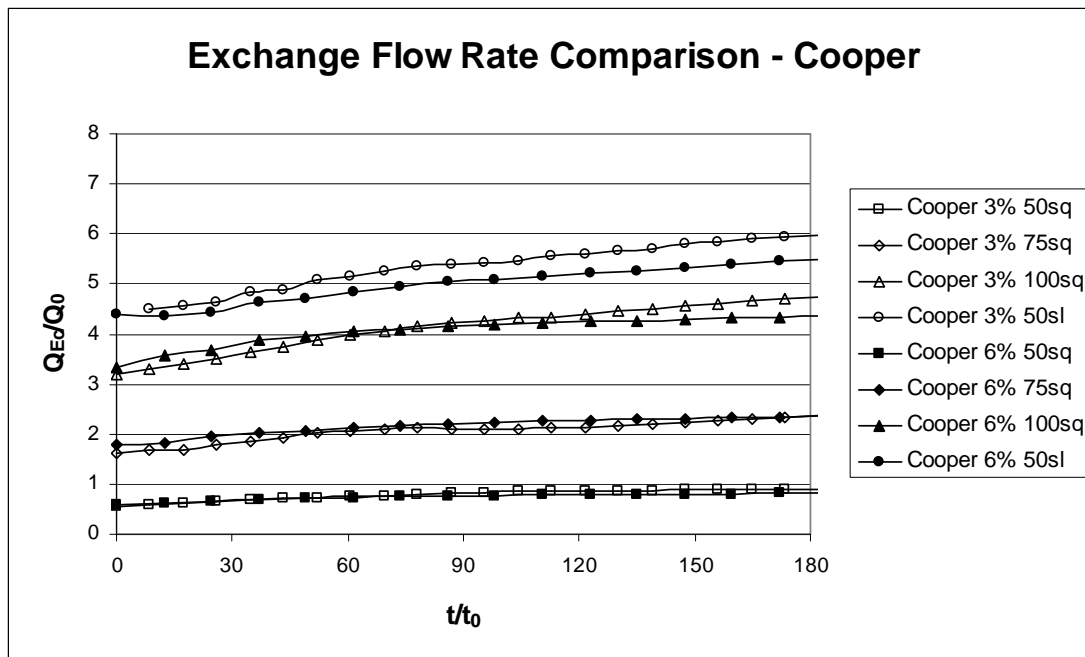


Figure 5.31 - Exchange flow rates calculated using Cooper's equations

The above equation is very interesting as it shows that Cooper's algorithm calculates only a minimal difference in exchange flow from the 3 percent to the 6 percent experiments. The exchange flow can be seen to steadily increase as the opening size increases which is what is expected intuitively and what was seen using the exchange flow calculated using the integral model.

It is important to remember that Cooper uses a circular vent assumption. Square and rectangular vents were used experimentally so when equation 2.26 was employed the diameter of the vent was determined based on a circle of equivalent area as the real vent. With square vents this approximation is expected to be minor but that may not necessarily be the case with the slot ceiling openings which have a high aspect ratio. The exchange flow rate comparison between the experimental data and that found using Cooper's algorithm is shown in Figures 5.32 and 5.33.

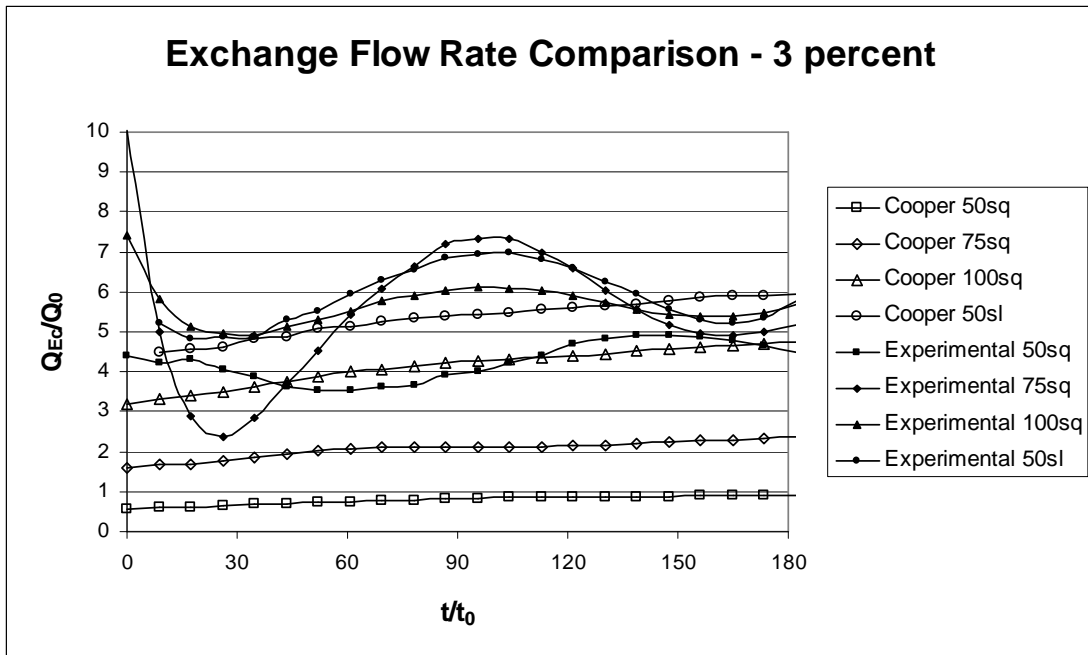


Figure 5.32 - Exchange flow rate comparison with Cooper – 3 percent

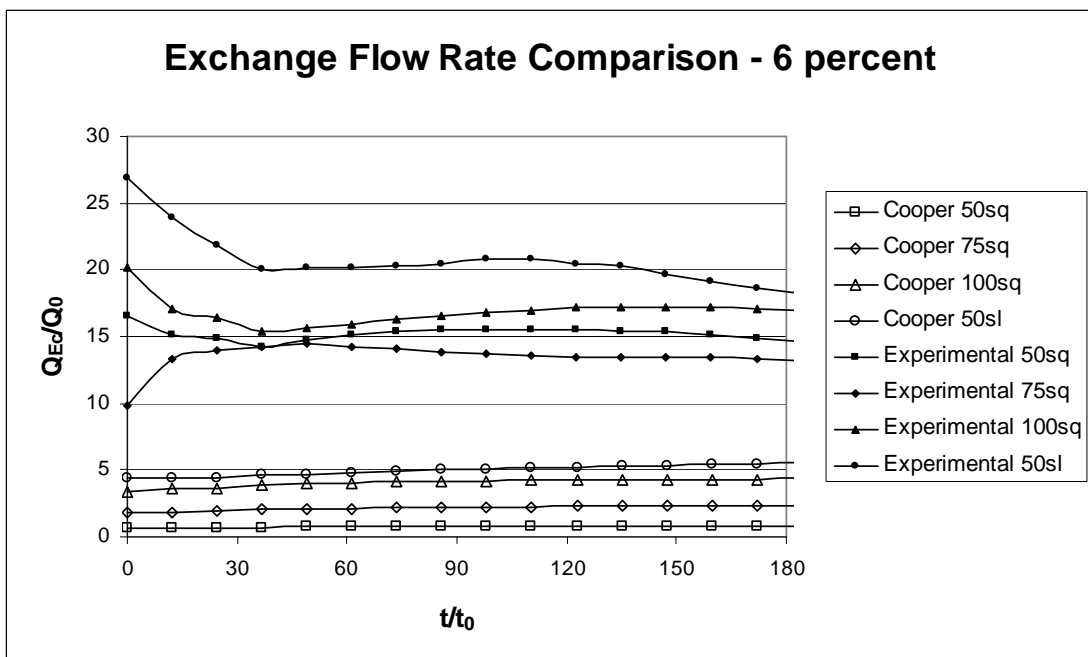


Figure 5.33 - Exchange flow rate comparison with Cooper – 6 percent

The above figures show that while the exchange flow rates in the 3 percent experiments are comparable to those calculated using Cooper’s equations, the same can not be said for the 6 percent experiments. Using the integral model a large difference is seen between the two series of experiments resulting in a large exchange flow of 15 to 20 times the source flow. When the step-by-step approach of Cooper is

used however there is very little difference between the different densities that were used which results in a marked difference when comparing the exchange flow rates of the 6 percent experiments.

The exchange flow constants are now compared for each set of experiments and the results are presented below in figures 5.34 and 5.35.

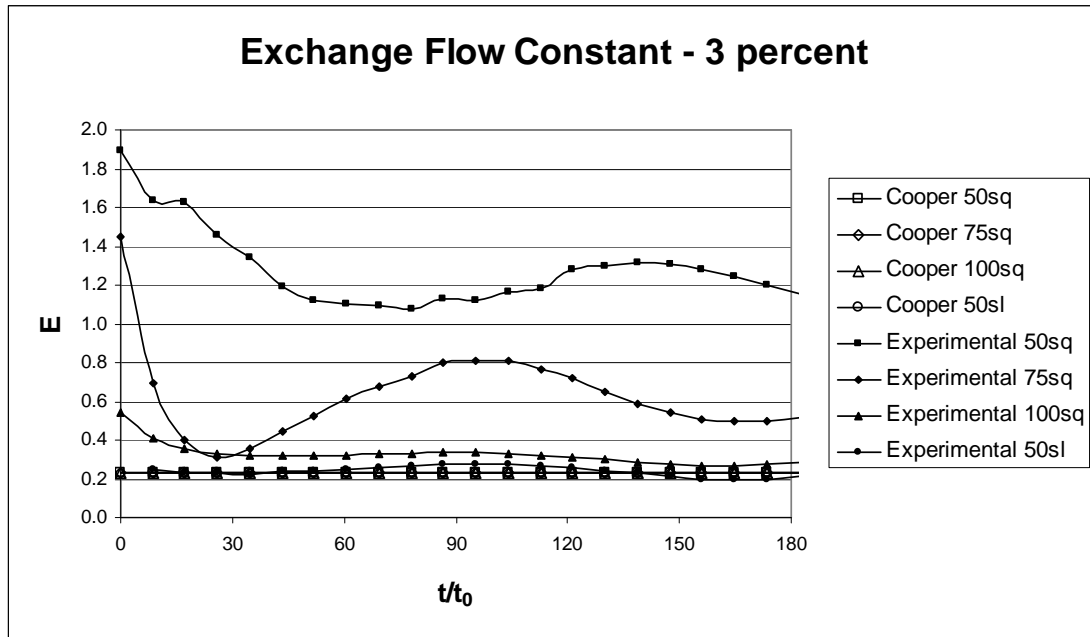


Figure 5.34 - Exchange flow constant comparison with Cooper – 3 percent

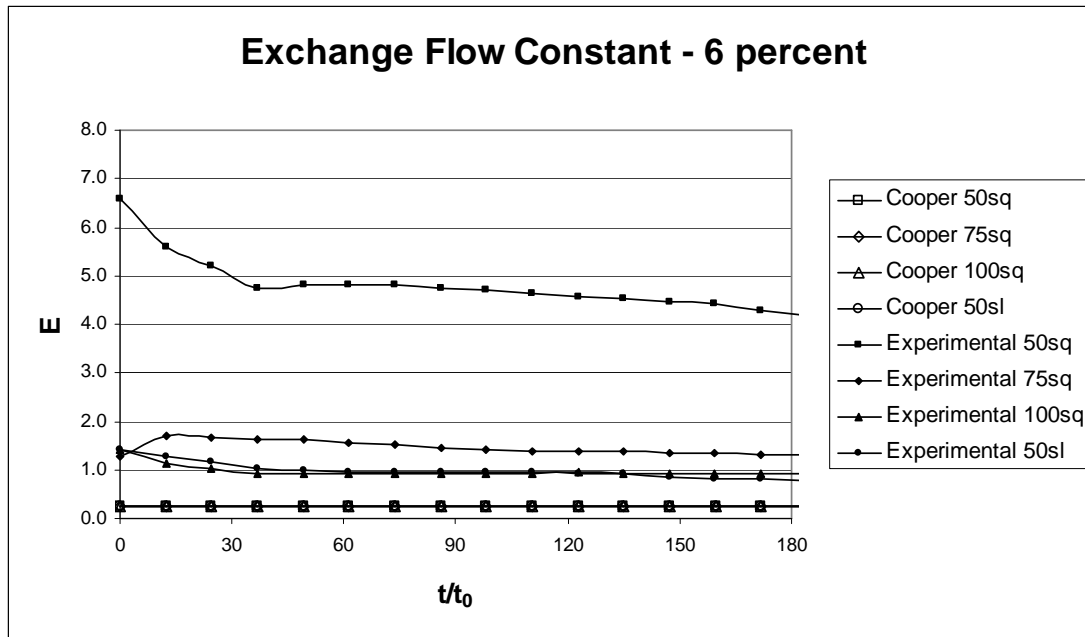


Figure 5.35 - Exchange flow constant comparison with Cooper – 6 percent

The above figures show that Cooper's method predicts an exchange flow constant of 0.23 for all experiments. The fact that the numbers calculated are in fact a constant is very encouraging. The experimental results, while not as consistent generally compare well to this figure. The exception to this however is where the exchange flow constant can be seen to be very large for the 50square opening experiment.

5.11. Discussion

There have been a number of issues and questions raised in this work and this section discusses these and provides further insight into the technical data already obtained. The performance of the integral model is discussed along with comparisons to the work of Cooper (1994) that was cited in the literature review.

The layer height model was developed and it was found that the relationship for the dimensionless layer height was as follows from equation 3-6.

$$\frac{z_l}{H} = \frac{1}{\left[1 + \left[\frac{3^4}{2^3} \pi \frac{H}{D} \frac{H}{W} \left(\frac{A_0}{A_B} \right)^2 Fr_0 k_T^4 t^* \right]^{1/3} \right]^{3/2}} \quad (3-6)$$

When dimensionless the layer height from each of the vent openings and each equivalent fire size were found to lie approximately on the same curve. This is the result which is to be expected and allows for comparison with data obtained from others. This result is important because it means that that data obtained under different initial conditions (provided they do not breach the limitations of the model, such as the plume impinging on the vent) can be compared to the data obtained in this series of experiments.

The descent of the layer height should be independent of vent size because the ambient fluid is only able to exchange with the fluid in the upper layer and has a net flow that is small compared to the exchange flow and is equal to the flow into the system. This was true with the exception of the 100 mm slot opening which was the largest vent and led to an unstable interfacial region and additional mixing that was unaccounted for in any of the models. While this is an interesting result the use of this vent was discontinued as it did not allow us to investigate the aims of these experiments.

The consistency of the layer height between experiments will not apply, however, when the ceiling vent is so large or the rate of venting is so high (more common in mechanically vented systems) that the upper layer evacuates around the rim of the opening only and air is drawn through the centre of the vent from the outside directly into the lower layer. This phenomenon is known as plug-holing and was not observed during the conduction of these experiments.

It was initially assumed when developing the integral model that the plume acted in such a way that it was as if the compartment were not present, that is, entrainment into all sides of the plume is not hindered in any way due to the presence of the compartment. This assumption was analysed and was found to be too simplistic and in fact a free plume with no restriction was found to entrain more free fluid and as a result spread faster and was less concentrated. The plume spreading rate that was initially assumed was then adjusted for use in the integral model. This adjusted spreading rate was found to be consistent with the work of Kikkert (2006).

Data obtained from these experiments was able to be compared with that of Turner and Baines (1969) and also with the model developed by Cooper (1994). It is interesting to note that in terms of the layer descent, the models compare very well with each other and with the experiments. It is not until the exchange flows are compared that Cooper's work and the experiments differ.

When the exchange flow rate was calculated it was found that the flow rate was not constant and showed considerable variation. This is possibly because, for the three percent experiments in particular, the density differences across the ceiling vent are relatively small and the exchange flow may be having some trouble establishing itself initially. For this reason the six percent experiments will be more fully representative of a fully established exchange flow.

The exchange flow rate was found to be only approximately six times the introduced flow rate in the case of the three percent experiments and was larger for the six percent experiments – around 15 to 20 times. In the saltwater analogue that is approximating the real life scenario, fluid is being introduced into the system, which is not the case in a real fire. This additional fluid has not been taken into account

further when calculating exchange flows and was assumed to be negligible at the beginning of the project.

While the exchange flow would ideally be as large as possible compared to the inlet flow, the figures seen for the six percent experiments are high enough to support the notion of considering the inlet flow to be negligible. The three percent experiments however are not really large enough to make this assumption and is a limitation of the model.

The exchange flow rate calculated was found to be comparable to, although higher than, what Cooper's equations predict for the three percent experiments. The six percent experiments however were much higher than Cooper's. This is interesting because we know that fire size (or density difference) is the driving force when considering flows of hot gases in a compartment and we would expect that for a fire that is twice as large that the exchange flow would be significantly higher. This is what is seen when the integral model is used to predict the exchange flow but Cooper's algorithm does not reflect this. In fact when the Cooper method is used the predicted exchange flow is almost identical regardless of the density difference. As the opening size was increased the Cooper method predicted a steady increase in the amount of fluid flow through the opening which is what was expected and seen using the integral model. These findings appear to be a major issue with the Cooper algorithm as it shows that it does not adequately compensate for changes in density difference.

The exchange flow constant was found to be very large for some of the experiments but when Cooper's method was used it was seen to be consistent through time and between experimental series. This number is essentially a densimetric Froude number for the system however the approximation is crude. This is because it fails to take into account some of the more detailed geometric effects. For example this does not take into account difference between the square and rectangular openings that were used in the experiments and the fact that Cooper's algorithm was based on data from experiments using circular vents. It was observed during the conduction of the experiments that the corners of the openings were important to the flow structure as this is where much of the flow seemed to be focussed. As the experimental data was

collected using concentrations that were integrated across the opening and the compartment some of this detail was lost.

Further possible reasons for differences between the methods are difficult to ascertain as the techniques used to calculate the exchange flow are different in each case. The empirical approach of Cooper was based on a limited data set as this was all that was available at the time but conversely this study is based on mathematical theory and experiments conducted with a saltwater analogue system. Both methods have inherent advantages and disadvantages and the next logical step is to conduct a series of scale experiments of real fire scenarios to add further insight to the problem.

6. Conclusions

A number of key discoveries have been made throughout the course of this work and these findings are summarised here.

Firstly a technique was shown to relate the density difference used in a saltwater analogue system to its fire size in a 'real life' fire scenario. It was found that a density difference of three percent equates to a fire size of 323 kW and a six percent density difference equates to a fire size of 646 kW.

One of the first interesting discoveries that were made was the speed at which the layer interface fell with the largest ceiling opening. With this large opening there was a significant amount of turbulence in the interfacial region leading to additional mixing that was not observed to any significant extent with any of the other ceiling vents.

The implications of this finding are that in a design scenario if a large ceiling vent is present (in this case 40 % of the area of the ceiling) then the descent of the layer will not follow accepted conventions and in fact drops far more rapidly and in an unpredictable manner. This means that the available time for occupants to escape the compartment will be far less than previously thought.

Other than in the situation considered above with the very large ceiling opening, the descent of the layer was found to be independent of vent size. A theoretical model for the layer height descent in a compartment was developed from first principles and then improved by adjusting the spread constant. This was done on the basis of comparison between the plumes generated in the fire compartment and those generated without the compartment present. It was found that the assumption on which the original model was based, that the spreading rate for a plume inside the compartment was the same as if the compartment were not there, was not accurate. The new spread rate data obtained enabled the constant to be adjusted to more accurately reflect the conditions inside the fire compartment. Once non-dimensionalised, the improved model was found to accurately predict the descent

of the layer interface when compared with experiments and another predictive model developed by Turner and Baines (1969).

The rate of exchange was then able to be calculated by developing the integral model further to include the exchange flow through the ceiling opening. The amount of exchange flow was found to steady at around five times the inlet flow rate for the three percent experiments and around 15 times for the six percent experiments when non-dimensionalised. It is noted that a doubling of the density difference, or fire size if considering the real life scenario, leads to an increase of the exchange flow rate through the opening that depends on a higher function.

When the saltwater system was used to replicate a real fire situation it was noted that in order to create the turbulent fluid flow seen in a fire, the flow rate of introduced fluid required was on the order of 1.7 L/min. A real fire has no introduced fluid at all and it was assumed that the amount of fluid generated by the source would not be significant compared to the amount of flow through the ceiling opening. While this may be the case for the six percent experiments that showed the exchange flow was around 15 times the introduced flow, the three percent experiments indicated only a five times exchange flow to introduced flow ratio which indicates there is an inherent error in the data of up to 20 %.

When compared to the work of Cooper, which has been incorporated into the BRANZFire model by Wade, the exchange flow rate was found to compare favourably for the three percent series of experiments but was significantly higher using the integral model for the six percent experiments. Using Cooper's algorithm resulted in very similar exchange flows for both density differences studied for a particular ceiling opening. This appears to be a definite limitation in the use of this technique as it does not sufficiently take into account fire size which we know is a definitive factor when considering smoke and heat production flows.

An exchange flow constant was considered using the integral model results as well as those from using Cooper's method. This was developed by considering that the exchange flow should depend only on the density difference being introduced to the compartment and the size of the opening. The integral model results were quite

consistent, especially considering the three percent experiments but there were some experimental runs that were clear outliers in the analysis. Over all opening sizes and across both density differences studied the exchange flow constant calculated using Cooper's method was consistent and constant at 0.233.

Differences between the two techniques was not expected however as the approximation is necessarily crude and does not take into account more detailed effects such as differences in scale and differences between the square and rectangular openings that were used experimentally and the fact that Cooper's algorithm was developed based on circular vent openings. In fact it was observed during the experiments that the corners of the vents may play a significant role as the flow seemed to focus there.

7. Future Work

There are a number of assumptions used throughout this work which arise from the way the saltwater analogue system is used to replicate a real fire scenario. Future work could encompass using scale models of real fire scenarios to examine the way the analysis developed in this work performs in predicting the conditions in the fire compartment. This would be difficult due to the presence of the smoke and the heat in the fire compartment when it comes to taking measurements and this issue would have to be mitigated as far as possible. Using a scale saltwater model of a real fire scenario has advantages though, because a large range of measurements can be taken instead of having to be calculated from theory such as pressure differences across openings and velocity through openings which would have required the use of time consuming particle tracking velocimetry in the saltwater analogue. A physical model similar to that used by Harrison (2000) would be ideal for such a purpose.

As was discovered through the course of this work, when large openings are present there is potential for the descent of the layer interface to be poorly defined, entrain smoke and descend very rapidly. There is potential for this phenomenon to be investigated further in terms of the conditions under which it begins to occur to a non-negligible extent, how much additional smoke is entrained into the layer and the time available for occupants in these to escape. This could be done using a saltwater analogue system or a scale model of a real fire scenario.

As discussed previously in the literature review, Mills compared the work of Cooper in the form of the BRANZFire zone model developed by Wade, with the CFD model the Fire Dynamics Simulator. He found while early predictions of the layer height and upper layer temperature were accurate, as the simulation progressed errors compounded to give poor results further down the line. There is potential for the layer height and entrainment models developed herein to be expanded and compared with the results obtained from a package such as FDS.

It was found when developing the integral model that the spreading rate of the saltwater plume in the compartment did not accurately match that of a free plume.

There is potential for the extent of this behaviour to be investigated further. For example, providing guidance to the extent at which the spread constant is affected depending on the distance of a plume, in port diameters, to nearby obstructions. This will allow the use of situation specific spread constants which will give more accurate results than simply using the free plume assumption or the figure developed in this report as any source location will have a unique spread constant depending how near it is to walls etc.

It was noticed during observations of experiments in progress that much of the flow seemed to focus in the corners of the ceiling opening, a detail that was lost in the data as it was integrated across the width of the opening or the compartment. This difference may have been responsible for some of the discrepancy between the exchange flow constant found when using the two different methods and it would be a very interesting phenomenon to investigate further. This extent of this effect would be best studied using laser techniques that do not integrate across the width of the compartment and instead are able to take a 'cross section' of the flow. It is likely that the proximity of the corners to each other would also have an effect on the flow.

8. References

Baines, W. D., Turner, J. S., (1969) "Turbulent Buoyant Convection from a Source in a Confined Region: J. Fluid Mech., vol 37, part 1, pp 51 – 80.

Baum, H. R., Cassel, K. W., McGrattan, K. B., and Rehm, R. G. (1995) "Gravity-Current Transport in Building Fires." International Conference on Fire Research and Engineering, Orlando, Florida, 27 - 32.

Baum, H. R., Rehm, R. G., (1984) "Combustion Science and Technology" pp 40, 55-77.

Baum, H. R., Rehm, R. G., (1978) "National Bureau of Standards Journal of Research" pp83, 297.

Brown, W.G., (1962) "Natural Convection through Rectangular Openings in Partitions – 2. Vertical Partitions" International Journal of Heat Transfer, Vol 5, pp 869 – 878.

Cenedese, C., Dalziel, S., (1998) "Concentration and Depth Field Determined by the Light Transmitted Through a Dyed Solution" 8th International Symposium on Flow Visualisation.

Clement, J. M., (2000) "Experimental Verification of the Fire Dynamics Simulator (FDS) Hydrodynamic Model" Ph.D Thesis, University of Canterbury, Christchurch, New Zealand.

Cote, A.E., (1997) editor-in-chief, *NFPA Fire Protection Handbook*. 18th edition. Quincy, MA: National Fire Protection Association, page 1-15.

Cooper, L. Y., (1994a) "Combined Buoyancy and Pressure-Driven Flow through a Horizontal Ceiling Vent" NISTIR 5384, National Institute of Standards and Technology, Gaithersburg, MD, USA.

Cooper, L. Y., (1994b) "VENTCF2: An Algorithm and Associated Fortran 77 Subroutine for Calculating Flow Through a Horizontal Ceiling/Floor Vent in Zone Type Compartment Fire Model" NISTIR 5470, National Institute of Standards and Technology, Gaithersburg, MD, USA.

Emmons, H. W., (2002) “Vent Flows” SFPE Handbook (3rd ed.) Section 2, Chapter 3, National Fire Protection Agency, Quincy, MA.

Epstein, M., (1988) “Buoyancy-driven Exchange Flow Through Small Openings in Horizontal Partitions” *Journal of Heat Transfer*, 110, 885-893.

Epstein, M., and Kenton, M. A., (1989) “Combined Natural Connection and Forced Flow through Small Openings in Horizontal Partitions with Special Reference to Flows in Multi-Compartment Enclosures.” *Journal of Heat Transfer*, 111, pp 980-987.

Fleischmann, C. M., (1994) “Backdraft Phenomena” NIST-GCR-94-646, National Institute of Standards and Technology, Gaithersburg, MD.

Hacker, J., Linden, P. F., Dalziel, S. B., (1996) “Mixing in Lock-release Gravity Currents” *Dynamics of Atmospheres and Oceans*, 24(1-4), pp 183 – 195.

Harrison, R., (2000) “Smoke Control in Atrium Buildings: A Study of the Thermal Spill Plume” ME Thesis, University of Canterbury, Christchurch, New Zealand.

Heskastad, G., and Spalding, R. D., (1991) “Inflow of Air Required at Wall and Ceiling Apertures to Prevent Escape of Fire Smoke.” *Proceedings of the 3rd International Symposium on Fire Safety Science*, Elsevier, pp 919-928.

Hilsenrath, J., *et al.*, (1955) “Tables of Thermal Properties of Gases” NBS circular 564, National Institute of Standards and Technology, Gaithersburg, MD, USA.

Hunt, G. R., Cooper, P., Linden, P. F., (2001) “Thermal Stratification Produced by Plumes and Jets in Enclosed Spaces” *Building and Environment*, 36, pp 871 – 882.

Karlsson, B., Quintiere, J. G., (2000) “Enclosure Fire Dynamics” USA.

Kelly, A. A., (2001) “Examination of Smoke Movement in A Two Story Compartment Using Salt and Computational Fluid Dynamics Modelling” MS Thesis, University of Maryland.

Kikkert, G. A., (2006) “Buoyant Jets with Two- and Three-dimensional Trajectories” PhD Thesis, University of Canterbury, Christchurch, New Zealand.

Kikkert, G. A., Davidson, M. J., Nokes, R. I., (2007) “Characterising Strongly-advected Discharges in the Initial Dilution Zone” *Environmental Fluid Mechanics*, 7, 1, pp 23 – 41.

Klote, J. H., Milke, J. A., (2002) “Principles of Smoke Management” American Society of Heating and Air-Conditioning Engineers, Atlanta, Ga.

Lin, Y.J.P., Linden, P. F., (2002) “Buoyancy-driven Ventilation Between Two Chambers” *Journal of Fluid Mechanics*, Vol 463, pp 293 – 312.

Lin, Y.J.P., Linden, P. F., (2005) “The Entrainment Due to a Turbulent Fountain at a Density Interface” *Journal of Fluid Mechanics*, Vol 542, pp 25 – 52.

Linden, P. F., (1999) “The Fluid Mechanics of Natural Ventilation”, *Annual Review of Fluid Mechanics*.

McGrattan, K. B., (2004a) “Fire Dynamics Simulator (Version 4): Users Guide” Building and Fire Research Laboratory and National Institute of Standards and Technology, Gaithersburg, MD, USA.

McGrattan, K. B., (2004b) “Fire Dynamics Simulator (Version 4): Technical Reference Guide” Building and Fire Research Laboratory and National Institute of Standards and Technology, Gaithersburg, MD, USA.

McGrattan, K. B., (2005) “Fire Dynamics Simulator (Version 4.06)” Building and Fire Research Laboratory and National Institute of Standards and Technology, Gaithersburg, MD, USA.

McBryde, J.D., (2006) “Experimental and Numerical Modelling of Gravity Currents Preceding Backdrafts” ME Thesis, University of Canterbury, Christchurch, New Zealand.

Mills, C. K., (2004) “Comparison of Flow Predictions Made by BRANZFire and Fire Dynamics Simulator for Shallow Horizontal Ceiling Vents” ME Thesis, University of Canterbury, Christchurch, New Zealand.

Nokes, R., (2007) "Imagestream Version 6.01" University of Canterbury, Department of Civil Engineering, Christchurch, New Zealand, Image Processing Software.

Nokes, R., (2006a) "Imagestream Version 5.02: System Theory and Design" University of Canterbury, Department of Civil Engineering, Christchurch, New Zealand.

Nokes, R., (2006b) "Imagestream Version 5.02: User's Guide" University of Canterbury, Department of Civil Engineering, Christchurch, New Zealand.

Poreh, M., Morgan, H. P., Marshall, N. R., Harrison, R., (1998) "Entrainment by Two-dimensional Spill Plumes", Fire Safety Journal, Vol 30, pp 1-19.

Rehm, R. G., Baum H. R., (1978) "The Equations of Motion for Thermally Driven Buoyant Flows", Journal of Research of the National Bureau of Standards, Vol 83 (No 3), pp 297-308

Rehm, R. G., McGrattan, K. B., Baum, H. R., Cassel, K. W., (1997) "Transport by Gravity Currents in Building Fires", Fifth International Symposium of Fire Safety Science, Melbourne, Australia, pp 391-402.

Rooney, G. G., Linden, P. F., (1997) "Strongly Buoyant Plume Similarity and Small-fire Ventilation" Fire Safety Journal, 29, pp 235 – 258.

Shin, J. O., Dalziel, S. B., and Linden, P. F. (2004). "Gravity currents produced by lock exchange." Journal of Fluid Mechanics, 521, 1-34.

Steckler, K. D., Baum, H. R., and Quintiere, J. G., (1986) "Salt Water Modelling of Fire Induced Flows In Multicompartmen Enclosures." Twenty-first Symposium (International) on Combustion, 143-149.

Tieszen, S. R., (2001) "On the Fluid Mechanics of Fires" Annual Review of Fluid Mechanics, 33, 67 – 92.

Wade, C. A., (Revised 2003) "BRANZFire Technical Reference Guide" Study Report No. 92, BRANZ, Wellington, New Zealand.

Weng, W. G., Fan W. C., (2002) “Experimental and Numerical Study on Salt Water Modelling of Gravity Current Prior to Backdraft in a Compartment” *Journal of Applied Fire Science*, 11(3), pp 279-289.

Zukoski, E. E., (1978) “Development of a Stratified Ceiling Layer in the Early Stages of a Closed-room Fire” *Fire and Materials*, vol 2, no. 2.

9. Appendix A

9.1. Matlab Algorithm

Provided with thanks by Cameron Oliver, University of Canterbury, Christchurch, New Zealand 2007.

```
function[track,crossSectionData,crossSectionRadius,gaussianParameters
] =
scalartraverse(scalarMatrix,griddx,griddy,sourcecx,sourcecy,sourceAngle
InDegrees,stepLength,initialCrossSectionWidth,numberOfMovements,numbe
rOfFitIterations)
%First cell in scalarMatrix is defined to be at coords x=0,y=0.
%sourceAngleInDegrees is defined as angle from positive x axis,
towards
%positive y axis. Also, this is defined over a regular grid
%(griddx=griddy).

CROSS_SECTION_NUMBER_OF_INTERPOLATION_PTS=50; %wouldn't want to go
too much below 20 cos you'll just be cutting out too much data
DONT_FIT_DATA_BELOW_PERCENTAGE_OF_CROSS_SECTION_MAXIMUM = 0.1;
%Parameters relating to first fit:
FIT_ACROSS_PERCENTAGE_OF_OUTER_DATA = 0.7; %That is, the percentage
distance from the centreline to end of data above min cutoff point
(see above).
FIT_ACROSS_PERCENTAGE_OF_INNER_DATA = 0.7;
%Parameters relating to subsequent fits:
FIT_ACROSS_OUTER_DATA_TO_MULTIPLE_OF_B_VALUE = 0.9;
FIT_ACROSS_INNER_DATA_TO_MULTIPLE_OF_B_VALUE = 0.9;

[n,m]=size(scalarMatrix);
crossSectionWidth = initialCrossSectionWidth;
maxScalar=max(scalarMatrix);

%== A. Determine trajectory =====
disp('Part 1/4: Determining ridge of maximum values via direct
interpolation.');
```

```
Xnew = sourcecx/griddx + 1;
```

```

Ynew = sourcey/griddy + 1;
Thnew = sourceAngleInDegrees*pi/180;
track=zeros(numberOfMovements+1,3);
track(1,1)=sourcecx;
track(1,2)=sourcecy;

for i=2:(numberOfMovements+1)
    %== Evaluate concentration value at distance stepLength away from
    last position, at angles 10 degrees above and 10 degrees below last
    angle.
    Xold=Xnew; %new becomes old
    Yold=Ynew;
    Thold=Thnew;
    Thnew = fminbnd(@interpheight,(Thold-
10*pi/180),(Thold+10*pi/180),[],scalarMatrix,Yold,Xold,stepLength,grid
ddx,griddy);
    Xnew = Xold+stepLength*cos(Thnew)/griddx;
    Ynew = Yold+stepLength*sin(Thnew)/griddy;
    track(i,1)=(Xnew-1)*griddx;
    track(i,2)=(Ynew-1)*griddy;
    track(i,3)=Thnew;
    if((Xnew>n) | (Ynew>m) | (Xnew<0) | (Ynew<0))
        disp(['Warning: Traverse left domain, so numberOfMovements
reduced from ',int2str(numberOfMovements),' to ',int2str(i-2),'.'])
        track(i:numberOfMovements+1,:) = [];
        numberOfMovements=i-2;
        break;
    end
end

%Plot trajectory
figure(1);
[Xcut,Ycut] = meshgrid(0:griddx:(m-1)*griddx,0:griddy:(n-1)*griddy);
surf(Xcut,Ycut,scalarMatrix);
axis equal;
hold on;
[a,b]=size(track);
plot3(track(:,2),track(:,1),ones(a,1)*maxScalar,'-g','LineWidth',2);
view([0,0,1]);
shading flat; %interp;
%lighting phong;

```

```

camroll(90);
title([num2str(sourceAngleInDegrees),'degree interpolated-maximum
trajectory (Part 1/4)']);
clear a b;
hold off;

%== B. Take cross sections and fit to gaussian profile in order to
determine more accurately where centreline is =====
disp('Part 2/4: Taking first round of gaussian fits, using these to
refine ridge definition.');
```

```

crossSectionData =
zeros(numberOfMovements+1,CROSS_SECTION_NUMBER_OF_INTERPOLATION_PTS);
crossSectionRadius =
zeros(numberOfMovements+1,CROSS_SECTION_NUMBER_OF_INTERPOLATION_PTS);
outerbtrack=zeros(numberOfMovements+1,2);
maxValues=zeros(numberOfMovements+1,2);
gaussianParameters=zeros(numberOfMovements+1,3);

for i=2:(numberOfMovements+1)
    xC=track(i,1); %x at centre of cross section
    yC=track(i,2); %y at centre of cross section
    theta=track(i,3); %technically the theta between the last
trajectory point and this trajectory point.
    %==Go through and read off data
    for j=1:CROSS_SECTION_NUMBER_OF_INTERPOLATION_PTS;
        dn = -(crossSectionWidth/2) + (j-
1)*(crossSectionWidth/(CROSS_SECTION_NUMBER_OF_INTERPOLATION_PTS-1));
        %distance along cross section, between -crossSectionWidth and
+crossSectionWidth.
        xMesh = (xC + sin(theta)*dn)/griddx + 1; %converting here to
mesh terms, rather than true spatial dimension terms
        yMesh = (yC - cos(theta)*dn)/griddy + 1;
        %Make actual interpolation
        crossSectionData(i,j) = interp2(scalarMatrix,yMesh,xMesh);
        %Figure out which is max interpolated value for each cross-
section
        if(crossSectionData(i,j) > maxValues(i,1))
            maxValues(i,1)=crossSectionData(i,j); %value
            maxValues(i,2)=dn; %location

```

```

        end
    end
    %==Now choose the data suitable for fitting over. We want
    ln(scalar) and radius.
    %==First select the data with absolute value greater than the set
    percentage of the cross-sectional (interpolated) maximum
    fitNumberPoints=0;
    for j=1:CROSS_SECTION_NUMBER_OF_INTERPOLATION_PTS

if(crossSectionData(i,j)>DONT_FIT_DATA_BELOW_PERCENTAGE_OF_CROSS_SECT
ION_MAXIMUM*maxValues(i,1))
        dn = -(crossSectionWidth/2) + (j-
1)*(crossSectionWidth/(CROSS_SECTION_NUMBER_OF_INTERPOLATION_PTS-1));
%as before
        fitNumberPoints=fitNumberPoints+1;
        fitdataA(fitNumberPoints,1)=crossSectionData(i,j);
%scalar value
        fitdataA(fitNumberPoints,2)=dn; %radius
    end
    end
    %==Next, select data with radius within set percentages of (non-
    negligible) inner data and outer data.
    clear fitdataB;
    fitNumberPoints2=0;
    if(~maxValues(i,1)==0) %If the maximum in the cross section was
    actually above zero, then fitNumberPoints will be greater than zero.
        outerRadiusCutoff=maxValues(i,2)-(maxValues(i,2)-
fitdataA(1,2))*FIT_ACROSS_PERCENTAGE_OF_OUTER_DATA;

innerRadiusCutoff=maxValues(i,2)+(fitdataA(fitNumberPoints,2)-
maxValues(i,2))*FIT_ACROSS_PERCENTAGE_OF_INNER_DATA;
    else
        outerRadiusCutoff=0;
        innerRadiusCutoff=0;
    end
    for k=1:fitNumberPoints
        if((fitdataA(k,2)>outerRadiusCutoff) &
(fitdataA(k,2)<innerRadiusCutoff))
            fitNumberPoints2=fitNumberPoints2+1;
            fitdataB(fitNumberPoints2,1)=fitdataA(k,1); %scalar value
            fitdataB(fitNumberPoints2,2)=fitdataA(k,2); %radius

```

```

        fitdataB(fitNumberPoints2,3)=log(fitdataA(k,1)); %natural
log of scalar value (NB: log in matlab is the natural log, otherwise
notated as ln)
        end
    end
    %==Now we can actually fit that data.
    if(fitNumberPoints2>2) %need at least 3 points to fit a 2nd
order polynomial :-)
        p = polyfit(fitdataB(:,2),fitdataB(:,3),2);
    else
        p = [0 0 0];
    end
    %==Extracting gaussian parameters:
    gaussianParameters(i,1) = (1/abs(p(1)))^0.5; %Spread parameter
(b). Note this equation should technically be (-1/p(1))^0.5.
    gaussianParameters(i,2) = (gaussianParameters(i,1)^2*p(2))/2;
%True centre point (r0)
    gaussianParameters(i,3) = exp(p(3) +
gaussianParameters(i,2)^2/gaussianParameters(i,1)^2); %Scalar max
value (Cm)
    %==Finally, overwrite track x and y with corrected centre point.
    track(i,1) = track(i,1) +
sin(track(i,3))*gaussianParameters(i,2); %x
    track(i,2) = track(i,2) -
cos(track(i,3))*gaussianParameters(i,2); %y

    outerbtrack(i,1)= track(i,1) + sin(track(i,3))*(-
gaussianParameters(i,1)); %b_upper_x
    outerbtrack(i,2)= track(i,2) - cos(track(i,3))*(-
gaussianParameters(i,1)); %b_upper_y

%Plot cross sections:
%figure(1);
%    plot(fitdataA(:,2),fitdataA(:,1),'k. ');
%figure(2);
%    plot(fitdataB(:,2),fitdataB(:,3),'k. ');
%    hold on;
%    if(~isnan(gaussianParameters(i,1)))
%        fplot(@polynomial, [(-crossSectionWidth/2)
(crossSectionWidth/2) min(fitdataB(:,3)) 0],[[],[],[],p(1),p(2),p(3)];
%    end

```

```

% hold off;
%figure(3);
% plot(fitdataB(:,2),fitdataB(:,1),'k. ');
% hold on;
% if(~isnan(gaussianParameters(i,1)))
%     fplot(@gaussian, [(-crossSectionWidth/2)
(crossSectionWidth/2)], [], [], [], gaussianParameters(i,1), gaussianParam
eters(i,2), gaussianParameters(i,3));
% end
% title(i)
% hold off;

end

clear xMesh yMesh xC yC theta innerRadiusCutoff outerRadiusCutoff
maxValues fitdataA fitdataB fitNumberPoints fitNumberPoints2 dn Xold
Xnew Yold Ynew Thold Thnew p;

%Plot updated trajectory
figure(2);
surf(Xcut,Ycut,scalarMatrix);
axis equal;
hold on;
[a,b]=size(track);
plot3(track(:,2),track(:,1),ones(a,1)*maxScalar,'-g','LineWidth',2);
plot3(outerbtrack(:,2),outerbtrack(:,1),ones(a,1)*maxScalar,'-
k','LineWidth',2);
view([0,0,1]);
camroll(90);
shading flat;
title([num2str(sourceAngleInDegrees),'degree first gaussian-fitting
trajectory (Part 2/4)']);
clear a b;
hold off;

%== C. Use new centreline definition to take cross sections in more
accurate directions, and of width=fn(b) =====
disp(['Part 3/4: Making ',int2str(numberOfFitIterations),' further
gaussian-fitting iterations.']);
lnData=zeros(1,CROSS_SECTION_NUMBER_OF_INTERPOLATION_PTS);
for itr=1:numberOfFitIterations

```

```

    %==First, update theta values, using central differencing where
we can
    for i=2:(numberOfMovements+1)
        if(i==(numberOfMovements+1))
            track(i,3) = atan((track(i,2)-track(i-1,2))/(track(i,1)-
track(i-1,1))); %last cross section, so has to use backward
differencing
        else
            if(isnan(track(i-1,2)))
                if(isnan(track(i+1,2)))
                    track(i,3) = NaN; %surrounded by NaN
coordinates, so can't calculate theta.
                else
                    track(i,3) = atan((track(i+1,2)-
track(i,2))/(track(i+1,1)-track(i,1))); %previous coordinate is NaN
so have to use forward differencing
                end
            else
                if(isnan(track(i+1,2)))
                    track(i,3) = atan((track(i,2)-track(i-
1,2))/(track(i,1)-track(i-1,1))); %next coordinate is NaN so have to
use backward differencing
                else
                    track(i,3) = atan((track(i+1,2)-track(i-
1,2))/(track(i+1,1)-track(i-1,1))); %all ok, so use central
differencing
                end
            end
        end
    end
end
end
end
    %==Now go through and interpolate+fit cross sections, based on
previous fit information.
    for i=2:(numberOfMovements+1)
        xC=track(i,1);
        yC=track(i,2);
        theta=track(i,3);
        crossSectionWidth =
gaussianParameters(i,1)*(FIT_ACROSS_OUTER_DATA_TO_MULTIPLE_OF_B_VALUE
+ FIT_ACROSS_INNER_DATA_TO_MULTIPLE_OF_B_VALUE);
        outerLimit = -
gaussianParameters(i,1)*FIT_ACROSS_OUTER_DATA_TO_MULTIPLE_OF_B_VALUE;

```

```

    %==Interpolate off data
    for j=1:CROSS_SECTION_NUMBER_OF_INTERPOLATION_PTS;
        dn = outerLimit + (j-
1)*(crossSectionWidth/(CROSS_SECTION_NUMBER_OF_INTERPOLATION_PTS-1));
%distance along cross section, between -crossSectionWidth and
+crossSectionWidth.
        xMesh = (xC + sin(theta)*dn)/griddx + 1; %converting here
to mesh terms, rather than true spatial dimension terms
        yMesh = (yC - cos(theta)*dn)/griddy + 1;
        %==Make actual interpolation
        if((isnan(xMesh)) | (isnan(yMesh)))
            crossSectionData(i,j) = NaN;
            crossSectionRadius(i,j) = NaN;
            lnData(1,j)=NaN;
        else
            crossSectionData(i,j) =
interp2(scalarMatrix,yMesh,xMesh);
            crossSectionRadius(i,j) = dn;
            lnData(1,j)=log(crossSectionData(i,j));
        end
    end
    %==Fit this data
    p = polyfit(crossSectionRadius(i,:),lnData(1,:),2);
    %==Extract gaussian parameters
    gaussianParameters(i,1) = (-1/p(1))^0.5; %Spread parameter
(b)
    gaussianParameters(i,2) = (gaussianParameters(i,1)^2*p(2))/2;
%True centre point (r0)
    gaussianParameters(i,3) = exp(p(3) +
gaussianParameters(i,2)^2/gaussianParameters(i,1)^2); %Scalar max
value (Cm)
    %==Finally, overwrite track x and y with corrected centre
point.
    track(i,1) = track(i,1) +
sin(track(i,3))*gaussianParameters(i,2); %x
    track(i,2) = track(i,2) -
cos(track(i,3))*gaussianParameters(i,2); %y

    outerbtrack(i,1)= track(i,1) + sin(track(i,3))*(-
gaussianParameters(i,1)); %b_upper

```

```

        outerbtrack(i,2)= track(i,2) - cos(track(i,3))*(-
gaussianParameters(i,1)); %b_lower
    end
    disp(['Iteration ',int2str(itr),' complete.']);
end
%Plot updated trajectory
figure(3);
surf(Xcut,Ycut,scalarMatrix);
axis equal;
hold on;
[a,b]=size(track);
plot3(track(:,2),track(:,1),ones(a,1)*maxScalar,'-g','LineWidth',2);
plot3(outerbtrack(:,2),outerbtrack(:,1),ones(a,1)*maxScalar,'-
k','LineWidth',2);
view([0,0,1]);
camroll(90);
shading flat; %interp;
title([num2str(sourceAngleInDegrees),'degree final trajectory (Part
3/4)']);
clear a b;
hold off;

%== D. Go through and take cross sections on *both* sides, to a width
of 4b. =====
disp('Part 4/4: Extracting final set of data to return to user. ');
%Make the number of interpolation points proportional to the what
we've
%been taking before (w.r.t. width b):
finalNumberInterpolationPoints =
ceil(4*CROSS_SECTION_NUMBER_OF_INTERPOLATION_PTS/(FIT_ACROSS_OUTER_DA
TA_TO_MULTIPLE_OF_B_VALUE +
FIT_ACROSS_INNER_DATA_TO_MULTIPLE_OF_B_VALUE));
clear crossSectionData crossSectionRadius;
crossSectionRadius =
zeros(numberOfMovements+1,finalNumberInterpolationPoints);
crossSectionData =
zeros(numberOfMovements+1,finalNumberInterpolationPoints);
%Now go for it...
for i=2:(numberOfMovements+1)
    xC=track(i,1);
    yC=track(i,2);

```

```

theta=track(i,3);
crossSectionWidth = gaussianParameters(i,1)*4;
outerLimit = -gaussianParameters(i,1)*2;
%==Interpolate off data
for j=1:finalNumberInterpolationPoints;
    dn = outerLimit + (j-
1)*(crossSectionWidth/(finalNumberInterpolationPoints-1));
%distance along cross section, between -crossSectionWidth and
+crossSectionWidth.
    xMesh = (xC + sin(theta)*dn)/griddx + 1; %converting here to
mesh terms, rather than true spatial dimension terms
    yMesh = (yC - cos(theta)*dn)/griddy + 1;
%==Make actual interpolation
    if((isnan(xMesh)) | (isnan(yMesh)))
        crossSectionData(i,j) = NaN;
        crossSectionRadius(i,j) = NaN;
    else
        crossSectionData(i,j) =
interp2(scalarMatrix,yMesh,xMesh)/gaussianParameters(i,3); %C/Cm
        crossSectionRadius(i,j) = dn/gaussianParameters(i,1);
%r/b
    end
end
end

disp('Finished.');
```

%== Appendix: Internal functions =====

```

function z = interpheight(Theta,Z,Yold,Xold,stepLength,griddx,griddy)
    Xnew = Xold+stepLength*cos(Theta)/griddx;
    Ynew = Yold+stepLength*sin(Theta)/griddy;
    z = -interp2(Z,Ynew,Xnew);
```

```

function C = gaussian(r,b,r0,Cm)
    C = Cm*exp(-((r-r0)/b)^2);
```

```

function C = polynomial(r,c3,c2,c1)
    C = c1 + c2*r + c3*r^2;
```

10. Appendix B

10.1. Dimensionless Layer Height Equation

Recall equation 3-5.

$$z_I = \left[\frac{1}{\frac{1}{H^{2/3}} + \frac{3}{2} \frac{1}{DW} \left[3 \frac{\pi^2}{4} B_0 k_T^4 \right] t} \right]^{3/2} \quad (3-5)$$

Divide by H and substitute $B_0 = \frac{\pi}{4} d^2 \Delta_0$

$$\begin{aligned} \frac{z_I}{H} &= \frac{1}{H} \left[\frac{1}{\frac{1}{H^{2/3}} + \frac{3}{2} \frac{1}{DW} \left[3 \frac{\pi^2}{4} B_0 k_T^4 \right] t} \right]^{3/2} \\ &= \left[\frac{1}{\frac{1}{H^{2/3} H^{-2/3}} + \frac{3}{2} \frac{H^{2/3}}{DW} \left[3 \frac{\pi^2}{4} B_0 k_T^4 \right] t} \right]^{3/2} \\ &= \left[\frac{1}{1 + \left[\frac{3^4 \pi^2 H^2}{2^3 4 D^3 W^3} B_0 k_T^4 \right] t} \right]^{3/2} \\ &= \left[\frac{1}{1 + \left[\frac{3^4 \pi^2 H^2 \pi}{2^3 4 D^3 W^3 4} U_0 d^2 \Delta_0 k_T^4 \right] t} \right]^{3/2} \end{aligned}$$

Let $t^* = \frac{t}{t_0}$ where $t_0 = \left[\frac{d}{\Delta_0} \right]^{1/2}$

$$\begin{aligned}
\frac{z_I}{H} &= \left[1 + \left[\frac{3^4}{2^3} \pi \left(\frac{\pi}{4} \right)^2 \frac{H^2 d^2}{D^3 W^3} U_0 \Delta_0 k_T^4 \right]^{1/3} t^* \left(\frac{d}{\Delta_0} \right)^{1/2} \right]^{-3/2} \\
&= \left[1 + \left[\frac{3^4}{2^3} \pi \left(\frac{\pi}{4} \right)^2 \frac{H^2 d^2}{D^3 W^3} U_0 \Delta_0 k_T^4 \left(\frac{d}{\Delta_0} \right)^{3/2} \right]^{1/3} t^* \right]^{-3/2} \\
&= \left[1 + \left[\frac{3^4}{2^3} \pi \left(\frac{\pi}{4} \right)^2 \frac{H^2 d^4}{D^3 W^3} \frac{U_0}{\Delta_0^{1/2} d^{1/2}} k_T^4 \right]^{1/3} t^* \right]^{-3/2}
\end{aligned}$$

Let $\beta = \frac{\pi}{4} d^2$, $\gamma = DW$

$$\begin{aligned}
\frac{z_I}{H} &= \left[1 + \left[\frac{3^4}{2^3} \pi \frac{H}{D} \frac{H}{W} \left(\frac{\beta}{\gamma} \right)^2 Fr_0 k_T^4 \right]^{1/3} t^* \right]^{-3/2} \\
&= \frac{1}{\left[1 + \left[\frac{3^4}{2^3} \pi \frac{H}{D} \frac{H}{L} \left(\frac{\beta}{\gamma} \right)^2 Fr_0 k_T^4 \right]^{1/3} t^* \right]^{3/2}}
\end{aligned}$$

11. Appendix C

11.1. Light Attenuation Equation Derivation

Light is attenuated as it passes through a dyed fluid and can be described by the absorption theory developed by Lambert-Beer (Cenedese and Dalziel 1998).

$$\frac{\partial I}{\partial p} = -\eta I$$

where I light intensity
p path of light ray
η rate of light absorption

For a fluid with a uniform dye concentration c , and a width h , the above equation can be integrated along the light path from $p = 0$ to $p = h_f$. This gives the attenuation ratio shown below where light intensity is a function of the concentration in the fluid and the distance along the path of the light.

$$\frac{I(h_f, c)}{I(0, c)} = e^{-\eta h_f}$$

where $I(h_f, c)$ intensity of light leaving fluid
 $I(0, c)$ intensity of light entering fluid

For low concentrations of dye the relationship between the rate of attenuation and the dye concentration is linear (Cenedese and Dalziel 1998) and this is represented in the following equation.

$$\eta = f(c) = \frac{1}{a}c + b$$

where a empirical attenuation rate constant
b rate of attenuation in fluid with no dye

Using this expression the attenuation ratio can now be expressed as shown below.

$$\frac{I(h_f, c)}{I(0, c)} = e^{-\eta h_f} = e^{-((1/a)c+b)h_f} = e^{-(1/a)ch_f} e^{-bh_f}$$

When there is no dye present in the fluid $c = 0$ so the attenuation ratio can be simplified as follows.

$$\frac{I(h_f, 0)}{I(0, 0)} = e^{-f(c)h_f} = e^{-bh_f}$$

where $I(h_f, 0)$ light intensity leaving un-dyed fluid

$I(0, 0)$ light intensity entering un-dyed fluid

The above equations may now be divided to eliminate the dependence on b , the rate of attenuation in the fluid with no dye.

$$\frac{I(h_f, c)}{I(0, c)} \bigg/ \frac{I(h_f, 0)}{I(0, 0)} = \frac{I(h_f, c)}{I(h_f, 0)} = e^{-(1/a)ch_f}$$

This equation means that only the light intensities leaving the fluid are important and there is no longer any dependence on the light entering the fluid. In experimental terms this means that light intensity readings need only be taken at a single location rather than multiple sites. The above equation now refers to the integrated concentration, i.e. the thickness of the fluid multiplied by the dye concentration. In light attenuation experiments it is the integrated concentration that is actually measured. The above equation can be presented in terms of the integrated dye concentration and d_f , the optical thickness of the fluid as shown below. This equation predicts that the amount of light passing through the dyed fluid will decay exponentially as integrated dye concentration increases.

$$ch_f = a \ln\left(\frac{I_0}{I}\right) = ad_f \quad (3-2)$$

$$d_f = \ln\left(\frac{I_0}{I}\right) \quad (3-3)$$

where I_0 light intensity leaving un-dyed fluid
 I light intensity leaving dyed fluid
 d_f optical thickness of fluid

12. Appendix D

12.1. Concentration Profiles Across Vent

Three Percent Experiments

